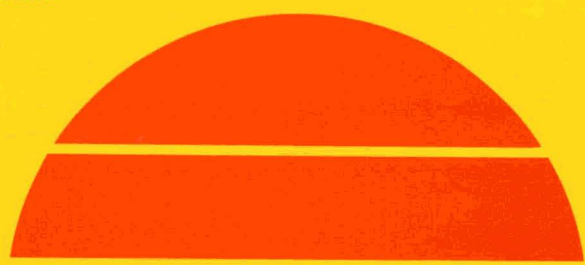282
5-25-78

LARGE AREA SILICON SHEET BY EFG

Fourth Quarterly Report, October 1—December 31, 1977

January 15, 1978

Work Performed Under Contract No. NAS-7-100-954355

Mobil Tyco Solar Energy Corporation
Waltham, Massachusetts

U.S. Department of Energy

Solar Energy

DISCLAIMER

This report was prepared as an account of work sponsored by an agency of the United States Government. Neither the United States Government nor any agency Thereof, nor any of their employees, makes any warranty, express or implied, or assumes any legal liability or responsibility for the accuracy, completeness, or usefulness of any information, apparatus, product, or process disclosed, or represents that its use would not infringe privately owned rights. Reference herein to any specific commercial product, process, or service by trade name, trademark, manufacturer, or otherwise does not necessarily constitute or imply its endorsement, recommendation, or favoring by the United States Government or any agency thereof. The views and opinions of authors expressed herein do not necessarily state or reflect those of the United States Government or any agency thereof.

DISCLAIMER

Portions of this document may be illegible in electronic image products. Images are produced from the best available original document.

Mobil Tyco Solar Energy Corporation
16 Hickory Drive
Waltham, Massachusetts 02154

LARGE AREA SILICON SHEET BY EFG

Program Manager: F.V. Wald

Fourth Quarterly Report - Subcontract No. 954355

Covering Period: October 1, 1977 - December 31, 1977

January 15, 1978

THIS PAGE

WAS INTENTIONALLY

LEFT BLANK

ABSTRACT

This report presents a detailed economic evaluation of several EFG
ribbon growth technology scenarios using the "SAMICS" interim price
estimation guidelines. It is concluded that the growth of 10 ribbons
from a double five ribbon furnace of the general type represented by the
existing Machine 3A, which is now being operated under this contract,
would meet the requirements of producing ribbon at a price below $20/m^2$,
the 1986 JPL goal. The technology requirements are that one operator can
operate 2 of the 5 ribbon growth stations in which each ribbon grows at a
speed of 7.5 cm/min and is also 7.5 cm wide. The machines also would
have to achieve a duty cycle of 67% at minimum and yields above 75%.
Finally, silicon must be available at $10 to ~$25/kg, depending on the
yield assumed, or achievement of the stated goal becomes quite difficult.
These conclusions are the final results of the economic analysis task
under the contract.

The technical sections then address themselves to the various ele-
ments which are clearly needed to meet the economic goals. Section I
discusses the progress towards the growth of 7.5 cm wide ribbon at 7.5 cm/
min. The major problem at present is to identify and resolve a severe
tendency in the ribbon to buckle as soon as it becomes more than 2 - 5 cm
wide and is grown at speeds over 4 cm/min. Several design changes in the
growth cartridge are being investigated to cure this problem. Section II
discusses the progress towards 5 ribbon (5 cm wide) multiple growth in
Machine 3A, and we are quite confident that the design changes which are
now being incorporated will lead to the desired demonstration of concur-
rent growth of 5 ribbons in short order.

Also, fluid flow phenomena have been investigated and it is shown
that by utilization of such phenomena the impurity distribution in the
ribbon may be manipulated to a significant extent. In fact, proper
utilization of these phenomena has allowed preparation of solar cells of

slightly over 10% efficiency from the center 2.5 cm of a 5 cm wide ribbon
of material grown under quite "dirty" conditions from Machine 3A. These
investigations are being further pursued.

Also, using (together with other methods) a somewhat novel "EBIC"
technique we were able to demonstrate that the internal grain structure
found. previously in some ribbons grown at high speeds has virtually no
influence on the performance of the material when made into a solar cell.

Table of Contents

List of Figures

List of Tables

I. INTRODUCTION

The present program is part of a total Mobil Tyco Solar Energy Corporation objective to produce silicon ribbon for solar cells at a cost which will allow their wide scale use for generation of electric power. On February 14, 1977, it was significantly expanded with the addition of several new tasks. In order to carry out these tasks, major pieces of equipment which have been designed and built under in-house funded programs were made available for use under the contract, namely a multiple EFG ribbon growth station and automatic growth control devices.

The edge-defined, film-fed growth process itself was initially developed for the commercial production of continuous, shaped single crystals of sapphire from the melt and was applied to growth of silicon for solar cells partly under NSF Grant GI37067X via Harvard University, JPL Contract 953365, and under NSF Grant GI433873. The basic feasibility of the application of EFG to the growth of silicon ribbon has been proven and the theoretical base for extending the technique to the efficient production of single crystal silicon sheet has been established. There are three fundamental objectives which are now being pursued:

1. Demonstrate that, from an improved resistance heated EFG crystal growth station (JPL No. 1), it is possible to obtain growth of single, continuous ribbons, 7.5 cm wide at a rate of 7.5 cm per minute. These ribbons furthermore are to be of a quality sufficient for fabrication of solar cells between 8% and 12% AM1 efficiency.

2. Demonstrate, by using the resistance heated multiple growth station made available to the program by Mobil Tyco (Machine 16, now JPL No. 3A), that it is possible to grow simultaneously 5 ribbons of 5 cm width at 7.5 cm per minute, using automatic control systems which have been developed also by Mobil Tyco and which are likewise made available to the program to be mated with the growth station.

3. Characterize the material grown not only in terms of its electrical and crystallographic properties, but more particularly as a solar cell. The aim here is to identify any fundamental barrier which might prevent the material from achieving 12% AM1 solar conversion efficiency when grown from the crystal growth stations employed here.

In summary, the program is now entering into a greater engineering research and development effort. Thus, the crystal growth machines now being used can be considered forerunners of true production machines because of their capability for wide (5 cm - 7.5 cm) high speed (7.5 cm/ min) multiple (5 ribbons) growth under automatic control. Also, with respect to the capability of the material to produce solar cells, the question is no longer whether EFG material is fundamentally capable of yielding solar cells of more than 10% AM1 efficiency, but, rather whether crystal growth machines operating at the high speeds required for economic reasons and with the complexity necessary for multiple growth can be designed such that they produce material from which large (e.g., 7.5 cm x 7.5 cm) cells of good efficiency can be fabricated at high yields.

II. WORK ON CRYSTAL GROWTH STATION JPL NO. 1 by T. Surek and J.P. Kalejs

A. Overview

Experimental work has centered on development of the 7.5 cm cartridge system in a continuing effort to obtain reliable growth of 7.5 cm wide ribbon at 7.5 cm/min growth rate. Several shortcomings in design were recognized, and design changes were made and tested. Considerable improvements in growth conditions and run-to-run reproducibility were realized. Nearly 25 meters of ribbon were grown in eight of the runs; some of the ribbon was 7 cm wide and was grown at speeds up to 6 cm/min. The 7.5 cm belt puller has been routinely used in the experiments; in one run, continuous growth of ribbon over a 1 3/4 hour long period was achieved. Qualitative studies were made of seeding and spreading problems and of stress and guidance induced buckling of the ribbon as a function of the growth conditions. Experimental and theoretical works to study fluid flow effects on impurity redistribution in the ribbon have continued.

B. Crystal Growth

1. Experimental

The experimental program on JPL No. 1 during this quarter has centered on continuing to develop the 7.5 cm cartridge system. The growth runs consisted of three experimental series, each lasting approximately one monthly period. During the first series of runs, the main thrust of the experiments was to attempt to reproduce earlier successful runs (run Nos. 18-26 and 18-27, reported previously[1]) in which 7.5 cm wide ribbon was grown. These experiments revealed a number of shortcomings in the design of the 7.5 cm cartridge. The second series of experiments was spent on incorporating and testing some of the design changes. New diagnostic and run procedures have helped to pinpoint and eliminate problems which were felt to have contributed to the lack of reliability of the cartridge system. Considerable improvements in growth conditions have

3

been realized in the second series of runs. In the third series of experiments, which will be continued during the next quarter, the effect of growth conditions (thermal parameters, gas flows, etc.) on growth performance was examined. The evaluation of the latter rests in the qualitative assessment of growth stability (e.g., ease of spreading to full width or of maintaining constant ribbon width) and of ribbon quality (e.g., residual stress, or deviations from flatness as a result of stress or guidance-induced buckling).

A summary of the experiments carried out on JPL No. 1 during this quarter is given in Table I. In the following, we discuss the important findings in the three experimental series.

Run Nos. 18-33 to 18-39: Growth of full-width ribbon from the 7.5 cm cartridge was not repeated in the initial series of runs, primarily because of a failure to achieve a proper temperature profile along the die top. Shortcomings in cartridge components believed to be responsible for this failure were identified in these runs, and design modifications were undertaken to correct them. The components which have the greatest influence on the die top temperature are the die face heater, the end heaters and the die shields. Inadequacy and unreliability of the heaters necessitated a return to the configuration used in the 5 cm cartridge, where the end heaters are located above the face heater, rather than in the same plane. In addition, a redesign of the high-temperature power connections was needed to correct heater power fluctuations caused by loosely fitting heater elements. Improvements in the die top shields were arrived at by reducing the possibility of warping and by increasing the opening in the shields and hence preventing contact to the die surface.

Changes were also made in several other areas to improve cartridge performance and reliability of operation. The afterheater shields were lengthened and increased in number, in order to reduce the afterheater power requirements. Graphite crucibles were used instead of fused silica crucibles from run 18-37 onwards. This reduced SiO build-up on the cold shoes which often impaired viewing of the growth interface. New pre- and post-growth diagnostic procedures were developed in the course of these runs to focus attention on growth problems caused by cartridge component misalignments. Because of the close proximity of high and low temperature components near the die top, misalignments of the order of 0.01 to 0.02 cm are suspected to be sufficient to make growth marginal, if not impossible.

The influence of gas flow to the cartridge during seeding was also

Table I. JPL No. 1 Run and Ribbon Growth Data.

Run No.	Cooling Block†	Growth Speed (cm/min)	Ribbon Width (cm)	Total Length (m)	Comments
18-33	A	-	-	-	Puller malfunction; mechanical corrections made.
18-34	A	-	-	-	Left-right temperature variation; tested belt puller; heavy SiO build-up.
18-35(a)	A	-	-	-	Short circuit in cartridge; assembly error.
18-35(b)	B	-	-	-	Left-right temperature variation; end heaters not operating properly.
18-36	A	-	-	-	Uniform temperature profile along die top; heavy SiO build-up prevented growth.
18-37	B	-	-	-	Graphite crucible in this and subsequent runs; left-right temperature variation; water flooding terminated run.
18-38	A	-	-	-	Ar/He gas flow effects studied; large center-to-end temperature difference; short growth only with frequent fractures after seeding.
18-39	B	-	-	-	Same as 18-38.
18-40	C	<5	2 - 3	2	First run with design changes; cooling block 0.30 cm from die top; fracture problems at seeding; buckling at faster speeds.
18-41	C	<5	2 - 3	1	Repeat of previous setup; similar findings to 18-40.
18-42	C	<5	2 - 3	2	Cooling block lowered to 0.18 cm from die top; similar findings to 18-40 and 18-41.
18-43	C	3 - 5	2.5 - 4.5	6	Repeat of previous setup; effect of afterheater temperature on buckles and residual stress studied; difficult to spread at slow speed.
18-44	C	3 - 4	4.5 - 6	4	Repeat of previous setup; difficult to spread; no buckles at slow speed, even in wide ribbon.
18-45	C	4	3 - 7	0.5	Repeat of previous setup; full-width seeding with seed holder; no buckles; temperature profiles measured.
18-46	D	3 - 5.5	4.5 - 7	5	Cooling block 0.07 cm from die top; 1 3/4 hours of continuous growth without freeze; buckles except in last 0.6 m.
18-47	D	5 - 6	6 - 7	4	Repeat of previous setup; buckles except in last 0.2 m.
18-48	B	-	-	-	Faulty thermocouple in afterheater; seed melted in afterheater; no growth.
18-49	B	-	-	-	Cooling block too close to die top; no visibility.

† A - All-molybdenum cooling block, 0.37 cm thick, 0.24 cm opening.
  B - All-molybdenum cooling block, 0.37 cm thick, 0.32 cm opening.
  C - "Stretched" version of 5 cm cooling block, 0.40 cm thick, 0.15 cm opening.
  D - "Stretched" version of 5 cm cooling block, 0.25 cm thick, 0.15 cm opening.

investigated during this series of runs. Mostly predictable effects were observed when argon/helium gas flow conditions were changed. With argon flow alone, variations in the flow rate had no effect on the meniscus height during static seeding. Introduction of helium to the cartridge resulted in a very rapid decrease of meniscus height along the die top; the transient was less than one second. These experiments suggest that varying the argon/helium gas mixture can be used for rapid control of spreading/tapering, of freezing, and in attaining the 7.5 cm/min growth rate. In the latter case, it has been generally noted that one of the difficulties with fast growth is the transient seeding process where the maximum growth rate (in essence) is reached during the initial ~30 seconds. Varying the argon/helium gas mixture from the beginning would allow one to attain the higher speeds in stages.

Run Nos. 18-40 to 18-42: The second series of runs was carried out to test the design changes detailed above. Growth conditions were improved and generally satisfactory and stable; about 5 meters of narrow ribbon were grown in the three experiments. These runs utilized a redesigned, "stretched" version of the 5 cm cartridge cooling blocks. These were designed to allow for flexibility in the mode of introducing gas to the interface region and in changing the cooling block operating temperature. The cold shoe and die heater arrangement closely approximated that used for growth with the 5 cm cartridge.

Although growth conditions were judged to be reasonable in these runs, difficulties were encountered in seeding and spreading of the ribbon in the width range of 2 to 4 cm. Shattering of the ribbon occurred frequently, generally within 30 to 60 seconds of the start of growth. For the most part, ribbon seeded successfully exhibited severe buckling when ramping to speeds over 4 cm/min. In addition, buckles were generated in ribbons over 2 cm wide when growth speeds were raised to 5 cm/min and above. These buckles were nearly periodic, with ridges separated by about 2 cm. Preliminary indications were that these growth problems were thermal in origin, perhaps accentuated by seed and cartridge component misalignments, or by partial obstruction of the growth slot by the afterheater radiation shields.

Run Nos. 18-43 to 18-49: The design changes which were implemented during the previous three runs to overcome problems with temperature variations along the die top received further testing during the third series of runs. Growth conditions were generally stable and reproducible from run-to-run; in the first five of the seven runs, nearly 20 meters of

6

ribbon were grown at widths up to 7 cm and speeds up to 6 cm/min. As in the previous runs, difficulties with growth generally consisted of seeding and spreading problems, and of the ribbon buckling during growth or occasionally shattering a short time after seeding. These problems were examined qualitatively in these runs as a function of the growth conditions such as the ribbon width, growth rate, gas flow to the cartridge and afterheater temperature.

The cooling block used in runs 18-43 to 18-47 was the "stretched" version of that used in the 5 cm cartridge system; the block thickness and distance from the die were changed in the last two runs, as noted in Table I. Runs 18-48 and 18-49 used the all-molybdenum cooling block which was originally designed for the 7.5 cm cartridge and was used in the earlier successful growth of 7.5 cm wide ribbon (runs 18-26 and 18-27[1]). These runs failed for reasons which were not related to the cooling block.

The maximum growth rate which could be attained was found to depend on the flow rate of helium to the cartridge. At a constant flow rate of ~0.1 ℓ/min of argon, the growth rate could be varied from ~2.5 cm/min to ~6.5 cm/min for helium flow rates of 0 to ~0.5 ℓ/min. A deleterious side effect of the increased helium flow was to cool the afterheater by increasing the conductive heat losses to the cooling block and at the cartridge face and side walls. To some extent, these heat losses could be offset by increasing the power to the afterheater.

Although stable growth, with a constant ribbon width, could be obtained at any growth rate in the range 3 to 6 cm/min (depending on the helium flow rate), it was not possible to spread a narrow ribbon to the full width of the die (7.5 cm) at growth rates < 4 cm/min. Typically, the regions of the die near the ends, where the ribbon was not growing, were frozen under these conditions; the range of the end heaters was not sufficient to overcome this problem. Spreading conditions could be obtained at faster growth rates (e.g., run 18-47), where the increased helium flow rates were accompanied by an increase in the power to the die face heater. As a result, the ends of the die became unfrozen, and spreading could be controlled by adjusting the power to the die end heaters. The spreading problem, and the related problem of ribbon edge stability, will require more quantitative observation and analysis during the next quarter.

Another aspect of the seeding/spreading problem which was worked on during these runs is the development of full-width seeding capability.

The typical seeds used in these runs were ribbons grown in the 5 cm cartridge system on JPL No. 3A, and hence were somewhat less than 5 cm wide. In the initial design of the seed holder, a 7 cm wide silicon wafer, cut from a 10 cm x 10 cm x 0.04 cm Wacker polycrystalline wafer, was held by a thin (0.125 cm) graphite plate which was pinned to a molybdenum plate to give a total "seed" length of ~35 cm (this length is required by the combined lengths of the cartridge and the belt puller). Full-width seeding was used in some of the ribbon grown in run 18-45; the experiments demonstrated that the previously experienced spreading problems at low speed growth (for a narrow seed) could be overcome by full-width seeding. Further tests of full-width seeding will require several obvious refinements to the design of the seed holder. Of course, once routine growth of 7.5 cm wide ribbon is established, the ribbons themselves can be used for subsequent seeding.

These experiments also permitted some observations of thermal stress related problems in wide and fast ribbon growth reported previously (e.g., Ref. 2). These problems include: (i) high residual stresses in the ribbon, which shows up either in problems of cutting the ribbon into solar cell blanks, or, on occasion, in the spontaneous shattering of the ribbon during growth; and (ii) generation of buckles in the ribbon during growth, which makes the ribbon unsuitable for cell blanks because of the large deviations from flatness. Peak-to-peak deviations are typically 0.1 to 0.15 cm; the buckles are usually periodic with a spacing of ~2 cm between ridges (see Fig. 1).

It was found that residual stress in the ribbon could be avoided by running the afterheater at a temperature $\geq 1100^{\circ}C$ (at the hottest point), while the stress was excessive for afterheater temperatures $\leq 900^{\circ}C$. The residual stress did not depend on whether or not the periodic buckles were generated in the ribbon. Problems with reaching a sufficiently high temperature in the afterheater occurred only when helium was used to attain the higher growth rates, as explained previously.

Thermal stress and/or misalignment problems are also believed to be responsible for the occasional shattering of the ribbon in the vicinity of the cooling block after some 30 seconds to one minute of growth. In order for the ribbon to fracture, its temperature must be below ~600°C in this region. Contact of a buckled or misaligned ribbon with the cooling block could have resulted in the rapid cooling of the ribbon and in the excessive thermal and/or mechanical stresses which caused fracture. The shattering of the ribbon was enhanced when the newly grown ribbon was
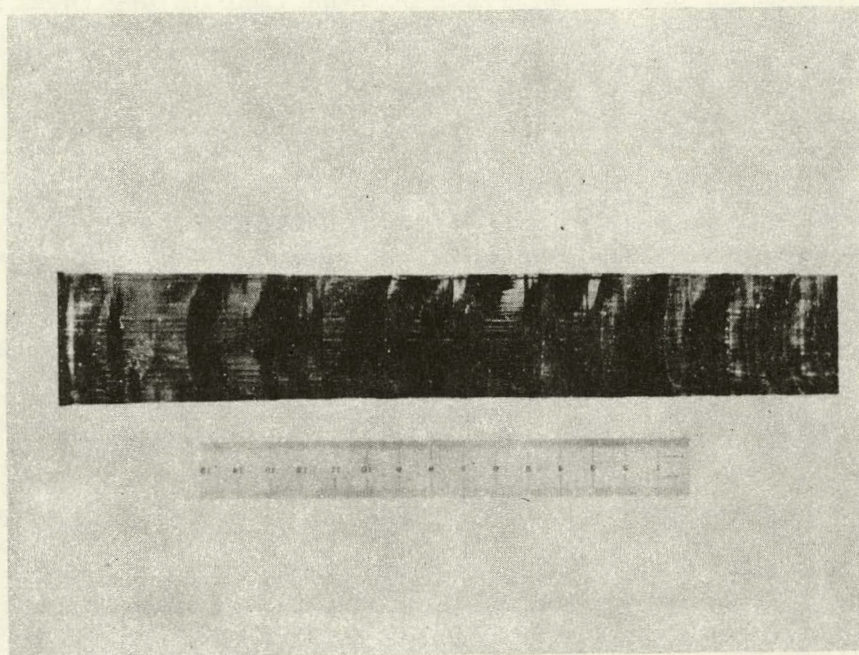
Fig. 1.   Periodic buckles in ribbon grown in run 18-47.

very thin, especially near the center; this is consistent with the expectation that a thin ribbon is cooled more rapidly than a thick ribbon. Growth with nonuniform thickness along the ribbon width invariably resulted in the buckling of the newly grown section just below the seed interface. This buckling was avoided when the initial ribbon was relatively uniform in thickness, which suggests that the initial buckling may be caused by thermal stresses which result from large temperature variations along the width of the ribbons with the nonuniform thickness.

The reasons for the nearly periodic buckles seen in Fig. 1 are not clear at this time. Under low speed growth conditions (nearly zero helium flow, < 4 cm/min growth rate), the ribbon was essentially flat aside from obvious guidance problems and/or the initial buckling during the seeding transient; the ribbon remained free of buckles for widths up to 7 cm. At faster growth rates, however, buckles were generated in all ribbons ≳ 2.5 cm wide. To this point in the investigations, no relationship has been found between the peak-to-peak amplitude or periodicity of the buckles and the ribbon width or growth rate.

There were two exceptions to the above observations which may shed some light as to the origin of the buckles. These occurred in runs 18-46 and 18-47 where, after a long period of buckled growth at > 5 cm/min and a ribbon width of ~7 cm, the buckles suddenly disappeared. The ribbon then remained essentially flat for ~60 cm in run 18-46 and ~20 cm in run 18-47; growth was terminated in both cases by a sudden freeze of the ribbon to the die. A possible explanation is that the buckles may be propagated by uneven cooling of opposite faces of the ribbon in the vicinity of the cooling block. The surface which is closer to the block loses more heat by conduction to the block; this causes a contraction of the ribbon such that the opposite surface will subsequently be closer to the block, and so on. Thus, a flat ribbon can be grown if the ribbon remains centered in the cooling block; this mechanism of periodic buckling requires an initial perturbation of a sufficiently large magnitude. Problems with guidance and misalignment, or buckling during the seeding transient can provide the necessary perturbation. In order to gain a better understanding of the buckling problem, we are currently developing a technique for profiling the ribbon surface to obtain quantitative measures of the buckle geometry.

A possible relationship between the periodic buckles and the vertical temperature profile in the ribbon was suggested in a previous report.[2] The explanation for buckles in the central portion of the ribbon was based

on the expectation (as a result of theoretical calculations) that the vertical temperature profile goes through a minimum in the vicinity of the cooling block and a maximum near the hottest point in the afterheater. The thermal stresses in the region of negative curvature of the temperature profile could then be relieved by the observed buckling of the ribbon.[2]

Attempts to obtain reliable measures of the vertical temperature profile have involved the development of suitable ribbon thermocouples, as discussed in detail in Section V. A preliminary test of graphite-silicon thermocouples was carried out in run 18-45. Figure 2 shows the temperature profiles measured under typical slow and fast growth conditions in terms of the helium flow to the cartridge. The afterheater temperature was about $1200^{\circ}C$ for both measurements. The profiles were obtained by slowly melting the ribbon into the die until the hot-junction of the thermocouple melted; the temperature values were deduced from the thermocouple reading at the melting point and the calibration curves shown in Section V. The results are in remarkable agreement with the expected form of the temperature profile; the ribbon is undercooled in the region of the cooling block before being reheated in the afterheater. It is also clear that, in fast growth where buckling is severe, there is considerably more undercooling of the ribbon than under slow growth conditions.

These preliminary measurements also indicated some difficulties with the technique which need to be resolved. Problems of shorting of the silicon or the graphite to the cartridge and of insufficient heat-sinking of the cold junction of the thermocouple in these early trials are discussed in Section V. Also, the curve for slow growth in Fig. 2 is obviously shifted by a constant amount ($\sim200^{\circ}C$) along the entire profile. This is the result of either the shorting of the thermocouple, or, more likely, the inaccurate observation of the melting point at the hot junction against which the other readings were calibrated. Such profile measurements, along with the geometrical profiling of the ribbon, will be used in the next quarter to address the problem of ribbon buckling.

Finally, aside from the various problems discussed above, two significant achievements in these experiments are noteworthy. First, the 7.5 cm belt puller has been incorporated into the system, and has been routinely used in the majority of the growth runs. (The stroke puller is used only to test specific guidance problems, thermal profiling, etc.) Ribbon was scribed in ~1 m sections as it emerged from the belt puller;
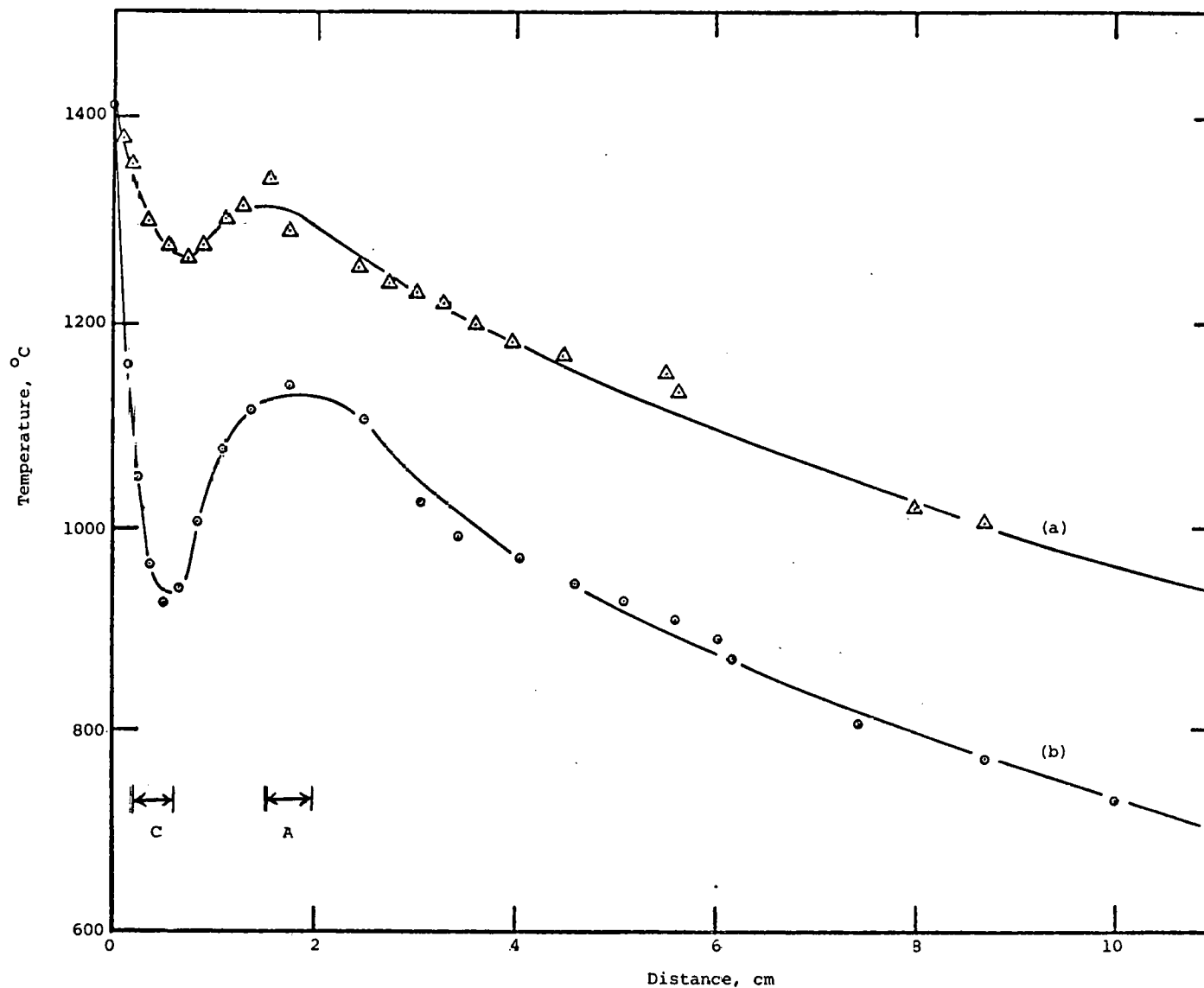
Fig. 2. Temperature distribution in ribbon as a function of distance from the growth interface.
(a) Slow growth conditions (0.15 ℓ/min Ar, zero Fe); (b) fast growth conditions (0.05
ℓ/min Ar, 0.4 ℓ/min He). The locations of the cooling block (C) and afterheater element
(A) are indicated in the figure.

unless the residual stress in the ribbon was high, there was no disruption to growth. A second (and related) important result is that continuous growth (i.e., growth without a freeze) was achieved in run 18-46 for a period of 1 3/4 hours; much of the ribbon was 7 cm wide and grown at speeds > 5 cm/min. Shorter periods of continuous growth were attained in many of the other runs. These results are an indication of the general improvements in growth conditions which have been realized as a result of improved designs and assembly and run procedures.

2. Fluid Flow Studies

A second experiment, run 16-090, using a single capillary die to test the effects of fluid flow on impurity redistribution, has been carried out on Station JPL No. 3A. The growth conditions were essentially the same as those for the first experiment, run 16-087. To evaluate the performance of the die, material was grown from this die as well as from a standard multicapillary die from the same melt with all growth conditions maintained as nearly identical as possible.

Ribbons 16-090-1 to 16-090-3 were grown from the multicapillary die, ribbons 16-090-4 to 16-090-8 from the single capillary die. Growth speeds were in the range 2.5 to 3.2 cm/min. The material grown in this run, as in 16-087, was characterized by a heavy SiC particle density. In addition, asymmetry in growth conditions was reflected in the SiC particle density as well as in a nonuniform ribbon thickness.

Material grown in this run has been examined for improvements in material quality. The results are discussed in Section IV. Again, the presence of SiC and asymmetry in growth conditions has made interpretation of the results more difficult. However, it is clear than an improvement in solar cell quality can be obtained by use of a single capillary die in place of the multicapillary die.

Material grown from the single capillary die in runs 16-087 and 16-090 has been prepared for impurity analysis using emission spectroscopy. The primary purpose of this analysis will be to compare the impurity concentrations at the sides of the ribbon to those in the center in order to look for the redistribution expected from fluid flow. Narrow strips along the growth direction were scribed from the sides and center of a 10 cm long ribbon, and these will be analyzed individually. A second sample was preferentially etched to remove about 0.008 cm of surface material at locations determined by black wax coating of specific parts of the front and back surfaces of the ribbon. The purpose here is to look for asymmetry of the impurity distribution across the ribbon thickness, which

could then be related to asymmetry in growth conditions. Some results are reported in Section IV.

Further experimental work with special die configurations to look for impurity redistribution effects has been postponed for the time being. Aluminum doped silicon of known resistivity has been obtained for future experiments. This will be used to dope the melt, and the material grown will be examined for redistribution of the aluminum. Die blanks have been ordered for the 7.5 cm cartridge to use in these and other experiments. They will be finished to desired fluid flow configurations for experiments in JPL No. 1 when acceptable growth conditions have been established in the 7.5 cm cartridge.

The results of theoretical work on impurity redistribution by fluid flow in 7.5 cm wide silicon ribbon growth are presented in detail in Appendix 7 in a paper which has been submitted for publication.

III. <u>MULTIPLE RIBBON FURNACE</u> by B.H. Mackintosh

A. <u>Overview</u>

During the fourth quarter, the multiple ribbon furnace was prepared for operation with five growth cartridges growing 5 cm ribbons from a continuously replenished melt under the control of one operator. One five-ribbon run was unsuccessfully attempted. Multiple ribbon growth had previously been demonstrated with three 2.5 cm ribbons in mid 1976 and three 5 cm ribbons in June 1977. The latter experiment was not very satisfactory though, as the four attempted runs were plagued by crucible failures, unreliable cartridge electrical performance, and silicon monoxide deposits on the capillary surfaces of the dies. Three ribbons were simultaneously grown for less than one hour, and they were not all full width. Work in the fourth quarter has been aimed directly at eliminating these hindrances. The melt replenishment, or continuous silicon feeding system was built and made operational. Most growth in the past quarter has been performed with graphite crucibles. To overcome the problem that graphite of sufficiently low porosity to contain silicon has not been available in stock of sufficient length to make crucibles for this furnace, a technique for transferring silicon from one small crucible to another through capillary bridges was evaluated. Numerous detail changes were made to improve the reliability and achieve similarity of operation among the five growth stations.

A design of die which imparts stability to ribbon edge position was evaluated. The effort to design such a die was motivated by a judgment that the electro-optical automatic width control (AWC) system on which testing and development work has been done during the year has not yet reached a degree of reliability and convenience of use that would make it a net asset in a multiple growth situation. Based on the limited experience of 5 runs though, we believe that use of "bulbous end" dies will fulfill a major part of the function of the AWC system as it now stands.

15

Also in this case, setup operations or changes of control mode during growth are not required of the operator. Furthermore, adding to the complexity of a machine already heavily burdened with electronic devices and interconnections is avoided.

During five weeks of the quarter, too, some of the equipment associated with the fourth and fifth cartridge positions was built while the subsystems of the three cartridges already in use were dismantled for cleaning, alignment, calibration, etc. A new utilities connection for the cartridge power supplies/was installed. Furnace operation resumed on the 15th of December.

A new main furnace insulation package had also been installed, so one day of running was devoted to "burning in" the furnace, i.e., burning away points of contact between the heating element connecting posts and tight-fitting insulation. On the following two days, dry heat-ups were performed to check operation of the rebuilt trap doors, check cartridge alignment with the hot zone openings, and test new cartridge heaters, power supplies and temperature controllers. Toward the end of this testing activity, the cartridges were used to take two sets of temperature measurements indicating the longitudinal temperature profile of the furnace. For one set of measurements, the lowermost tips of the dies were observed with an optical pyrometer. To view the die tips through the normal viewing slits, the cartridges were raised so that their bottoms were flush with the bottoms of the openings in the insulation. The other measurements were simply readings of the die temperature control thermocouples taken simultaneously with the pyrometer measurements. These two sets of measurements appear in Fig. 3, along with an earlier temperature profile measurement. Because the furnace had not until this time been outfitted with trap doors or other apparatus on three of the six positions, the only type of profile measurement previously made was to observe the far side heating element through the viewing slits. A typical set of readings is given in Fig. 3; these were taken with a radiometer whose optical path was partially obscured by glass and apertures in radiation shields. The readings are low by about 300 degrees, but they seemed relatively close together in light of the fact that the crucible and silicon were expected to level longitudinal profiles. The temperatures of the ends indicated by the recent pyrometer measurements were surprisingly low, but they were also made without the leveling influence of a crucible in the furnace.

A "practice" 3-ribbon growth run was executed to turn up any equipment problems remaining after dry testing and to refresh the operators'
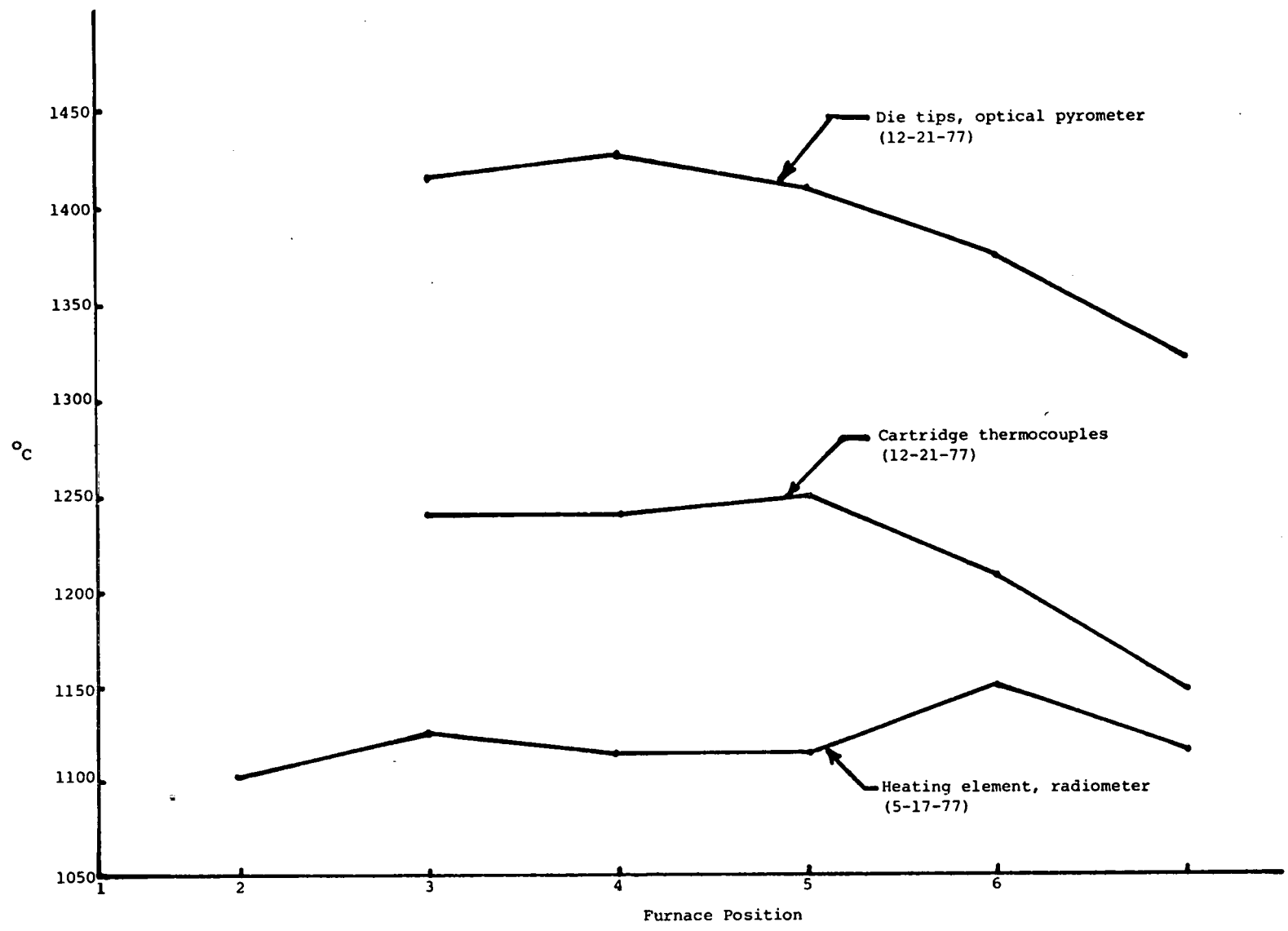
Fig. 3.   Furnace 3A temperature profiles.

growing techniques. As it was anticipated that miscellaneous small problems would crop up, a quartz crucible and conventional dies were used. The capillary bridge-connected graphite crucibles and bulbous dies, both in short supply, were saved for a second run much more likely to be free from bugs. Several small problems were indeed encountered in this run: one set of trap doors failed to open fully, in one cartridge too much time was required to "tune" the temperature controllers, and the silicon failed to rise up to the die in the right-most cartridge of the three. The crucible was not sufficiently hot at this position to maintain the silicon molten when the cartridge was lowered from midway to full insertion. However, the main zone temperature was not raised further because silicon monoxide was building up in and around the two cartridges which were operational. Two ribbons were grown simultaneously for one-half hour before ending the run.

Prior to the next run, the main furnace heating elements were modified to get the ends hotter by drilling large holes through them just inboard of the connecting posts located at the ends. Elements of larger cross section were substituted for the two side elements. The increased cross section more than compensated for the drilled holes, giving a lower element resistance and more heating power at the power supply's maximum voltage.

A three-section graphite crucible interconnected with capillary bridges, suitable for five cartridge operation, was installed (see Fig. 4). Silicon would be fed into the left hand section by the melt feeder and would flow to the other two sections. The run was begun by melting in sufficient material to fill the first crucible to its 10 mm optimum depth. This depth was indicated by the melt level probe; it was expected that the probe would soon lose contact as half of the melt transferred to the second crucible. When, after an hour and a half, the die in the second cartridge had not yet filled, it was removed from the furnace to visually observe the second crucible section. No silicon was present. An insulating plug was inserted in place of the cartridge to help heat the region of the capillary bridge and the bridge was probed with a thermocouple, which indicated a top surface temperature of 1530°. When after another hour no silicon had appeared, it was decided to melt ribbon into the second crucible through cartridge No. 1, grow ribbon from cartridge No. 3, and see if silicon would transfer to the third crucible section. A quantity of ribbon corresponding to the optimum filling depth was melted-in over the next half hour. Shortly thereafter, a silicon flood was perceived and the furnace shut off. Post-mortem

Melt Feeder   Growth Cartridges
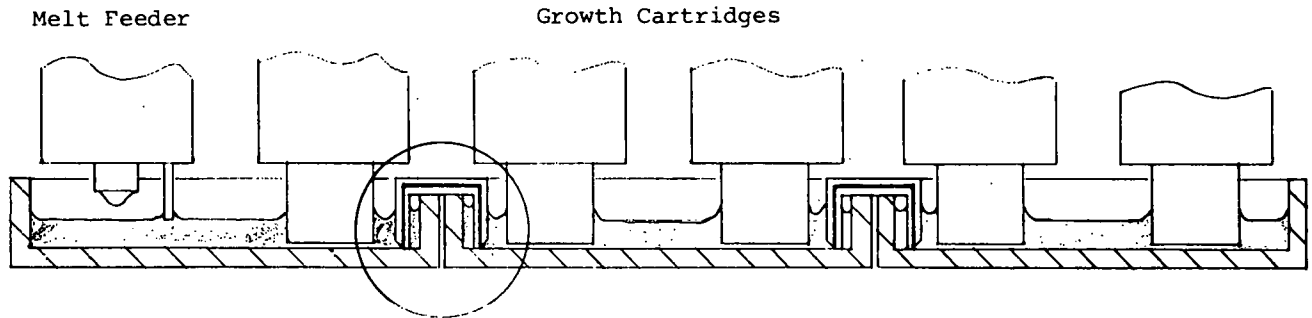
Fig. 4.   Three section capillary bridge connected crucible.
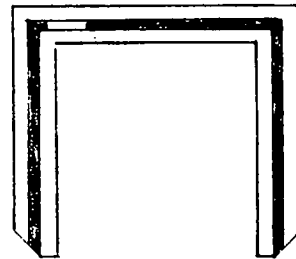
Fig. 5.   Appearance of capillary bridge, sectioned after run of 12/27/77
          circled above - dark areas indicate silicon presence (see text).

examination revealed that: (1) the silicon had fed up both sides of the capillary bridge to essentially the same points in all four channels as shown in Fig. 5; (2) silicon had filled the second crucible section only to about the lateral midpoint of the third die where apparently it was stopped by a freezing isotherm; (3) part of the support bar supporting the three crucible sections had broken, creating a path for heater current through the crucible support tongue in which the control thermocouple is located. This short circuit was minor with respect to the current through the heater, but it heated the crucible support and gave false high temperature readings. The crucibles supported each other and remained approximately in position despite the broken support; and (4) the flood was started by a piece of ribbon which fell sideways into the crucible; it proceeded quickly over most of the first two crucible sections because of the capillaries formed by the graphite crucible covers.

The reason for failure of the capillary bridge to work in this situation when it worked before is not understood. A freezing isotherm in the bridge is suggested by the fact that all four channels stopped flowing up from the first crucible at the same point, but silicon later flowed well past the centerline of the bridge from the other side. The thermal environment in which the bridge operates is very nearly symmetric about the bridge's centerline. A film of silicon dioxide has often inhibited wetting of die capillaries, but none was found in the bridge capillaries, nor should there have been any in this hot, well-shielded location. On the other hand, if silicon were to wet graphite according to simple surface tension theory and flow through small capillaries were impeded only by fluid viscosity, the EFG dies would fill in a matter of seconds. The fact that silicon rises up the dies at typically ~10 cm per hour indicates, however, that the silicon-carbon-SiC interaction at advancing wetting is a more complicated phenomenon.

The two obstacles to multiple growth at the end of this quarter are seen to be lack of satisfactory crucibles and problems with furnace temperature distribution. The crucible problem has two near-term solutions, both of which will be pursued immediately. One is the use of tubes below liquid level to join graphite sections. This technique was not tried earlier because the capillary bridge seemed to work well and presented less of a risk of floods. The other solution has just presented itself in the form of a new supplier of graphite, whose product, in 24 inch maximum length pieces, has recently been analyzed by the internal materials evaluation lab at Mobil Tyco. The graphite has properties almost identical to Poco DFP-1, including satisfactory resistance to liquid silicon.

It was found not to be available from stock in large sizes but was ordered and promised for delivery at the end of January. From the available 24 inch length, crucibles could be made extending under four cartridge positions plus the melt feeder. The manufacturer indicates that it is not practical to make it in greater lengths.

The problem of furnace temperature distribution will be at least partially solved in the near future by further trimming of the heating elements and addition and removal of insulation from various regions of the hot zone. It is now obvious that the design of the furnace utilizing three heating elements supported at the ends concentrates three major heat sinks at each end for which it is hard to compensate. When the hot zone is redesigned in the coming year to substitute cleaner construction materials, a different configuration of heater and supports will be chosen.

A full-length dummy "crucible" with deep wells for thermocouples has been made so that the results of all future efforts at producing a uniform temperature along the length of the furnace can be measured in an identical and meaningful way.

B. <u>Automatic Controls</u> by D.A. Yates

1. <u>Experiments</u>

During this quarter, bench testing of the scanning meniscus system was performed; the purpose was to check the gain through the system, assess the sources of noise, and obtain some operating experience with the system under controlled conditions. Thus, the system was mounted on the furnace in the normal configuration, but instead of using a normal die in the cartridge, a knife edge slab with a calibrated notch in the center was used as the object to be viewed. The notch was 125 mils wide and 20 mils deep. Using an optical magnification of about -1.4 and an electrical gain of .04 V per CCD element, a vertical gain of .11 V/mil was expected. The measured gain was .10 V/mil, i.e., 20 mil deep notch produced a 2.0 V signal on the storage oscilloscope. The horizontal gain was 1.5 V/inch. With the particular oscilloscope settings that were used (1.0 V/cm, vertical; .5 V/cm, horizontal), the "picture" of the "die top" with the notch was magnified about 40 times in the vertical direction and 1.2 times in the horizontal direction. Of particular interest was the noise on the vertical scan measurements. In this regard, some difficulties with the electrical grounding in the system were discovered and corrected; however, the limiting source of noise is currently due to

mechanical vibration. The peak-to-peak noise of .1 V corresponds to 2 mils. The vibration is due to the operation of the lower zone of the furnace, and the current design of the optical mounts tends to amplify the vibration. Decoupling the mount is expected to reduce the noise; however, the vibration also affects the die position itself so the problem cannot easily be corrected entirely.

A potential problem with optical aperture definition may exist and could cause malfunction of the scanning meniscus system. The light collected from the interface at various positions along the width must be equal. If not, the comparator triggering will misinterpret the true interface position. Since the light has to pass through several narrow horizontal slots in the insulation and shields, a small rotation of one slot with respect to another in the optical path may result in some flux blockage. The potential problem is not severe for the edge monitoring system (AWC) since one point is observed for each edge system and the comparators are independent. Also, the aperture stop in the lens is the limiting stop in the system. A sufficiently large lens aperture stop is needed so that the horizontal slit in the shield nearest the lens is the limiting stop. This aperture definition is a potential problem that needs to be investigated; if it does exist, several relatively simple solutions are available.

A chart recorder interface for the meniscus scanner was designed and constructed. A strip chart recorder is used and the operation of the chart recorder motor is synchronized with the sweep of the scanner mirror. The meniscus height data is routed to the signal input of the recorder. The recording can be performed periodically with an internal timer or under manual operation. A marker indicates the "beginning of sweep" on the chart paper. The system is currently set up to perform a scan in either 15 or 30 seconds and the width of the "picture" of the growing ribbon can be magnified to 2X.

During the last run of October (16-100), preparation for use of the Automatic Width Controller was made. However, severe noise spikes traced to the SCR unit of the lower zone were picked up by the electronics and caused the AWC to malfunction. This source of noise is a recent phenomenon since the problem did not exist during testing earlier in the year. It was subsequently discovered that significant electrical noise is found on the furnace chamber (in spite of the fact that grounding straps are used). The AWC mount has been connected to the chamber and the interface disappeared when the mount was disconnected. Therefore, we

have changed some of the mounting parts so that the mount is electrically insulated from the chamber; we anticipate that this will correct the interface problem. This noise also had been picked up by the servo loop of the galvanometer scanner; electrical isolation of the scanner mount similarly solved the problem.

The electronics have been assembled for the remaining two AWC systems, thus completing the circuitry for the five AWC units for the multiple growth system.

2. Future of the Automatic Controls Effort

During this past year, hardware which may very likely be useful for future automatic control of ribbon growth has been developed. This hardware has been based on an optical sensing of the meniscus height and edge position. The qualitative relationship of meniscus height and edge positions to temperature distribution in the die (and pulling speed) is an accepted concept as has been discussed in previous reports. For short term control (periods up to an hour), ribbon growth under automatic width control alone has, on occasion, been exceptionally stable, yet freezes have terminated the growth. The addition of meniscus height sensing for the control of the face heater might well solve this problem. Whether this combination of techniques is optimum or even adequate for the sensing and control of the growth process is an open question; it is still untested.

In any case, an increase in inherent process stability will undoubtedly contribute to the success of any automatic controls effort in the future. In particular, the question of "freezes" has to be addressed and they have to be eliminated by measures which increase the stability of growth. Alternatively, the phenomena preceeding and succeeding them have to be demonstrated to see how an automatic control system could be built to act either to avoid freezes altogether or to self-start growth after a freeze has taken place. Unless this is resolved, further development of automatic control equipment appears unwarranted and the automatic controls effort is, therefore, not being carried further at least for the next year.

23

THIS PAGE

WAS INTENTIONALLY

LEFT BLANK

IV. <u>MATERIALS CHARACTERIZATION</u> by C.V. Hari Rao, C.T. Ho and L.C. Garone

A. <u>Cross-Sectional EBIC</u>

As part of the characterization efforts aimed at examining the effects of cross-sectional grain structure, a new EBIC technique was developed which permits examination of the electrical activity of polished cross-sectional areas of solar cells (Fig. 6).

The EBIC contrast observed in the cross section appears to be the result of charge storage by the electron beam in the oxide layer remaining from the Syton 2% peroxide polishing solution.

An MOS device was prepared by polishing a ribbon surface in a Syton 2% peroxide solution and then allowing it to sit in a solution of peroxide for one hour. Small aluminum barriers were evaporated on this sample. The C-V characteristics of the device indicated that the surface is in the depletion mode at zero voltage. Thus, electron beam generated minority carrier electrons tend to drift toward the Si/SiO_2 interface as shown in Fig. 7. If the surface recombination velocity is slow at the interface, the minority carrier electrons will temporarily be stored there causing an n-type surface layer and thus making the EBIC observation possible.[3]

It was found that the EBIC contrast occurs with sustained beam irradiation. In addition, the contrast fades following a lapse of irradiation and can be regenerated. Figure 8 is an example of the typical type of contrast observed in solar cells prepared from material grown under this contract. Note that the surface EBIC can be observed to some extent along with the cross-sectional EBIC permitting an easy comparison of the activity and distribution of the defects through the bulk. In some cases, boundary defects which appeared uniformly active in the surface EBIC exhibited nonuniform activity in their cross-sectional EBIC. This could be related to the dislocation distribution along the boundary. Also, many of the active defects observed in the cross section were located only in
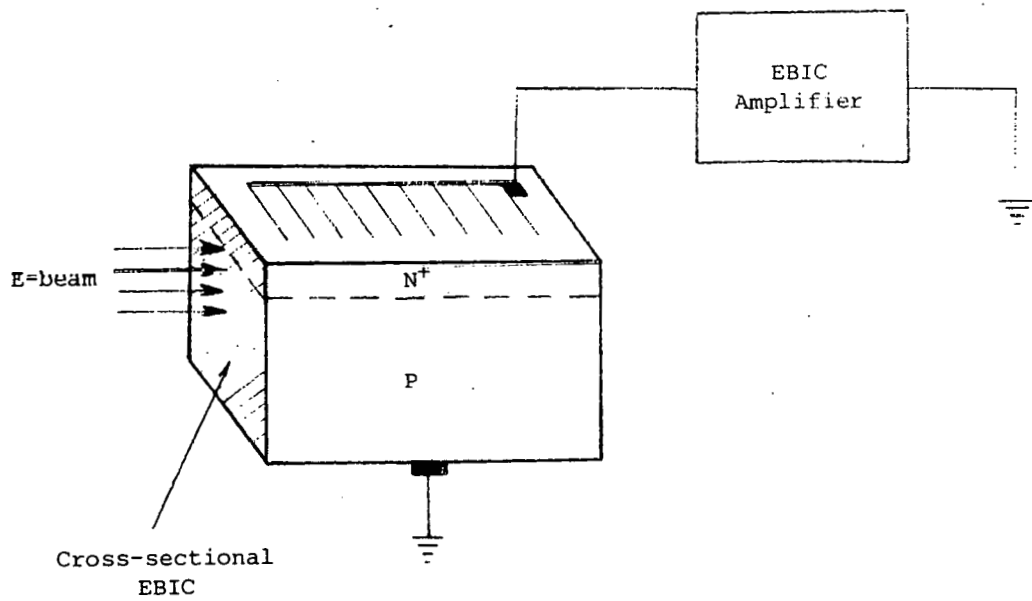
Fig. 6. Schematic of cross-sectional EBIC measurement.

(a)

(b)
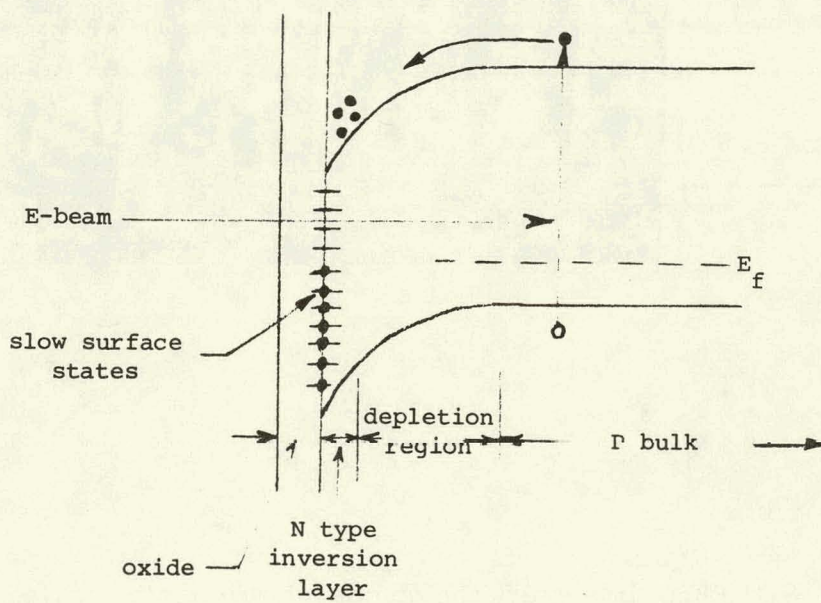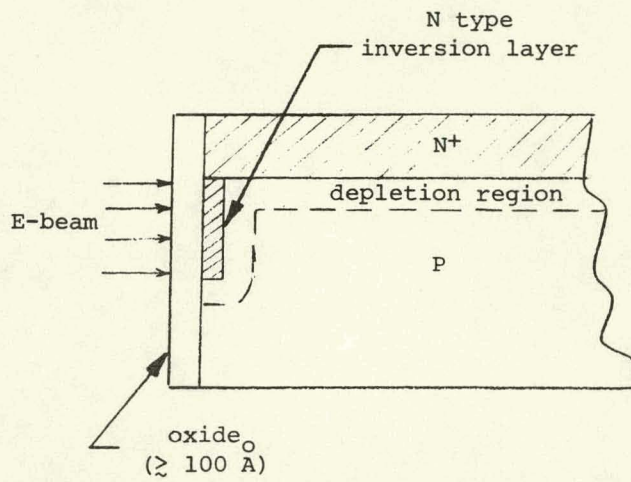
Fig. 7. Carrier generation and flow during cross-sectional EBIC. (a) is a schematic of the sample surface on electron beam irradiation, and (b) shows the carrier flow to the Si-SiO$_2$ interface.

Cross-sectional—→
EBIC

Surface—→
EBIC

.2 mm
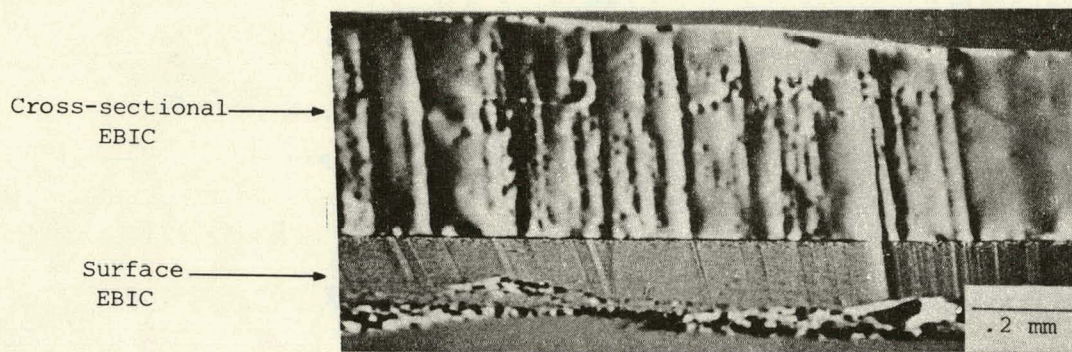
Fig. 8.   EBIC image of the cross section of a typical cell
          fabricated on JPL ribbons. Note that part of the
          surface EBIC image can also be observed.

the central position. Some of those that extended across most of the
thickness did not intersect the junction surface.

The activity in the cross section as a function of different process-
ing and growth conditions will be studied with this technique. In addi-
tion, by plotting the current output as a function of the electron beam
position, the diffusion length of the N^+ and P region can be determined.[4]
The cross-sectional EBIC technique can be used to reveal active defects
in the region where diffusion length measurements are taken. This permits
diffusion length data to be obtained as a function of position from an
active defect.

B. Cell Characterization

During this quarterly period, the question of the effect of central
grain structure on cell performance was addressed. The results indicate
that the central grain structure is innocuous in the absence of a high
impurity level. It will not in itself degrade the cell output. Data for
one of the samples studied in detail follows.

Twelve mesa diodes have been formed along the metallized fingers
from a 1.5 cm x 2 cm portion of cell No. 16807. This cell was fabricated
from run 16-087 in which a single capillary die was used and the photo-
voltaic junction was diffused on the type "a" surface.[1] The overall
conversion efficiency of the cell was 6.75% (no AR). Characterization of
the junction was performed using capacitance-voltage techniques. Capaci-
tance-voltage characteristics were measured on each diode. The net
ionized impurity concentrations ($N_A - N_D$) at a depth X from the space
charge region are calculated according to the standard Schottky equation:

$$N_A - N_D - \frac{-C^3}{q\varepsilon A^2}\left(\frac{dC}{dV}\right)^{-1}$$

$$X = \frac{\varepsilon A}{C}$$

where A is the diode area and ε is the dielectric constant of silicon.
Figure 9 summarizes the measurement results. Diodes No. 4 and No. 10
have large SiC particles in them and show higher and nonuniform distribu-
tion of impurities. The remaining diodes have relative uniform net
acceptor concentration, $N_A - N_D \simeq 1.05 - 1.55 \times 10^{16}$ cm^{-3}, which are in
excellent agreement with conductivity and Hall measurement data. From
this measurement we conclude that the compensating donor impurity con-
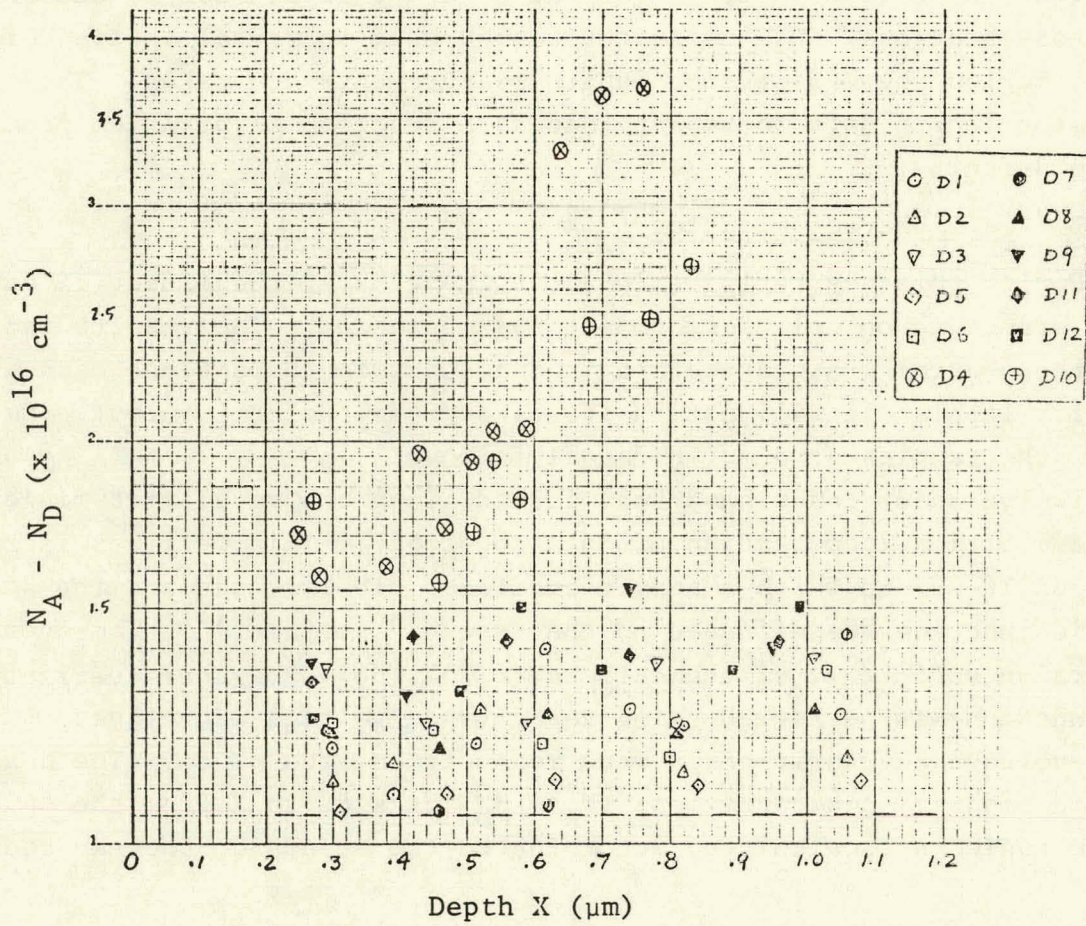
Fig. 9. Net carrier concentration as a function of depth Data was obtained as a result of capacitance-voltage measurements.

centration in this ribbon is less than 1×10^{15} cm^{-3} near the space charge region.

This sample was further characterized using spectral response techniques in the dark and at AM1, surface photovoltage (SPV), and diode recovery lifetime. The solar cell parameters were also measured. The electrical activity as well as the structural features of the individual defects in the mesas were examined with the EBIC technique followed by preferential surface and cross-sectional etching.

In Figure 10 we depict the location of each diode and the measurement results are tabulated in Table II. The optical micrographs of the cross sections of some of the mesas seen in Fig. 11 show the internal grain boundaries to have no correlation with the diffusion lengths or photovoltaic characteristics of the mesa diodes. However, the solar cell parameters measured appear to correlate well with the diffusion lengths obtained. In the cases of mesas No. 4 and No. 10 which contain SiC particles, the open-circuit voltage is quite low, presumably due to shunting effects of the particle.

Several other interesting observations were made. The variation of the diffusion length appears random and shows no definite pattern on the various positions of the sample. (It should be noted that this sample was cut from an undetermined region of a full-width section so that it is not possible to locate the central capillary's relative position to this sample.) In addition, the densities of the electrically active boundaries do not correlate with the diffusion length values or lifetimes obtained. It may be speculated that the overall impurity level is lower in this material (as evidenced by the average diffusion length of this material being higher than usual); therefore, the impurity level of the matrix plays a more important role than that segregating to the boundaries.

C. Recent Solar Cell Data

Material grown from run 16-090 has been processed into solar cells for evaluation. In this run, the material was grown from a single capillary die as well as from a standard multicapillary die. For the single capillary grown material, the overall features of the two types of surfaces (as we observed in run 087) have been reproduced. The overall cell outputs are lower than in material from the previous run. For the material from the multicapillary growth, however, the cell output is discernibly lower than the material prepared using a single capillary. The cell data are tabulated in Table III.

31
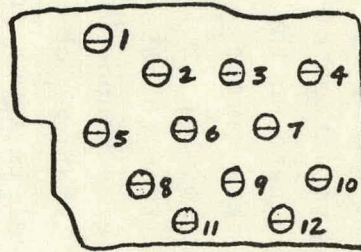
Fig. 10.   Schematic showing position of the mesa diodes in Table II.

Table II.   Electronic Properties and Cell Parameters of Mesas Fabricated on Solar Cell No. 16-807.

Diode No.	L_D (SR)	L_D (SPV)	τ_F (DRT)	L_D @ AM1 (μm)	J_{sc} (mA/cm^2)	V_{oc} (Volt)	FF	η (%)
1	39.9 ± .8	31.6 ± 1.7	3.31 ± .03	48.9	27	.562	.814	12.4
2	13.4 ± .5	6.6 ± 1.2	1.68 ± .03	–	21.8	.533	.797	9.26
3	29.1 ± 1.3	24.6 ± 1.6	3.67 ± .05	40	27.7	.558	.803	12.4
4*	11.9 ± 1.2	7.5 ± 1.2	1.48 ± .04	–	24	.191	.554	2.54
5	19.5 ± .3	19.1 ± 1.3	2.11 ± .07	–	21.1	.537	.795	9.0
6	8.20 ± .8	1.4 ± 1.0	1.52 ± .04	22.9	20.7	.533	.796	8.78
7	10.2 ± 1.0	5.6 ± 1.0	1.86 ± .07	21.1	20.7	.526	.787	8.57
8	24.7 ± .6	19.4 ± 1.7	2.60 ± .02	42.9	24.9	.550	.789	10.8
9	27.6 ± 1.2	24.3 ± 1.7	3.53 ± .05	39.8	25.8	.542	.794	11.1
10*	16.5 ± 1.2		1.65 ± .03	–	19.8	.153	.472	1.43
11	8.6 ± .6	3.5 ± .9	1.29 ± .04	22.9	23.3	.523	.763	9.30
12	11.8 ± 1.1	9.6 ± 1.2	2.94 ± .05	23.5	20.3	.532	.753	8.13

*SiC particle.

32

Mesa No. 5

Mesa No. 6

Mesa No. 7

500 μm
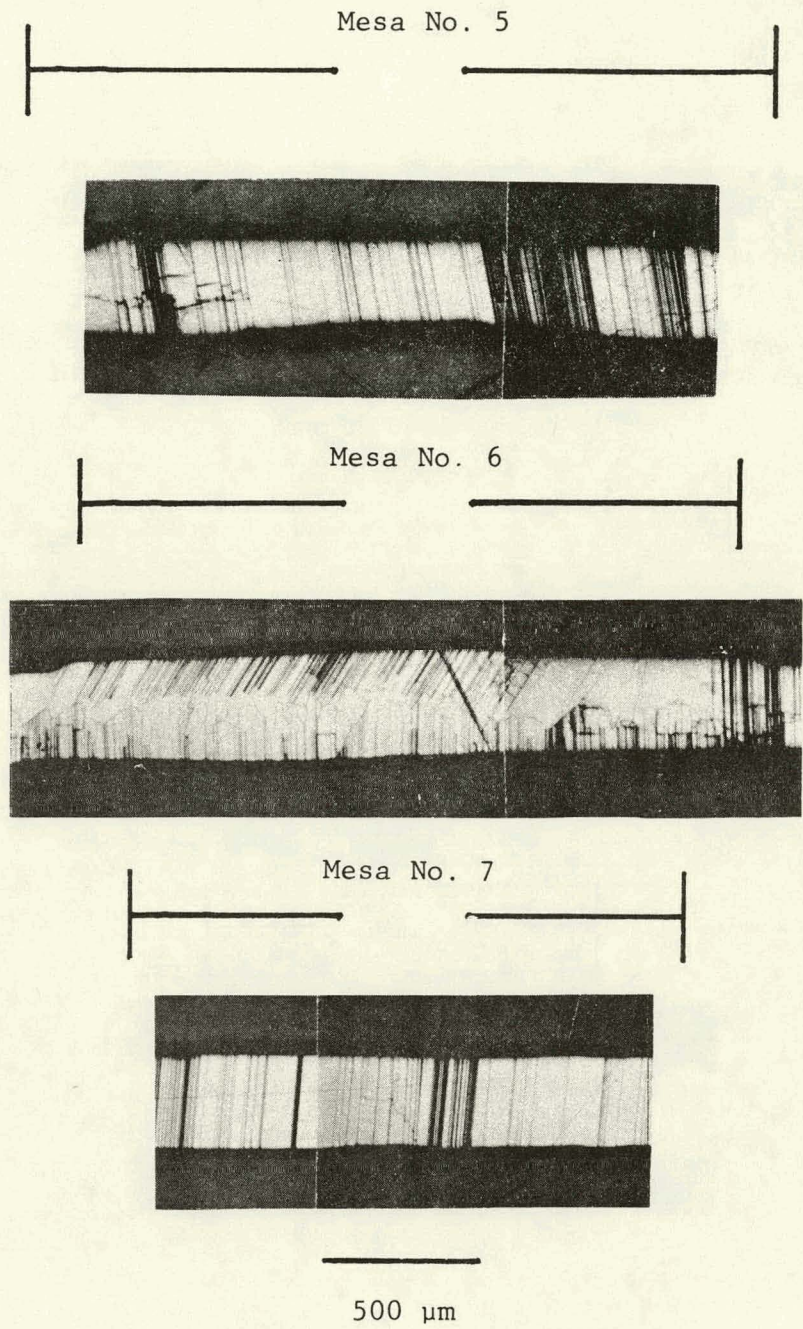
Fig. 11. Cross-sectional structure of mesas (numbered as shown)
fabricated on solar cell No. J16-807. Cross section
has been preferentially etched to reveal defect
structure.

33
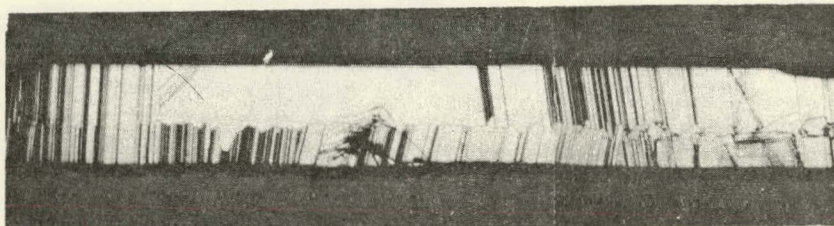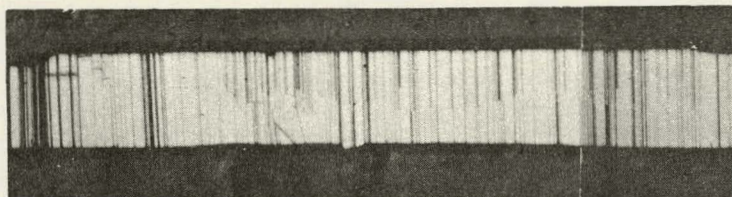
Mesa No. 8

Mesa No. 9

Mesa No. 10
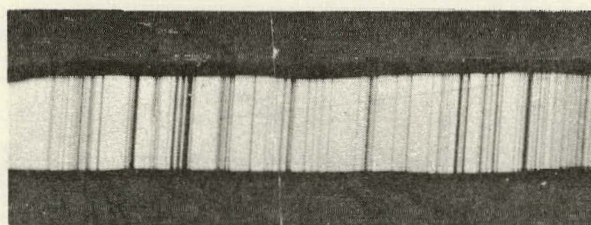
500 µm

Fig. 11. Continued.

Table III. Solar Cell Characteristics of Ribbon Material
Grown from Run No. 16-090.
AM1. No AR. Cell Area >15 cm^2.

Cell No.	J_{sc} (mA/cm^2)	V_{oc} (Volt)	F.F.	η (%)	Comments
16901	15.61	0.467	0.477	3.48	Multicapillary die
16903	13.70	0.342	0.438	2.05	
16911	16.61	.511	.677	5.74	
16912	17.06	.514	.70	6.15	
16914	17.07	.513	.623	5.45	
16915	16.68	.514	.708	6.06	Single capillary die
16916	16.63	.460	.431	3.30	
16917	17.53	.507	.603	5.36	
16918	16.59	.498	.589	4.86	

Finally, in Table IV we tabulate the AM1 characteristics for three high output cells all fabricated from the ribbon samples grown as part of the fluid flow experiment (cut from the center 2.5 cm of a 5 cm wide ribbon). These cells have evaporated AR coatings and represent the "state-of-art" performance for the resistance furnace grown materials.

D. Chemical Analysis

In making solar cells from the ribbon material grown using the "F" type single capillary die in System 16, run 16-090, the observation was made that cells fabricated on the surface having heavy SiC density resulted in very poor cell performance, whereas cells fabricated on the "front" or lower SiC density surface resulted in cells which displayed quite respectable solar cell characteristics. Therefore, one set of samples was chosen for chemical analysis. They were selectively etched to a 3 mil removal to determine whether the surface heavy in SiC particles also was heavier in other impurities. This was found not to be the case.

It was found that there was a variation in impurity concentration across the width of this sample. The sample scribed as shown in Fig. 12 had 3 mils removed from the top surface (lower density of SiC particles) of sections A and D, and 3 mils removed from the back surface (higher density of SiC particles) of sections B and C. Sections A and C exhibited a total impurity concentration of 2 ppm while sections B and D had a higher impurity concentration of 40 and 13 ppm, respectively. Section B's major contaminants were Ca, Al, Fe, Mg, and Ti impurities, whereas section D had mostly Ca, Fe, Mg, and Ti. The Fe and Ti contaminants can be attributed to the stainless steel components in the hot areas of the furnace, i.e., inner furnace enclosure. The Ca, Al, and Mg impurities are likely from the quartz crucible or from particulates off the exit port plate.

Recent spreading resistance data on F-type material from run 16-090 reveal a very uniform resistivity in the material, regardless of the nature of the surface (with or without SiC particles), of approximately .9 to .7 Ω-cm across the width of the sample, a substantial improvement over previous materials. The variation seen in the diffusion lengths in another sample from the same run adjacent to the one analyzed is shown in Fig. 13. Although we do not know if the sample sides correspond with one another, we can assume this to be likely. Future analysis will include the impurity concentration across the width of the sample with attention being paid to the channel vs. the edge regions.

36

Table IV. AM1 Cell Characteristics of Three High Output
Cells Fabricated on Ribbon Samples Grown as
Part of "Fluid Flow Experiment".

Cell No.	Area (cm^2)	J_{sc} (mA/cm^2)	V_{oc} (Volt)	FF	η (%)
1603	10.2	25.45	.535	.712	9.69
16808	15.3	27.66	.554	.693	10.62
16915	20.4	24.35	.525	.688	8.81

←————— Full width of sample —————→

A 3 mils etched off front	B 3 mils etched off back
C 3 mils etched off back	D 3 mils etched off front

⎧‾‾‾‾‾‾‾‾‾‾‾⎫ ⎧‾‾‾‾‾‾‾‾‾‾‾‾⎫

2 ppm   13 - 40 ppm
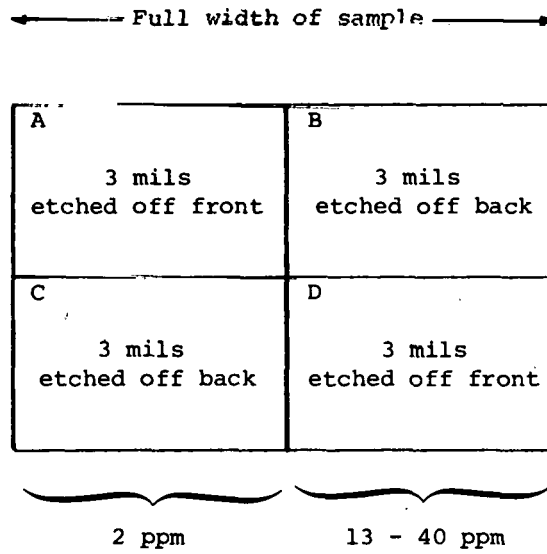
Fig. 12. Sampling procedure used for chemical
analysis of ribbon 16-090.
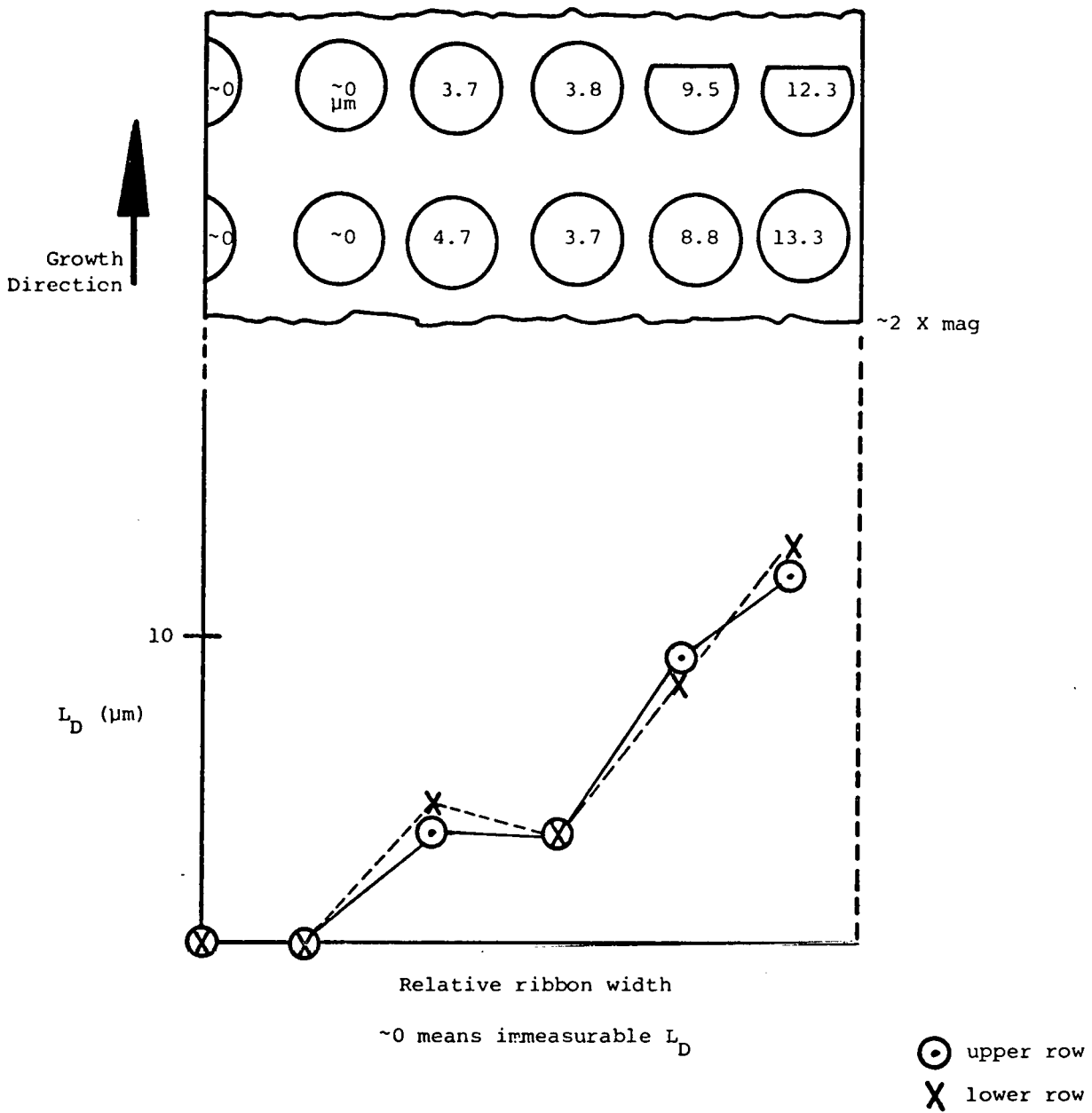
Fig. 13. Variation of SPV diffusion length with position along ribbon width for sample No. 16-090-4K. Ribbon was grown as part of "fluid flow experiment".

THIS PAGE

WAS INTENTIONALLY

LEFT BLANK

V.   CONCEPTUAL DESIGN STUDIES by E. Sachs

A.   Overview

The Annual Report[1] included a concise description of the meta-
morphosis of the conceptual design task. As the conceptual design task
per se ends this quarter a more detailed review is presented.

The task began with the responsibility of examining innovative
alternatives for EFG machines of future generations. The fundamental
choices to evaluate were single ribbon versus multiple ribbon machines,
and cartridge versus non-cartridge technologies. Variations in the pack-
ing configurations of multiple ribbon machines became an obvious point of
consideration including a 2-ribbon cartridge which, if it could be made
to work, would instantly double the output of any machine.

During this time, difficulties were being encountered in the
multiple growth attempts on Machine 16. These problems can be divided
into two groups, gross reliability problems with the furnace, and those
related to the viability of crystal growth when the equipment performed
without identifiable mishap. The problems relating to the furnace in-
clude trap door failures, large temperature gradients in the "main zone",
thermal expansion tolerancing problems causing heater shorts, etc. While
any one of these problems is sufficient to lead to the failure of a run,
they must be kept in perspective. The present furnace is essentially
unchanged since it was designed three years ago; it is truly a first
generation item of a new technology. The solutions to these problems
certainly require ingenious design and detailed attention to materials
selection, but are, on the whole, straightforward as the problems are well
understood.

That is not, however, the case with problems specific to the
growth system. Ribbon spreading, tapering, freezing and buckling are
incompletely understood. The die temperature control is primitive. More
complicated die configurations are largely unexplored. All this was

41

obvious from the repeated observation that during runs, even when no machine related problems were encountered, multiple growth was still difficult. Even single ribbon growth during a large percentage of runs was not easily possible and most often required full operator attention. Such problems as the ribbon cracking and buckling on JPL No. 1 are recurring reminders of the complex nature of thermal and mechanical interactions within a high speed growth cartridge.

At this point the results from the economic analysis task indicate that our present multiple ribbon cartridge technology, were it developed to production worthy status, holds the promise of undercutting the DOE price goals for sheet silicon.

As such, it is apparent that there is no need to go to a more complex packing geometry which would only invite destabilizing interactions between ribbons, or a different furnace layout which might or might not be more advantageous in some respects but which would set us back to the beginning of the task of building a system. Efforts directed at gaining a better understanding of our current (broadly speaking) growth systems and refining them appear now more fruitful.

This is the impetus for the shift of the conceptual design task from the design of the "machine" of the future to the understanding and design of the critical portion of the growth system of the future, namely the components directly related to the thermal, crystallographic, chemical, and fluid flow phenomena of the growing ribbon. Such a microscopic version of the "conceptual design" task can now proceed with the assurance that the resultant technology will meet economic goals.

It is this line of reasoning, coupled with the promise of great potential rewards for growth system innovation (as illustrated by the recent retrial of the bulbous end die; see Section III) that has led to the decision to build (at MTSEC expense) and run an additional growth station (No. 17) as a fully instrumented machine, designed as a research tool and test bed. It is this effort which will take the place of the conceptual design task during the coming year.

B.   Experimental Efforts

1.   Silicon-Carbon Ribbon Thermocouples

These in-situ ribbon termocouples are made by depositing SiO_2 on a ribbon, etching through in small spots, and gluing a strand of graphite string to these spots with graphite cement. The junction of carbon and silicon where the SiO_2 has been removed becomes the thermocouple bead. The graphite string is secured to the ribbon using alumina

42

paste which also electrically insulates the string from growth system components during use (see Section II). Electrical contact is made to the ribbon at the top using indium solder, while silver paste is used to contact the graphite bead.

One difficulty is that the room temperature thermoelectric sensitivity of silicon is over one order of magnitude higher than the high temperature sensitivity. This makes it imperative to accurately control the cold junction temperature. Accordingly, a seed holder was designed so that the metallic elements on both sides of the ribbon are water cooled. The ribbon is then thermally coupled to the seed holder by high thermal conductivity epoxy. The water temperature is measured after leaving the seed holder.

The calibration setup used to test these thermocouples consists of an "isothermal" grahpite block with an acceptance slit for the thermocouple ribbon and a hole for a reference W-Re thermocouple, supported within a graphite enclosure. A cylindrical resistance heater surrounds this "black" enclosure and insulation fully surrounds the entire system.

Calibration runs were done with four thermocouple ribbons. Ribbon No. 1 was run with the seed holder water cooled on one side only, whereas ribbons 2, 3, and 4 were run with the seed holder water cooled on both sides. All four calibrations were run against the same W-Re thermocouple. The results are plotted in Fig. 14. The data from ribbons 2 and 4 are within 1 mV of each other point for point from 6.50 mV on the W-Re thermocouple upwards. The data points for No. 4 from 6.5 mV up are omitted for clarity. These curves have all been corrected to a cold junction temperature of $10^{\circ}C$ using the measured seed junction water temperature and the previously determined room temperature thermoelectric sensitivity of silicon (1.26 mV/$^{\circ}C$).

The general shapes of the curves are consistent with data from Neuberger.[5] Of principal interest is the observation that all four curves have very much the same shapes from the point where the slope becomes negative. They appear only to be shifted by an additive constant which is independent of temperature. Above approximately $300^{\circ}C$ the thermoelectric properties of silicon are dominated by intrinsic processes and hence are a very weak function of dopant level. Below this temperature, in the extrinsic range, dopant level and crystal structure do affect thermoelectric properties. Hence, one would expect that the high temperature junctions of different ribbons would have the same behavior, but that the low temperature junctions would have different ab-

43
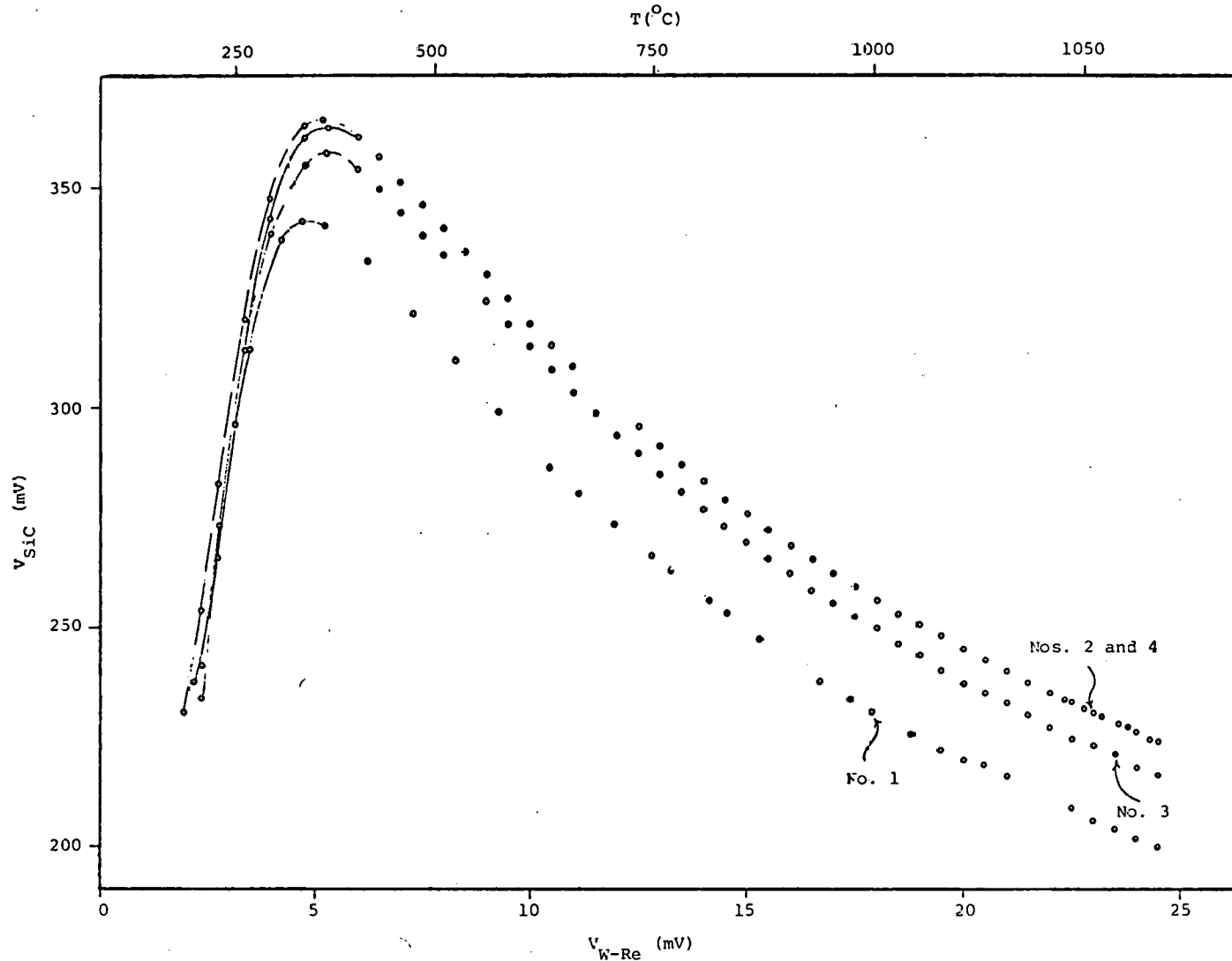
Fig. 14. Calibration data for Si-C thermocouple output vs. W-Re (3% Re vs. 25% Re) output. Data for curve No. 4 is plotted only below 6.5 mV as the remaining points are within 1 mV of the corresponding points for ribbon No. 2. The cold junction is corrected to $10^C C$.

solute Seebeck coefficients, and would, therefore, contribute differently to the measure voltage. This seems to be at least one explanation for the constant additive difference between ribbons.

Utility

These silicon-carbon thermocouples may be used without extensive individual calibration by obtaining a single calibration point and appropriately shifting the readings. Thus, a single calibration curve may be drawn up for all Si-C thermocouples, applicable to temperatures from 400°C to the melting point of silicon. This curve can be shifted by an arbitrary constant in Si-C thermocouple output, as it is only the curve shape that matters. Such a curve is presented in Fig. 15 taken from ribbon No. 2 data in Fig. 14. The data has been extrapolated to the melting point (25.8 mV W-Re), adjusted so that the melting point gives 0 mV on the Si-C thermocouple, and plotted against temperature.

The melting point sensitivity of these thermocouples is .080 mV/$^\circ$C, approximately 4.5 times that of a W-Re thermocouple. Errors in absolute temperature measurement arise from two sources: cold junction temperature indeterminance, and any errors inherent to the described curve shifting process. Cold junction temperature indeterminancy is multiplied by the ratio of the high and low temperature sensitivities (approximately 16). The curve shifting process would seem, from the data presented, to be accurate to within about 2 mV from 500° on up.

Since the cold junction temperature will most certainly be known to within .5°C, the total error is:

$$\text{Error} = .5^\circ\text{C (16)} + 2 \text{ mV} \frac{1}{.08} \, ^\circ\text{C/mV} \; ;$$
$$\text{Error} \cong 33^\circ\text{C} .$$

Relative measurements of temperature will be more accurate as the above error reflects a maximum error over the range 500 - 1412°C.

2. Capillary Filled Siphon

One growth run trial of the capillary filled siphon is described in detail in Section III.
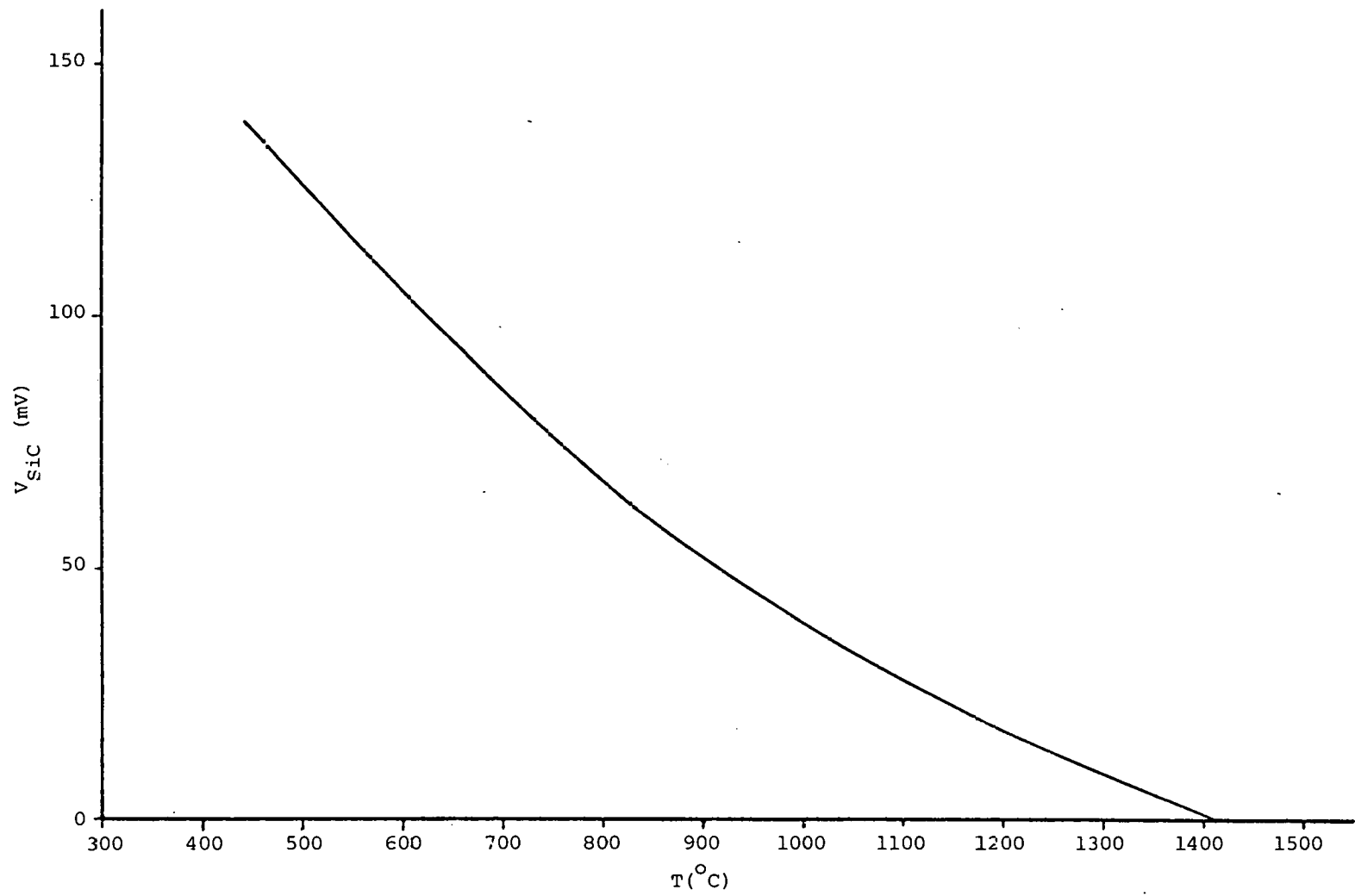
Fig. 15.   Calibration curve for Si-C thermocouple taken
from data for ribbon No. 2, Fig. 14.

VI. <u>ECONOMIC ANALYSIS</u> by S.R. Nagy

A. <u>Introduction</u>

Activity over the past quarter centered around the SAMICS interim
price estimation guidelines. As noted in the Annual Report,[1] the chief
weakness of the cost analysis model had been its inability to articulate
overhead. This problem was largely eliminated by adopting the SAMICS
linear price estimating model, which replaces the scheme of straight line
depreciation on lifetime equipment and 100% overhead on direct labor.
The SAMICS format also facilitates sensitivity analysis within the price
domain and comparison with other sheet growth technologies.

The resulting economic analysis model accepts an input data set
which contains all the growth parameters, costs, space and labor require-
ments, parts lifetimes and utility consumption rates involved in EFG
ribbon growth. This input data set is then prepared for insertion into
the SAMICS interim standard price estimating equation:[6]

$$\text{Price} = \frac{0.49*EQPT + 97*SQFT + 2.1*DLAB + 1.3*MATS + 1.3*UTIL}{QUAN}$$

Briefly, the equation burdens the categories of equipment, floor space,
direct labor, materials and utilities, then divides this annual manufac-
turing cost by the appropriate annual quantity produced to achieve the
market price of the product, which in this analysis is ribbon silicon
blanks.

B. <u>Structural Revisions of the Economic Analysis Model</u>

In addition to the incorporation of SAMICS, there are several sig-
nificant differences between the present economic analysis model and the
version described in the Annual Report.[1] The model was revised with
the intent of more accurately reflecting the present status of multiple
ribbon growth in any technology projection. Furthermore, early model

47

results indicated that certain simplifications could be made without significantly affecting the analysis.

Cartridge gas and electricity costs are no longer dependent on duty rate. It had been assumed that the duty rate fraction at any part of the run indicated the average number of cartridges operating over any given hour. This, in itself, is a useful way of understanding the duty cycle. If a cartridge was not in operation, it was assumed that no power or gas was being used. Present experience is not sufficient to determine how often this would be the case. Consequently, the duty rate now appears only in the defining equation for the output; it no longer serves to decrease operating costs. Appearing only in the time-averaged denominator of the price calculating equation, it no longer needs to be time-dependent. The average value of the old time-dependent duty rate was 68.6%. The new time-independent value of 67% (see Table V) agrees within the noise level of the model, simplifies it, and still represents a specific duty cycle projection, described below.

The defining cost equations for equipment have been restructured. Melt replenishment subsystems, such as controls and power supply, had not been adequately accounted for. These subsystems now form a separate term in the model. The electro-optical controls cost has been removed from the cartridge lifetime subsystems cost and augmented to include sophistication beyond the existing automatic width control system. The scriber cost has been added into the cartridge lifetime subsystems cost, since it is not large enough to require autonomy in the model output.

The costs for cartridge and melt replenishment subsystems have been divided into two categories: lifetime equipment and materials cost per run. The earlier version of the model attempted to articulate various parts lifetimes. At the present stage of development, lifetimes cannot be determined with precision. Dividing all the parts costs by their maximum lifetimes yields a minimum materials cost per run while all the minimum parts lifetimes provides a maximum cost per run. Finally, the older version of the model demonstrated that water costs are insignificant. They have been dropped from the model.

All of these changes have been made to provide assurance that economic technology projections are indeed safe estimates in their reflections of the present status of multiple ribbon growth. The economic analysis model is as detailed and complete as practical with the present level of EFG multiple ribbon growth experience.

48

Table V. Input Data to Economic Analysis Model: End of 1978.

	END OF 1978
Ribbon width (in.)	2.0
Growth rate (in./min)	2.0
Run length (hours)	116
Number of runs per year	52
Number of ribbons per furnace	5
Number of furnaces per production unit	1
Number of operators per production unit*	1
Yield (mass ribbon wafers/mass poly)	0.65
Duty rate	0.67
Polysilicon ($/kg)	70.0
Dopant ($ dopant/$ poly)	0.1
Thickness (in.)	0.008
Furnace lifetime subsystems ($/furnace)	30000
Cartridge lifetime subsystems ($/ribbon)	9000
Melt replenishment subsystems ($/furnace)	9000
Electro-optical controls ($/ribbon)	3000
Area for one production (sq ft)	100
Labor pay rate ($/hr)	5.00
Furnace insulation ($/furnace)	2000
Insulation lifetime (runs)	52.0
Heating elements ($/furnace)	500
Heating elements lifetime (runs)	26.0
Crucible ($/furnace)	400
Crucible lifetime (runs)	5.0
Melt replenishment materials ($/furnace/run)	40.00
Die ($/ribbon)	15.00
Die lifetime (runs)	1.0
Cartridge materials ($/ribbon/run)	40.00
Argon ($/100 cu ft)	2.35
Helium ($/100 cu ft)	8.48
Electricity ($/kwh)	0.05
Furnace argon flow rate (ft^3/hr/furnace)*	10.0
Cartridge argon flow rate (ft^3/hr/ribbon)*	5.0
Cartridge helium flow rate (ft^3/hr/ribbon)*	2.0
Furnace power consumption (kw/furnace)*	20.0
Cartridge power consumption (kw/ribbon)*	2.2

*Modes of time-dependent variables.

C. Technology Projections

Table V lists the default input data set. These figures describe the present multiple ribbon growth furnace, which accommodates a continuous melt replenishment system and five ribbons growing 5 cm wide at 5 cm/min.

No-growth furnace runs (with melt) of over three days have been attained with no indication of this being a limit. In-house operations have run for five days, indicating that growth station components such as shields, dies and crucibles may remain at temperature for at least this period. Consequently, the planned 116 hour run period stays within the limits dictated by previous achievements. As such, it is a conservative estimate. The run period is divided into four sections.

1. Unattended furnaces are automatically brought to temperature - 4 hours.

2. Growth start procedure; all ribbons are seeded, brought to full width and growth rate - 4 hours.

3. Routine crystal growth - 104 hours.

4. Furnaces are cooled down, routine maintenance is performed, and charged setups are inserted for the automatic start procedure commencing the next run - 4 hours.

By the end of 1978, the present furnace is assumed to be capable of running with one operator over the given run period with a duty cycle of at least 67%. The yield is anticipated to range between 50% and 80%. The mean of 65% is used here. The use of chunk polysilicon is planned, and a 0.2 mm ribbon is projected.

All of the cost and lifetime data was carefully re-examined over the last quarter. The furnace, cartridge, and melt replenishment lifetime subsystems are rounded up from the costs of the present equipment. As discussed above, the electro-optical controls cost is higher than the cost for the present automatic width control systems.

The area accounts for the floor space taken up by JPL 3A, room for auxiliary equipment, an operator aisle and free space alongside the furnace to facilitate hot zone removal.

The furnace insulation and heating element costs are actual values for JPL 3A. Their lifetimes are extrapolations of present data based on the given 116 hour run mode. The crucible cost is for a set of connected graphite crucibles. The five run lifetime assumes that the crucibles have been drained at the end of a run so that they can withstand thermal cycling. Using the actual costs of parts presently employed, and life-

times based on present performance extrapolated to the given run cycle, a range of $10 to $40 per run has been established for cartridge and melt replenishment materials. The maximum values are used here. Dies can be purchased in medium-sized lots for about $15 each.

For the furnace, argon flow and power consumption are higher than their modes during start-up, and go to zero in the last four hours of the run. Cartridge rates are zero for the first and last four hours of the run. Otherwise, they retain the stated values, which are typical.

The input data set represents a conservative near-term projection. It is as accurate and complete as present growth experience allows. No new cost-reducing technology has been assumed. The primary technical assumptions are a modest five ribbons per operator with a low yield and duty rate.

The economic analysis model prepares the data for insertion into the SAMICS cost-to-price equation. Table VI depicts the breakdown of costs which becomes the input for the SAMICS equation, as shown at the bottom of the table. PRICE1 gives the SAMICS value-added portion of the market price, and PRICE2 adds in a burdened cost of poly and dopant, giving the SAMICS total blank market price. It is important to note here that poly-silicon is not burdened by any amount in the JPL calculation of wafer price goals, even though a sequence of autonomous companies is assumed. Unless it is explicitly stated otherwise, the prices examined in this analysis do burden poly and dopant by the SAMICS materials coefficient of 1.3. The end of 1978 projected total blank market price of about $160/m^2 falls under the current 1980 JPL wafer price goal, adjusted to 1977 dollars, by $120. The output of one furnace is about 10% of the 1978 JPL production quantity goal.*[1] Three such production units would consti-tute a single hypothetical company with over 30% of the wafer market. One might also note that if the proposed 1982 poly cost of $25/kg is assumed, this same projection yields a total wafer price of about $112/m^2, $34 below the 1982 inflation adjusted goal. The operation of the present multiple ribbon machines with a moderate duty rate, yield, and run period would meet the JPL 1982 price goals if indeed a commensurate materials

---

*A cautionary note should be sounded here, though. The major problem of the JPL No. 3A furnace at present lies in the fact that it does not yet produce material with predictable solar cell quality. Yield in the present context, therefore, only indicates the ratio of mass of ribbon divided by mass of poly and does not connote any solar cell specifica-tions.

Table VI.   End of 1978:   Cost Breakdown.

```
EQUIPMENT
     FURNACE LIFETIME SUBSYSTEMS         ($)          30000.00
     CARTRIDGE LIFETIME SUBSYSTEMS        "           45000.00
     CONTROL EQUIPMENT                    "           15000.00
     MELT REPLENISHMENT SUBSYSTEMS        "            9000.00
     TOTAL EQUIPMENT                      "           99000.00

FLOOR SPACE
     AREA FOR ONE PRODUCTION UNIT       (SQ FT)         100.00

DIRECT LABOR
     DIRECT LABOR PAY RATE              ($/RUN)         560.00
     TOTAL LABOR                        ($/YR)        29120.00

MATERIALS
     FURNACE INSULATION                 ($/RUN)          38.46
     HEATING ELEMENTS                     "              19.23
     CRUCIBLE                             "              80.00
     MELT REPLENISHMENT MATERIALS         "              40.00
     DIE                                  "              75.00
     CARTRIDGE MATERIALS                  "             200.00
     FURNACE ARGON                        "              26.79
     CARTRIDGE ARGON                      "              63.45
     CARTRIDGE HELIUM                     "              91.58
     TOTAL MATERIAL                     ($/YR)        32994.85

UTILITIES
     FURNACE POWER                      ($/RUN)         112.10
     CARTRIDGE AND MR POWER               "              71.28
     TOTAL UTILITIES                    ($/YR)         9535.76

QUANTITY
     OUTPUT FROM ONE RUN               (SQ M/RUN)        38.94
     TOTAL QUANTITY                    (SQ M/YR)       2024.65
```

PRICE1=(0.49(99000.)+97(100.)+2.1(29120.)+1.3(32995.)+1.3(9536.)/ 2025.
       = $ 86.26/SQ M

PRICE2=PRICE1+1.3(POLY COST)=PRICE1+1.3($56.09/SQ M)
       = $159.18/SQ M

quality is achieved which would allow production of 10 - 12% efficiency solar cells at that time.

The computer print-out in Table VII gives a breakdown of the contributions to price derived from the output of the SAMICS equation. PRICE1 and PRICE2 are summed and displayed at the bottom of the table for convenience. One readily sees that the high value of each total coupled with a low output per run indicates a low throughput per growth station. In conjunction with design engineers, a number of alternative multiple ribbon growth configurations have been modeled. A simple extension of the present configuration was decided upon. It has been determined that other design alternatives pose too high a success risk to justify their relatively minor economic return.

The model input data which describes this production unit is given in Table VIII. The changes from the end of 1978 projection are noted with arrows. The major change is the employment of the 7.5 cm cartridge now under development in a two-furnace production unit. The increase in yield and decrease in thickness represent progress achieved through routine operation of the present 7.5 cm cartridge and multiple ribbon furnace. The duty cycle maintains its low level. The die cost represents twice the materials cost for the present 7.5 cm die.

No technological breakthroughs are assumed by the data set. The costs, as present values, are essentially for the construction of one dual furnace unit, where each furnace is quite similar to JPL 3A. These data, then, represent a fairly conservative technology projection. The cost breakdown as it becomes input for the SAMICS equation is given in Table IX. Table X presents the breakdown of the SAMICS output, illustrating the total blank price and the contribution of each element to it.

The total blank price of $31.44/m^2 undercuts the inflation adjusted 1984 JPL goal of $43.5/m^2, and would do so even if the poly cost were doubled. Comparison with the 1984 goal does not imply a strict time period for the dual furnace production unit. The time frame is determined by the parallel development of the 7.5 cm cartridge and the present multiple ribbon furnace, and the difficulties which arise in assuming the reliable operation of each. This reliability factor is the most crucial, yet most difficult variable to ascertain.

SAMICS was designed to price a manufacturing process at a plant-sized level. The dual furnace production unit has been costed on the basis of constructing and operating a single unit. Table XI gives the model input data for a single production unit on the basis of constructing

Table VII. End of 1978: Price Breakdown.

EQUIPMENT

FURNACE LIFETIME SUBSYSTEMS	($/SQ M)	7.261
CARTRIDGE LIFETIME SUBSYSTEMS	"	10.891
CONTROL EQUIPMENT	"	3.630
MELT REPLENISHMENT SUBSYSTEMS	"	2.178
TOTAL EQUIPMENT	"	23.960

FLOOR SPACE

AREA FOR ONE PRODUCTION UNIT	"	4.791

DIRECT LABOR

DIRECT LABOR PAY RATE	"	30.204
TOTAL LABOR	"	30.204

MATERIALS

FURNACE INSULATION	"	1.284
HEATING ELEMENTS	"	0.642
CRUCIBLE	"	2.671
MELT REPLENISHMENT MATERIALS	"	1.336
DIE	"	2.504
CARTRIDGE MATERIALS	"	6.678
FURNACE ARGON	"	0.871
CARTRIDGE ARGON	"	2.142
CARTRIDGE HELIUM	"	3.058
TOTAL MATERIAL	"	21.186

UTILITIES

FURNACE POWER	"	3.743
CARTRIDGE AND MR POWER	"	2.300
TOTAL UTILITIES	"	6.123

QUANTITY

OUTPUT FROM ONE RUN	(SQ M/RUN)	38.936
TOTAL QUANTITY	(SQ M/YR)	2024.646

PRICE1=23.960 + 4.791 +30.204 +21.186 + 6.123
    = $ 86.26/SQ M

PRICE2=PRICE1+1.3(POLY COST)=PRICE1+1.3($56.09/SQ M)
    = $159.18/SQ M

Table VIII.   Input Data to Economic Analysis Model:
            Single Production Unit.

	END OF 1978	SINGLE PRODUCTION UNIT
Ribbon width (in.)	2.0	3.0 ←
Growth rate (in./min)	2.0	3.0 ←
Run length (hours)	116	116
Number of runs per year	52	52
Number of ribbons per furnace	5	5
Number of furnaces per production unit	1	2 ←
Number of operators per production unit*	1	1
Yield (mass ribbon wafers/mass poly)	0.65	0.80 ←
Duty rate	0.67	0.67
Polysilicon ($/kg)	70.0	10.0 ←
Dopant ($ dopant/$ poly)	0.1	0.1
Thickness (in.)	0.008	0.006 ←
Furnace lifetime subsystems ($/furnace)	30000	30000
Cartridge lifetime subsystems ($/ribbon)	9000	9000
Melt replenishment subsystems ($/furnace)	9000	9000
Electro-optical controls ($/ribbon)	3000	3000
Area for one production (sq ft)	100	165 ←
Labor pay rate ($/hr)	5.00	5.00
Furnace insulation ($/furnace)	2000	2000
Insulation lifetime (runs)	52.0	52.0
Heating elements ($/furnace)	500	500
Heating elements lifetime (runs)	26.0	26.0
Crucible ($/furnace)	400	400
Crucible lifetime (runs)	5.0	5.0
Melt replenishment materials ($/furnace/run)	40.00	40.00
Die ($/ribbon)	15.00	10.00 ←
Die lifetime (runs)	1.0	1.0
Cartridge materials ($/ribbon/run)	40.00	40.00
Argon ($/100 cu ft)	2.35	2.35
Helium ($/100 cu ft)	8.48	8.48
Electricity ($/kwh)	0.05	0.05
Furnace argon flow rate (ft^3/hr/furnace)*	10.0	10.0
Cartridge argon flow rate (ft^3/hr/ribbon)*	5.0	5.0
Cartridge helium flow rate (ft^3/hr/ribbon)*	2.0	2.0
Furnace power consumption (kw/furnace)*	20.0	20.0
Cartridge power consumption (kw/ribbon)*	2.2	2.2

*Modes of time-dependent variables.

55

Table IX. Single Production Unit: Cost Breakdown.

EQUIPMENT		
FURNACE LIFETIME SUBSYSTEMS	($)	60000.00
CARTRIDGE LIFETIME SUBSYSTEMS	"	90000.00
CONTROL EQUIPMENT	"	30000.00
MELT REPLENISHMENT SUBSYSTEMS	"	18000.00
TOTAL EQUIPMENT	"	198000.00
FLOOR SPACE		
AREA FOR ONE PRODUCTION UNIT	(SQ FT)	165.00
DIRECT LABOR		
DIRECT LABOR PAY RATE	($/RUN)	560.00
TOTAL LABOR	($/YR)	29120.00
MATERIALS		
FURNACE INSULATION	($/RUN)	76.92
HEATING ELEMENTS	"	38.46
CRUCIBLE	"	160.00
MELT REPLENISHMENT MATERIALS	"	80.00
DIE	"	100.00
CARTRIDGE MATERIALS	"	400.00
FURNACE ARGON	"	53.58
CARTRIDGE ARGON	"	126.90
CARTRIDGE HELIUM	"	183.17
TOTAL MATERIAL	($/YR)	63389.70
UTILITIES		
FURNACE POWER	($/RUN)	224.20
CARTRIDGE AND MR POWER	"	142.56
TOTAL UTILITIES	($/YR)	19071.52
QUANTITY		
OUTPUT FROM ONE RUN	(SQ M/RUN)	315.64
TOTAL QUANTITY	(SQ M/YR)	11213.43

PRICE1=(0.49(198000.)+97(165.)+2.1(29120.)+1.3(63390.)+1.3(19072.)/11213.
     = $ 25.09/SQ M

PRICE2=PRICE1+1.3(POLY COST)=PRICE1+1.3($ 4.88/SQ M)
     = $ 31.44/SQ M

Table X. Single Production Unit: Price Breakdown.

```
EQUIPMENT
     FURNACE LIFETIME SUBSYSTEMS        ($/SQ M)         2.622
     CARTRIDGE LIFETIME SUBSYSTEMS         "             3.933
     CONTROL EQUIPMENT                     "             1.311
     MELT REPLENISHMENT SUBSYSTEMS         "             0.787
     TOTAL EQUIPMENT                       "             8.652

FLOOR SPACE
     AREA FOR ONE PRODUCTION UNIT          "             1.427

DIRECT LABOR
     DIRECT LABOR PAY RATE                 "             5.453
     TOTAL LABOR                           "             5.453

MATERIALS
     FURNACE INSULATION                    "             0.464
     HEATING ELEMENTS                      "             0.232
     CRUCIBLE                              "             0.965
     MELT REPLENISHMENT MATERIALS          "             0.482
     DIE                                   "             0.603
     CARTRIDGE MATERIALS                   "             2.411
     FURNACE ARGON                         "             0.315
     CARTRIDGE ARGON                       "             0.774
     CARTRIDGE HELIUM                      "             1.104
     TOTAL MATERIAL                        "             7.349

UTILITIES
     FURNACE POWER                         "             1.352
     CARTRIDGE AND MR POWER                "             0.859
     TOTAL UTILITIES                       "             2.211

QUANTITY
     OUTPUT FROM ONE RUN              (SQ M/RUN)       215.643
     TOTAL QUANTITY                   (SQ M/YR)      11213.425
```

PRICE1= 8.652 + 1.427 + 5.453 + 7.349 + 2.211
      = $ 25.09/SQ M

PRICE2=PRICE1+1.3(POLY COST)=PRICE1+1.3($ 4.88/SQ M)
      = $ 31.44/SQ M

Table XI. Input Data to Economic Analysis Model:
1 of 100 Production Units.

	SINGLE PRODUCTION UNIT	1 OF 100 PRODUCTION UNITS
Ribbon width (in.)	3.0	3.0
Growth rate (in./min)	3.0	3.0
Run length (hours)	116	116
Number of runs per year	52	52
Number of ribbons per furnace	5	5
Number of furnaces per production unit	2	2
Number of operators per production unit*	1	1
Yield (mass ribbon wafers/mass poly)	0.80	0.80
Duty rate	0.67	0.67
Polysilicon ($/kg)	10.0	10.0
Dopant ($ dopant/$ poly)	0.1	0.05 ←
Thickness (in.)	0.006	0.006
Furnace lifetime subsystems ($/furnace)	30000	20000 ←
Cartridge lifetime subsystems ($/ribbon)	9000	4500 ←
Melt replenishment subsystems ($/furnace)	9000	4500 ←
Electro-optical controls ($/ribbon)	3000	1500 ←
Area for one production (sq ft)	165	165
Labor pay rate ($/hr)	5.00	5.00
Furnace insulation ($/furnace)	2000	1000 ←
Insulation lifetime (runs)	52.0	52.0
Heating elements ($/furnace)	500	250 ←
Heating elements lifetime (runs)	26.0	26.0
Crucible ($/furnace)	400	200 ←
Crucible lifetime (runs)	5.0	5.0
Melt replenishment materials ($/furnace/run)	40.00	20.00 ←
Die ($/ribbon)	10.00	2.00 ←
Die lifetime (runs)	1.0	1.0
Cartridge materials ($/ribbon/run)	40.00	10.00 ←
Argon ($/100 cu ft)	2.35	2.12 ←
Helium ($/100 cu ft)	8.48	6.36 ←
Electricity ($/kwh)	0.05	0.03 ←
Furnace argon flow rate (ft^3/hr/furnace)*	10.0	10.0
Cartridge argon flow rate (ft^3/hr/ribbon)*	5.0	5.0
Cartridge helium flow rate (ft^3/hr/ribbon)*	2.0	2.0
Furnace power consumption (kw/furnace)*	20.0	20.0
Cartridge power consumption (kw/ribbon)*	2.2	2.2

*Modes of time-dependent variables.

and operating 100 such units. At an annual unit output of over 1.1×10^4 m^2, this represents a total factory output of 1.1×10^6 m^2/year, or about 25% of the JPL estimated 1986 silicon wafer market. In all but two cases, the cost reductions are no more than 50%. They have been determined in conjunction with project engineers and are based in part on quotations received from various vendors for large purchase orders. Cartridge materials have been reduced to $10 (which is still within the possible range of values for the end of 1978) due to the large volume of parts in 1000 growth stations. Die costs have been reduced to $2.00 because of a volume of 52000 dies per year.

The cost reduction is due totally to scale-up. No technical optimization is involved. Table XII presents the cost breakdown and SAMICS calculation for one of the 100 production units, and Table XIII gives the price breakdown from the SAMICS output. A comparison of Table XII with Table IX reveals the cost reductions attained in scaling up. The 1986 JPL total wafer price goal, in 1977 dollars, is $20.8/m^2$. However, as mentioned earlier, the contribution of poly to this price is not burdened in the JPL calculations. If the burdening on poly is removed, the multiple ribbon technology projection records a blank market price of $21.2/m^2$, about four-tenths of a dollar higher than the goal.

It is anticipated that over the next eight years, multiple ribbon growth will be optimized so that the low duty cycle used here as well as the stated yield will increase significantly. Figure 16 plots the total wafer price as a function of yield for three different duty rates. The polysilicon is left unburdened in this plot. All prices are in 1977 dollars. The horizontal line depicts the JPL 1986 total wafer price goal. One readily sees that a wide range of duty rates and yields falls below the goal, allowing a variety of optimization possibilities. As a fairly reasonable projection, an EFG multiple ribbon production unit with a yield of 90%, the JPL 1986 goal, and standard duty cycle of 83% would produce ribbon blanks at a value-added price of $11.8/m^2$, a poly price of $4.1/m^2$, or a sum total market price of under $16/m^2$, less than 75% of the JPL goal.

D. <u>Multiple and Single Ribbon Growth</u>

Single ribbon growth has occasionally been proposed as a potentially cost-effective technology. Mobil Tyco has done extensive work in both the single and multiple EFG growth areas, and is convinced that multiple ribbon growth is the only alternative capable of attaining economic iability in a large-scale market. This conclusion is quantified below.

59

Table XII. 1 of 100 Production Units: Cost Breakdown.

```
EQUIPMENT
    FURNACE LIFETIME SUBSYSTEMS         ($)          40000.00
    CARTRIDGE LIFETIME SUBSYSTEMS        "           45000.00
    CONTROL EQUIPMENT                    "           15000.00
    MELT REPLENISHMENT SUBSYSTEMS        "            9000.00
    TOTAL EQUIPMENT                      "          109000.00

FLOOR SPACE
    AREA FOR ONE PRODUCTION UNIT       (SQ FT)         165.00

DIRECT LABOR
    DIRECT LABOR PAY RATE              ($/RUN)         560.00
    TOTAL LABOR                        ($/YR)        29120.00

MATERIALS
    FURNACE INSULATION                ($/RUN)          38.46
    HEATING ELEMENTS                     "             19.23
    CRUCIBLE                             "             80.00
    MELT REPLENISHMENT MATERIALS         "             40.00
    DIE                                  "             20.00
    CARTRIDGE MATERIALS                  "            100.00
    FURNACE ARGON                        "             48.34
    CARTRIDGE ARGON                      "            114.48
    CARTRIDGE HELIUM                     "            137.38
    TOTAL MATERIAL                    ($/YR)        31089.98

UTILITIES
    FURNACE POWER                     ($/RUN)         134.52
    CARTRIDGE AND MR POWER               "             85.54
    TOTAL UTILITIES                   ($/YR)        11442.91

QUANTITY
    OUTPUT FROM ONE RUN              (SQ M/RUN)        215.64
    TOTAL QUANTITY                   (SQ M/YR)       11213.43
```

PRICE1=(0.49(109000.)+97(165.)+2.1(29120.)+1.3(31090.)+1.3(11443.)/11213.
    = $ 16.57/SQ M

PRICE2=PRICE1+1.3(POLY COST)=PRICE1+1.3($ 4.66/SQ M)
    = $ 22.63/SQ M ($21.73/sq m if poly cost not burdened by 30%)

Table XIII. 1 of 100 Production Units: Price Breakdown.

```
EQUIPMENT
    FURNACE LIFETIME SUBSYSTEMS          ($/SQ M)         1.748
    CARTRIDGE LIFETIME SUBSYSTEMS            "            1.966
    CONTROL EQUIPMENT                        "            0.655
    MELT REPLENISHMENT SUBSYSTEMS            "            0.393
    TOTAL EQUIPMENT                          "            4.763

FLOOR SPACE
    AREA FOR ONE PRODUCTION UNIT             "            1.427

DIRECT LABOR
    DIRECT LABOR PAY RATE                    "            5.453
    TOTAL LABOR                              "            5.453

MATERIALS
    FURNACE INSULATION                       "            0.232
    HEATING ELEMENTS                         "            0.116
    CRUCIBLE                                 "            0.482
    MELT REPLENISHMENT MATERIALS             "            0.241
    DIE                                      "            0.121
    CARTRIDGE MATERIALS                      "            0.603
    FURNACE ARGON                            "            0.284
    CARTRIDGE ARGON                          "            0.698
    CARTRIDGE HELIUM                         "            0.828
    TOTAL MATERIAL                           "            3.604

UTILITIES
    FURNACE POWER                            "            0.811
    CARTRIDGE AND MR POWER                   "            0.516
    TOTAL UTILITIES                          "            1.327

QUANTITY
    OUTPUT FROM ONE RUN                  (SQ M/RUN)     215.643
    TOTAL QUANTITY                       (SQ M/YR)    11213.425
```

PRICE1= 4.763 + 1.427 + 5.453 + 3.604 + 1.327
      = $ 16.57/SQ M

PRICE2=PRICE1+1.3(POLY COST)=PRICE1+1.3($ 4.66/SQ M)
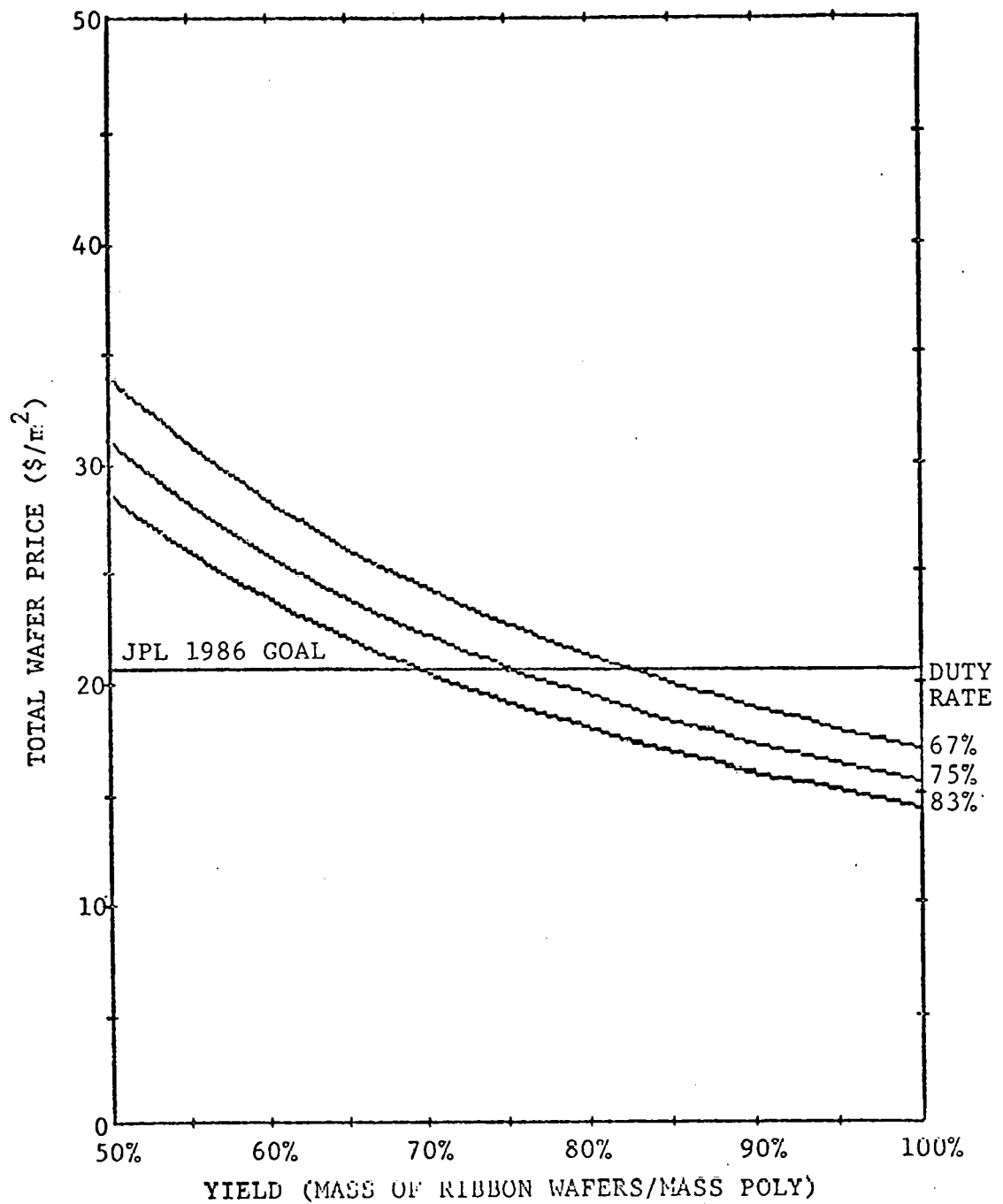   = $ 22.63/SQ M ($21.23/sq m if poly cost not burdened by 30%)

Fig. 16. Total wafer price vs. yield for 1 of 100 production units
(poly unburdened).

Table XIV details the input data set for a single ribbon furnace.
The various values for furnace items are based on our experience with
single ribbon growth. In this configuration, one must surround each
growth station with a separate furnace environment, and provide each with
melt replenishment. The heating elements and crucible costs are the
actual values for JPL Furnace 1. Growth station and melt replenishment
requirements remain unchanged. This is reflected in the part of the data
which remains constant. A ratio of almost 7 furnaces per operator was
used (i.e., 0.15 operators per furnace).

The data was fed into the SAMICS equation. Figure 17 gives the total
blank price for the single ribbon furnace and one multiple ribbon produc-
tion unit. The graph compares the burdened SAMICS terms. In all but
polysilicon material, multiple growth holds an edge in price, the latter
never exceeding three-fourths of the single ribbon furnace contribution
to price. Even in one were to assume a much higher duty rate for single
ribbon growth, which is not likely due in part to the need to attend
many furnaces as well as many ribbons, multiple ribbon growth proves more
economically attractive.

E. Sensitivity Analysis

The economic analysis model can determine the sensitivity of price
and quantity to all the input data terms. Much of this information is
evident in the cost and price breakdowns. Several of the more signifi-
cant terms are examined below.

The cartridge materials cost per run for a single production unit
contributes about $2.4/m^2$ to the total wafer price. Figure 18 illustrates
how the cartridge parts contribute to price as their replacement cost per
run varies over its possible range and beyond. The uncertainty in this
term, discussed above, indicates the minimum noise level of this particu-
lar technology projection. More importantly, cartridge materials will be
a large portion of the price if they actually cost about $30 or $40 per
run. From a purely economic standpoint, these parts should receive high
priority in future development efforts.

Gas costs provide another example of how this kind of technology
projecting economic analysis can feed back useful information to project
engineers. If one sets costs appropriate to large lot purchases (Tables
XI - XIII), the cartridge gas costs surface as the largest materials
contributors to price. The economic effect of reducing cartridge gas
flow is given in Fig. 19. A new 7.5 cm heat removal element has been
designed which should provide more efficient heat removal while lowering

Table XIV.   Input Data to Economic Analysis Model:
Single Ribbon Furnace.

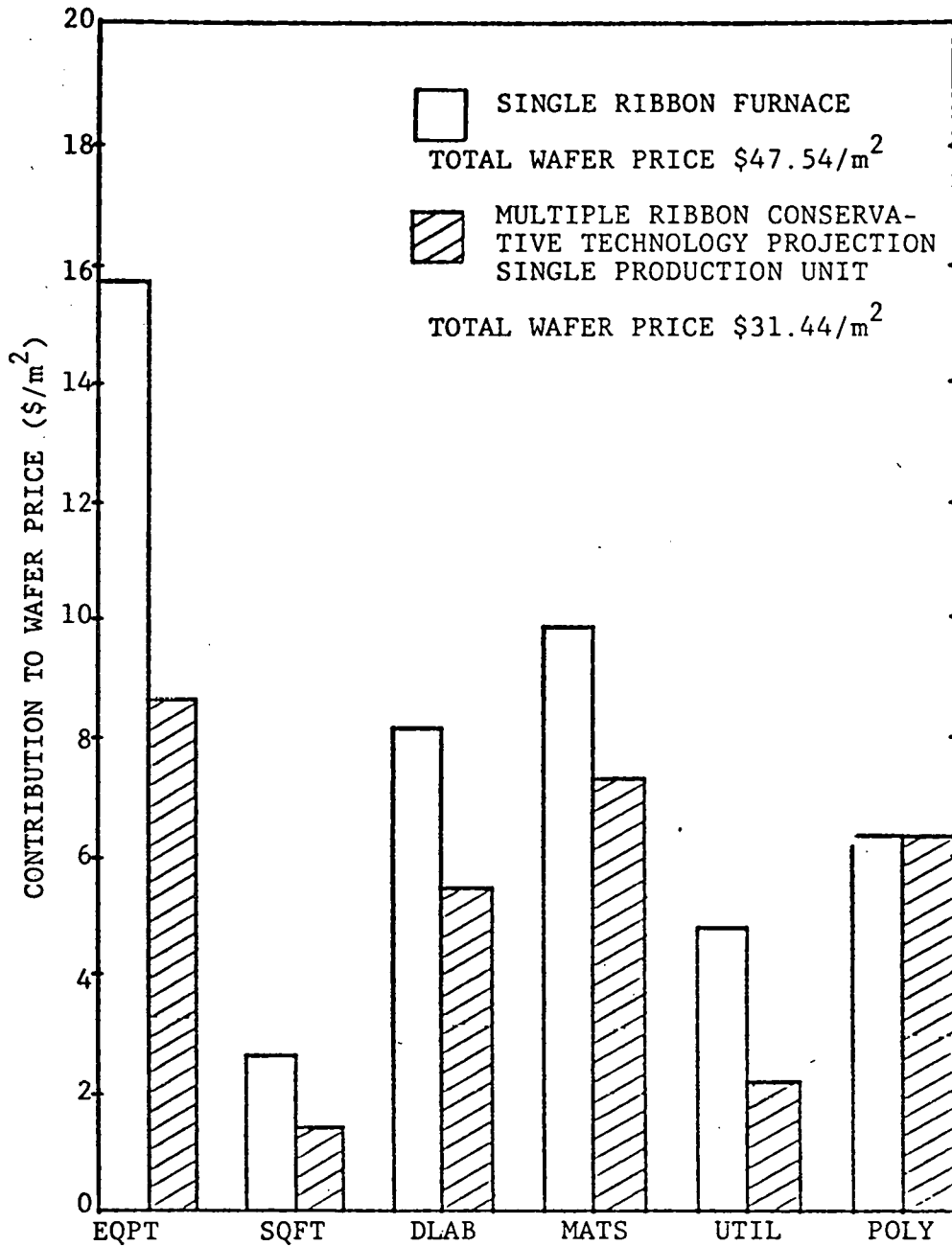|	SINGLE PRODUCTION UNIT	SINGLE RIBBON FURNACE	
Ribbon width (in.)	3.0	3.0	
Growth rate (in./min)	3.0	3.0	
Run length (hours)	116	116	
Number of runs per year	52	52	
Number of ribbons per furnace	5	1	+
Number of furnaces per production unit	2	1	+
Number of operators per production unit*	1	0.15	+
Yield (mass ribbon wafers/mass poly)	0.80	0.80	
Duty rate	0.67	0.67	
Polysilicon ($/kg)	10.0	10.0	
Dopant ($ dopant/$ poly)	0.1	0.1	
Thickness (in.)	0.006	0.006	
Furnace lifetime subsystems ($/furnace)	30000	15000	+
Cartridge lifetime subsystems ($/ribbon)	9000	9000	
Melt replenishment subsystems ($/furnace)	9000	9000	
Electro-optical controls ($/ribbon)	3000	3000	
Area for one production (sq ft)	165	30	+
Labor pay rate ($/hr)	5.00	5.00	
Furnace insulation ($/furnace)	2000	1000	+
Insulation lifetime (runs)	52.0	52.0	
Heating elements ($/furnace)	500	125	+
Heating elements lifetime (runs)	26.0	26.0	
Crucible ($/furnace)	400	66.50	+
Crucible lifetime (runs)	5.0	5.0	
Melt replenishment materials ($/furnace/run)	40.00	40.00	
Die ($/ribbon)	10.00	10.00	
Die lifetime (runs)	1.0	1.0	
Cartridge materials ($/ribbon/run)	40.00	40.00	
Argon ($/100 cu ft)	2.35	2.35	
Helium ($/100 cu ft)	8.48	8.48	
Electricity ($/kwh)	0.05	0.05	
Furnace argon flow rate (ft^3/hr/furnace)*	10.0	2.0	+
Cartridge argon flow rate (ft^3/hr/ribbon)*	5.0	5.0	
Cartridge helium flow rate (ft^3/hr/ribbon)*	2.0	2.0	
Furnace power consumption (kw/furnace)*	20.0	10.0	+
Cartridge power consumption (kw/ribbon)*	2.2	2.2	

*Modes of time-dependent variables.
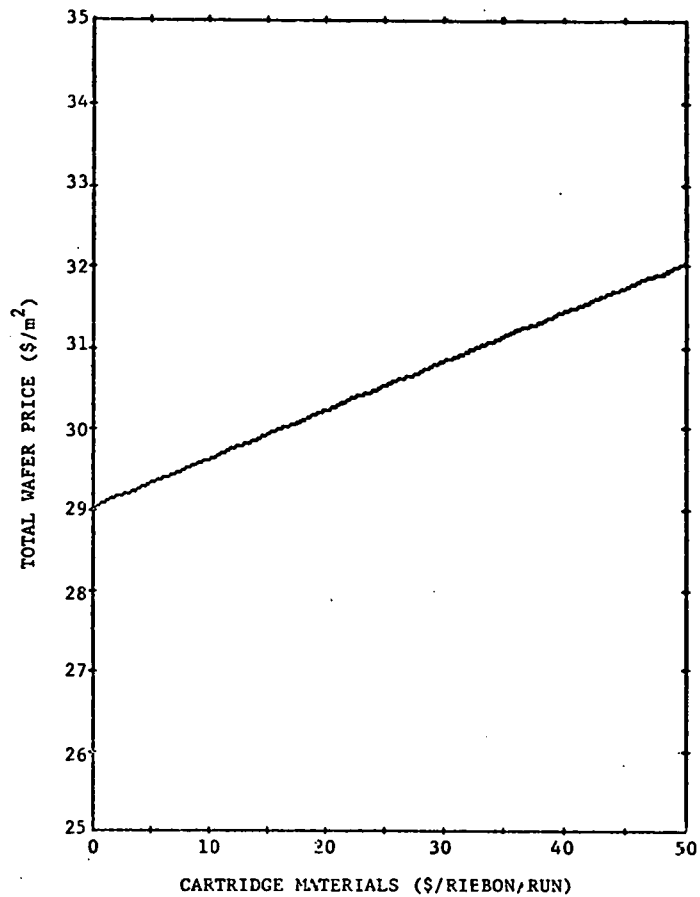
64

Fig. 17. Single vs. multiple ribbon growth.

Fig. 18. Total wafer price vs. cartridge
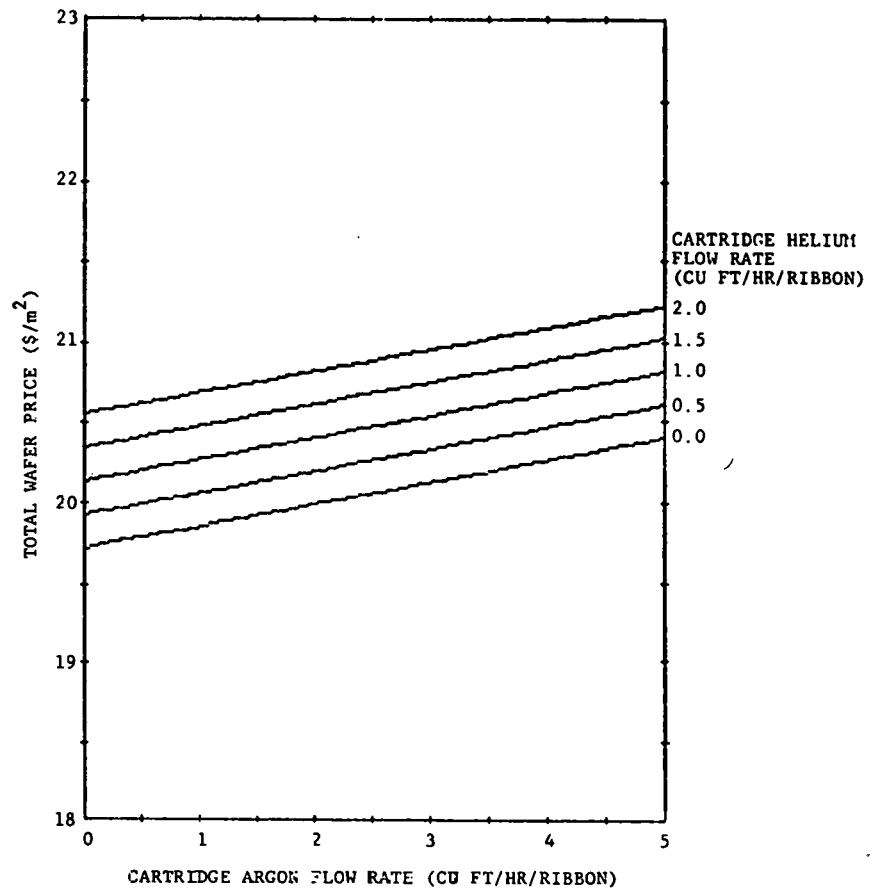materials for a single produc-
tion unit.

Fig. 19. Total wafer price vs. cartridge gas flow
rates for 1 of 100 production units (poly
unburdened).

gas flow rates well below their present levels, thus decreasing the overall blank price.

The contribution of the poly to the total wafer price is a simple function proportional to poly cost, ribbon thickness, and burdening on cost, and inversely proportional to the yield, the ratio of mass of cell quality wafers to mass of poly. It depends only on these variables.

Figures 20 and 21 show four model sensitivity analyses for variations in each of these variables. The burdening increases the poly contribution to price by 30% according to the SAMICS materials coefficient of 1.3. Dopant costs are left out of these plots.

Three points can be made. First, and most important, cost optimization requires a high yield process, especially at higher poly prices. Note that these graphs only go down to a yield of 50%.

Burdening makes a significant difference. At lower yields, a 30% cost increase means more in terms of dollars per square meter. JPL cost goal calculations and SAMICS both assume a sequence of autonomous companies. SAMICS assumes no interfirm packaging-unpackaging or transportation, and further, does not include marketing and distribution costs of a final product. In light of the large effect burdening has on poly contribution to wafer price, not to mention the burdening of wafer cost on cell price, etc., if the credibility of these assumptions is not firmly established, the given JPL value-added price goals might lead to a much higher total module dollars per watt figure than the goal for the given target year.

Finally, thickness is an important variable in poly price, as the difference between 6 mil and 8 mil ribbon readily shows. However, due to breakage losses, yield is a non-linear function of thickness. Thus, it cannot be concluded from these graphs that thinner is better.

These plots reflect the thickness and yield parameters which best fit EFG technology. A conversion from the appropriate units of any other sheet growth technology (e.g., slice plus kerf and process yield) to those used here will give the same curves. The results are general.

F. Conclusions

Table XVa and XVb summarize the numerical output of the economic analysis model for the four EFG technology projections that have been postulated. The most noticeable feature in Table XVa is the cost reduction which attends the introduction of the wider and faster growing dual furnace production unit and the subsequent expansion to a large-scale plant setting. The results evident from Figure 17 are reproduced. These
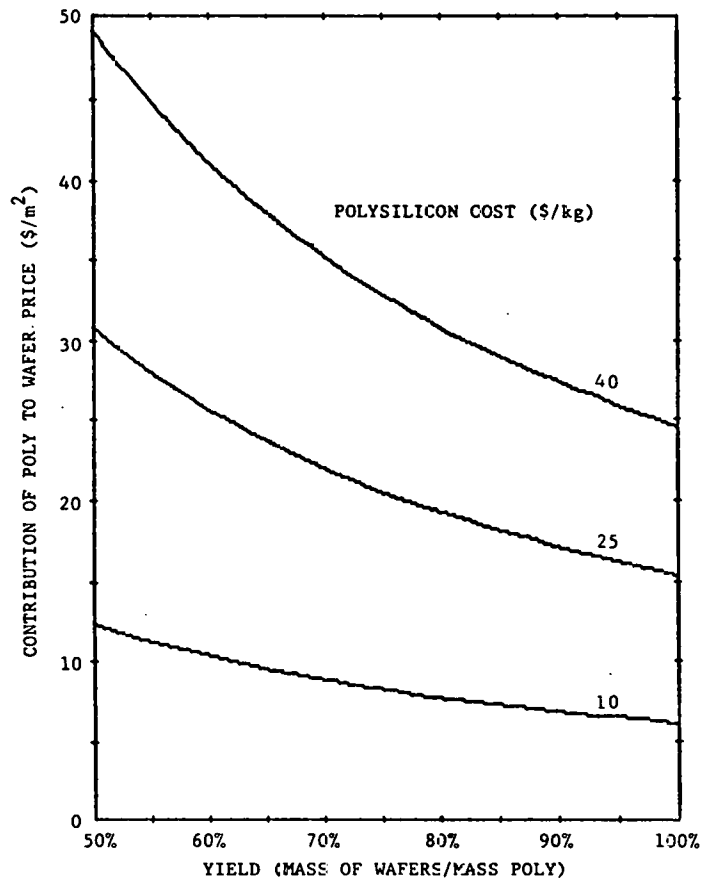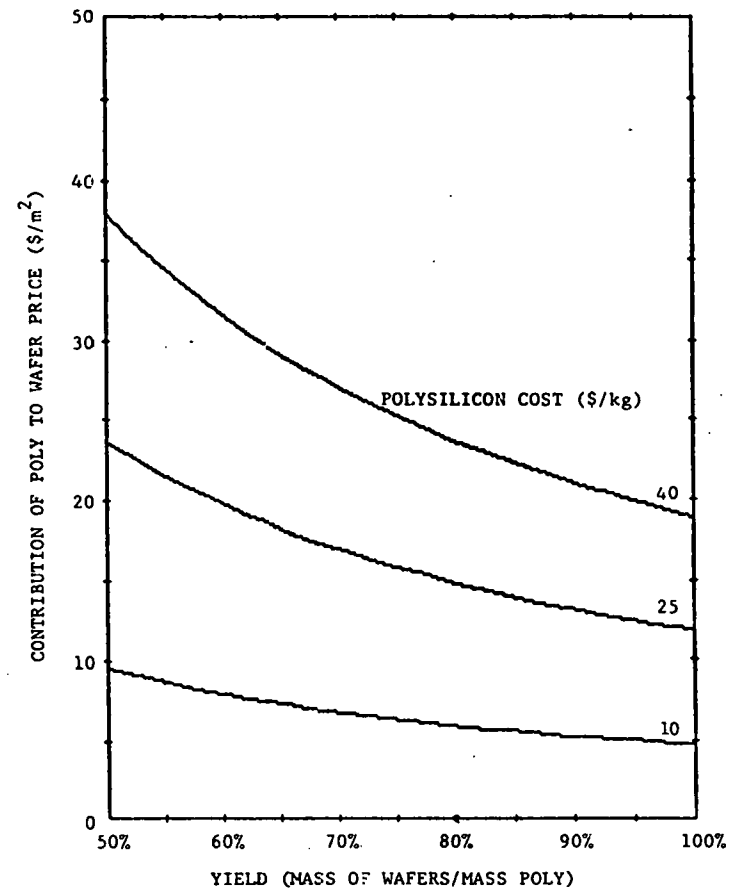
Fig. 20. Contribution of poly to total wafer price;
(a) thickness = .008 in., burdened, (b)
thickness = .008 in., unburdened.

(a)

(b)

Fig. 21.   Contribution of poly to total wafer price;
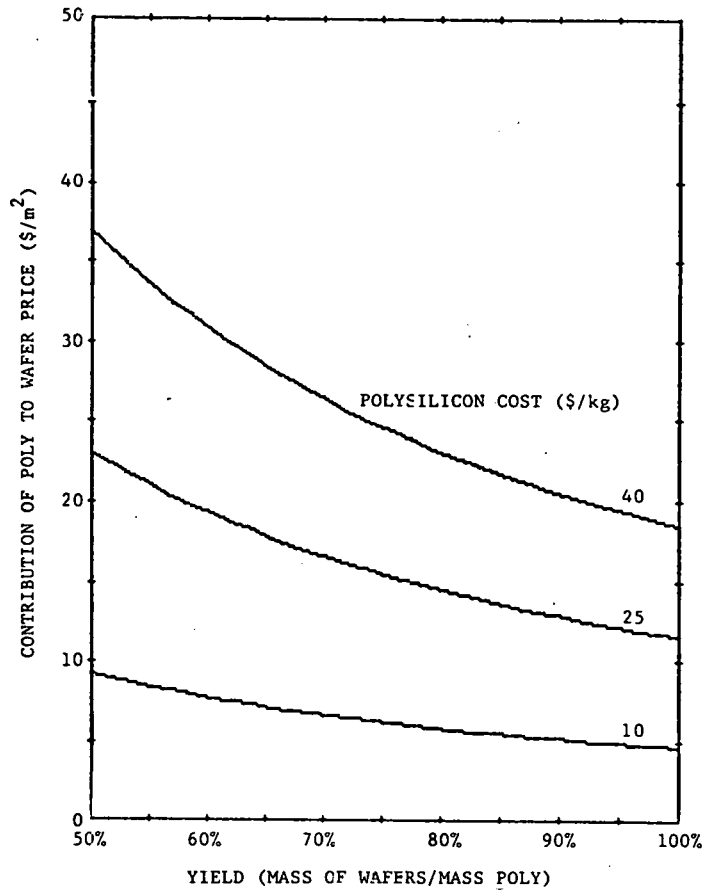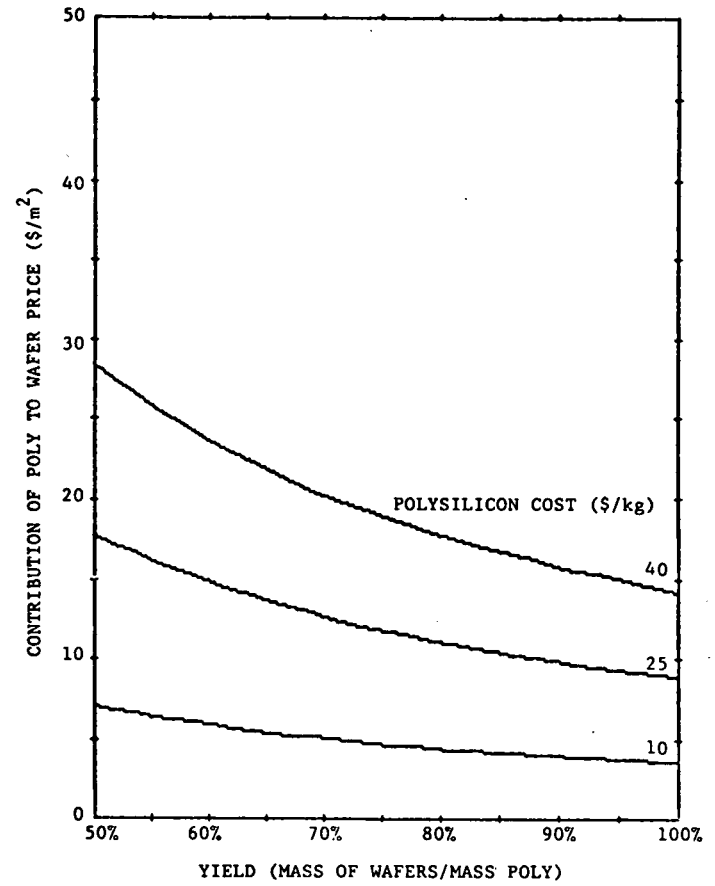(a) thickness = .006 in., burdened, (b)
thickness = .006 in., unburdened.

Table XVa. Distribution of Prices for Each Technology Projection ($/m^2).

Price Categories	End of 1978	Single Production Unit	1 of 100 Production Units	Single Ribbon Furnace
Equipment	23.96	8.65	4.76	15.73
Floor Space	4.79	1.43	1.43	2.60
Direct Labor	30.20	5.45	5.45	8.18
Materials	21.19	7.35	3.60	9.87
Utilities	6.12	2.21	1.33	4.81
Total Value-Added Price	86.26	25.09	16.57	41.19
Poly	72.92	6.34	4.66*	6.34
Total Blank Price	159.18	31.43	21.23	47.53

*Poly unburdened.

Table XVb. Percent Distribution of Prices for Each Technology Projection.

Price Categories	End of 1978	Single Production Unit	1 of 100 Production Units	Single Ribbon Furnace
Equipment	27.8	34.5	28.7	38.2
Floor Space	5.6	5.7	8.6	6.3
Direct Labor	35.0	21.7	32.9	19.9
Materials	24.6	29.3	21.7	24.0
Utilities	7.1	8.8	8.0	11.7
Total Value-Added Price	100	100	100	100
Poly	84.5	25.3	28.1*	15.4
Total Blank Price	185	125	128	115

*Poly unburdened

imply that multiple ribbon growth utilizes the furnace and plant environment more efficiently than single ribbon growth.

An examination of Table XVb reveals an interesting fact. The price distribution of the large-scale technology projection does not differ substantially from the near-term projection for JPL 3A (except, of course, for the poly contribution). As in Table XVa, Table XVb quantifies Fig. 17, illustrating the capital intensity of single ribbon growth. Single ribbon growth is also less sensitive to poly cost, even though the actual magnitude of the contribution to price is the same as in multiple growth.

Four major conclusions can be drawn from the economic analysis of EFG sheet growth technology.

- Multiple is more economically viable than single ribbon growth.

- The near-term (end of 1978) projection for JPL Machine 3A of about $160/m^2 undercuts the JPL 1980 total wafer price goal by $120.* If one uses a poly cost of $25/kg, the same projection meets the JPL 1982 total wafer price goal with a market price of about $112/m^2.

- A dual furnace production unit with ten 7.5 cm by 7.5 cm/min growth stations and one operator (duty rate 83%, yield 90%) scaled to 1986 output levels would produce silicon blanks at a market price under $16/m^2, less than 75% of the 1986 JPL goal.

- A high yield sheet growth process is favored, as polysilicon contribution to price increases and becomes more sensitive to poly cost, thickness and degree of burdening as the yield decreases. All of these factors are significant, even at higher yields.

The revisions made in the economic analysis model insure that economic technology projections reflect the present status of multiple ribbon growth. Equipment costs, parts costs and lifetimes, power consumptions and gas flow rates are either actual values or conservative estimates grounded in present data. The accuracy of the projections could be increased with a more certain and articulate input data set. The degree of experience in multiple ribbon technology limits the accuracy at present. The use of SAMICS allows EFG to be compared with other sheet growth technologies on a uniform market price basis.

These economic projections indicate that EFG multiple ribbon growth is capable of undercutting JPL goals in the LSSA Project by wide margins with the present technology and its end development, a multiple ribbon

---

*Utility of the material would, however, be dependent on the quality achieved as it expresses itself in solar cell efficiency at that time.

furnace which grows 7.5 cm ribbon at 7.5 cm/min, if the technology is capable of attaining the duty rates and yields (including the all-important solar cell quality factor!) posited at the given growth dimensions. These are the most crucial terms in the projections. Sensitivity analysis can aid in isolating areas which require greater engineering thrust, but such optimization is of minor importance relative to the need for a moderately reliable, high yield growth system. If these latter objectives can be met, multiple ribbon EFG becomes an extremely attractive prospect for the production of silicon sheet.

VII. REFERENCES

1. F.V. Wald et al., "Large Area Silicon Sheet by EFG", Annual Progress Report, ERDA/JPL 954355/77-3 (September 1977).

2. A.D. Morrison et al., "Large Area Silicon Sheet by EFG", Fourth Quarterly Progress Report, ERDA/JPL 954355/76-4 (December 1976).

3. T. Kato, T. Matsukawa, H. Koyama, K. Fujikawa, and R. Shimizu, J. Appl. Phys. 46, 2288 (1975).

4. W.H. Hackett, Jr., J. Appl. Phys. 42, 3249 (1971).

5. M. Neuberger et al., Hughes Aircraft Co., Culver City, California, "Silicon", AD698342, National Technical Information Service, U.S. Dept. of Commerce (October 1969).

6. Robert W. Aster and Robert G. Chamberlain, "Interim Price Estimation Guidelines: A Precursor and Adjunct to SAMIS III", Version One, JPL 5101-33, September 10, 1977.

THIS PAGE

WAS INTENTIONALLY

LEFT BLANK

APPENDICES

1. __Updated Program Plan__

   The original program plan, as amended, is still in effect.

2. __Man Hours and Costs__

   Previous cumulative man hours were 25,966 and cost plus fixed fee was $928,422. Man hours for the fourth quarter are 8,266 and cost plus fixed fee is $290,204. Therefore, total cumulative man hours and cost plus fixed fee are 34,232 and 1,218,626, respectively.

3. __Engineering Drawings and Sketches Generated During the Reporting Period__

   Figure 5, capillary bridge system.

4. __Summary of Characterization Data Generated During the Reporting Period__

   They are detailed in Section IV of this report. Of significance were findings that the cross-sectional structure does not materially affect the efficiencies of solar cells prepared from such ribbons. Also, cells which have efficiencies of ~10% are shown. These cells originated from the multiple furnace (Machine 3B) and demonstrated that fluid flow effects could be used to manipulate impurities in the ribbon leading to purification of the center section.

5. __Action Items Required by JPL__

   None.

6. __New Technology__

   New technology items are being separately reported, pending possible patent action.

7. "Impurity Redistribution in EFG" by J.P. Kalejs, submitted for publication to Journal of Crystal Growth.

THIS PAGE

WAS INTENTIONALLY

LEFT BLANK

APPENDIX 7

IMPURITY REDISTRIBUTION IN EFG

J.P. Kalejs

Mobil Tyco Solar Energy Corporation
16 Hickory Drive
Waltham, Massachusetts 02154, USA

Numerical solutions of convective and diffusive transport equations in the melt contained by the EFG capillary die are presented for a two-dimensional model of EFG of silicon ribbon. Die geometry is shown to influence convective impurity transport in melt supplying the interface region during growth. Nonuniformity in the component of melt velocity parallel to the growth interface gives rise to impurity redistribution across the width of the ribbon. Enhancement of impurity levels above those of the bulk melt is associated with regions of low velocity, depletion of levels with regions of high velocity. The degree of redistribution varies with growth speed and the interface segregation and liquid diffusion coefficients of the impurity species. The close relation between redistribution patterns and die geometry suggests levels of certain impurities in preselected regions of the ribbon may be controlled by die design.

1. INTRODUCTION

Interest has been growing in the edge-defined film-fed growth (EFG) method for pulling single crystals of predetermined cross section from the melt. This method was initially used in the growth of sapphire [1]; now it is being considered seriously for the preparation of silicon ribbon suitable for low cost solar cell manufacture [2]. Although much theoretical and experimental work on the EFG system for silicon has been reported [3], efforts have not yet extended to the study of fluid flow and impurity transport in the melt. An understanding of impurity transport is central to the ability to control the quality of melt grown crystals. The present calculations have been motivated by a desire to be able to predict the distribution of impurities potentially harmful to solar cell performance in silicon ribbon grown by EFG. This paper will present the results of numerical modelling of impurity transport in this system.

The EFG system differs from most crystal growth methods for which melt impurity transport has been studied in that growth takes place from a liquid meniscus film confined to the top of a die wetted by the melt, i.e., a capillary die. The primary function of the EFG die is to shape the cross section of the growing crystal. The die also contains the capillary path by which melt is supplied to the growth interface.

As a consequence of melt flow during growth, convective flow patterns are set up in the melt ahead of the solid-liquid interface. In EFG, the patterns can be fixed by choice of the die top and capillary geometry. This convection will be termed "die capillary" convection to emphasize its close relationship to EFG die geometry. Convective transport may also take place as a result of surface tension driven flow [4] and thermal convection [5]. The present analysis is restricted to a study of impurity transport by diffusion and die capillary convection. The latter will be shown to exert a direct influence on the melt impurity transport which controls impurity concentration levels in silicon ribbon.

grown by EFG.

The first part of the paper (Section 2) discusses EFG die configurations for silicon ribbon growth and the model for impurity transport in the system. In Section 3, the method of solution of the time-independent momentum and diffusion equations in two dimensions is outlined. Section 4 presents results of the calculations for EFG die configurations of interest in growth of silicon ribbon. Section 5 discusses the results, the limitations of the analysis and suggestions for experimental work.

2. IMPURITY TRANSPORT MODEL

2.1 EFG SYSTEM DESCRIPTION

A typical EFG system melt and die configuration used in silicon ribbon growth is shown schematically in fig. 1. The melt is drawn up to the die top by capillary action. The ribbon is pulled from the melt confined within a liquid meniscus film at the die top by surface tension forces. The position of the growth interface above the die top, i.e., the meniscus height, is a function of the growth conditions and die geometry. Their interrelationships have been discussed elsewhere [3]. The present work will examine impurity transport by convection and diffusion in the melt contained by the die and liquid meniscus film. For this purpose, the meniscus height will be regarded as fixed and independent of convective flow patterns or impurity concentrations in the melt.

The path of the melt through the die capillaries and the liquid meniscus film at the die top is fixed by the choice of die geometry. Die capillary configurations representative of those used in silicon ribbon growth are shown in cross section in fig. 2. In fig. 2a, the die top is fed by evenly spaced capillaries. The choice of the capillary cross section and arrangement is dictated by considerations of capillarity (i.e., die material) and viscous drag [2]. In most cases, a slot extends full width along the die top and enlarges the melt volume below the growth interface. Other forms of capillary feed are by means of a

channel cut either in the ends of the die, as in fig. 2b, or in the center, as in fig. 2c. Additional die modifications are possible in the shaping of the die top. These are not considered to be essential to the understanding of basic transport phenomena and the discussion is, therefore, restricted to planar die top surfaces.

2.2 CONVECTIVE AND DIFFUSIVE TRANSPORT

A three-dimensional model is required to fully account for convection and diffusion of impurities in the melt of the die and liquid meniscus film in both the width (w) and thickness (t) dimensions of a growing ribbon. A complete solution using numerical schemes with the help of a computer clearly would be time-consuming and costly. Fortunately, the wide, very thin aspect (w >> t) of the silicon ribbon growth systems currently of interest lends itself to a two-dimensional approach. Approximations inherent in such an approach will now be examined.

Melt is supplied to the growth interface by convection in the die capillaries, the die top slot, and the liquid meniscus film. The flow will be, to a good approximation, in the plane of the die cross sections shown in fig. 2 aside from viscous boundary layer constriction in the thickness dimension. Deviations from this two-dimensional flow due to the curvature of the meniscus in the thickness dimension will be minimal when growth takes place such that the ribbon and die top slot thicknesses are equal. In this case, the three-dimensional nature of the meniscus film at the die top has much reduced impact because the flow through the die top slot and film is likely to be predominately in a channel of constant (rectangular) cross section perpendicular to the growth direction. Convection out of the plane of the die width cross section may also arise from variations in the ribbon thickness, surface tension driven convection, or a mismatch of the capillary and die top slot dimensions perpendicular to this plane.

The relative importance of diffusion and convection in the transport of impurities is gauged by the Peclet number, Pe, defined Pe = VL/D. Here, V is the speed characterizing the convective flow, L is a typical distance over which com-

parison of the two transport mechanisms is to be made, and D is the melt impurity diffusion coefficient. With the help of the Peclet number, regimes may be defined for which either convection or diffusion is the dominant mechanism of impurity transport: Pe >> 1 implies transport is convection dominated, while for Pe << 1, it is diffusion limited. For Pe ~ 1, both mechanisms have a comparable influence on transport.

The extreme aspect ratio of the ribbon growth system considered here has important implications for the study of impurity transport. For very wide but thin ribbons it is possible to satisfy simultaneously both of the inequalities,

$$Pe_t = V_t L_t / D \ll 1, \qquad Pe_w = V_w L_w / D \gg 1. \tag{1}$$

V_t and V_w are characteristic melt flow speeds in the ribbon thickness and width dimensions, respectively; L_t and L_w are the respective characteristic distances of the order of the ribbon thickness and width. In this regime, impurity transport across the ribbon thickness is diffusion limited while convection dominates in the ribbon width dimension. Within the scope of the model, the conditions needed for the inequalities of eq. (1) to hold are fulfilled in the EFG of silicon ribbon. In addition, it can be argued that diffusion limited transport in the thickness dimension cannot appreciably perturb convective transport in the plane of the ribbon width.

The calculation of combined convective and diffusive transport in the melt contained by the die and the meniscus will be carried out for the die cross sections of the type illustrated in fig. 2. To simplify matters further, the calculation is restricted to a planar growth interface. Curvature of the meniscus film at the die edges is also neglected. In a rough-walled capillary tube, such as may be the case if the die is made of graphite, transition to turbulent flow takes place when the Reynolds number, referred to tube diameter and average flow velocity, exceeds 2000. In the calculations reported below for silicon melt flow,

the Reynolds number remains below 200. It follows that melt flow in the die is laminar at the silicon ribbon growth speeds of interest.

3. SOLUTION PROCEDURE

The transport equations and boundary conditions for which solutions are reported below are given in the Appendix. The calculation domains for the velocity and concentration fields are shown in figs. 3 and 4, respectively. These domains incorporate the various capillary arrangements in fig. 2. A finite difference scheme [6] is used to solve the eqs. (A1) ·· (A7) numerically for the velocity and concentration fields. Nonuniform grids are employed with 18 x 18 nodal points in the x- and y- directions, respectively. A finer grid line spacing is used near the growth interface in all calculations and in the capillary exit region when needed to resolve detail there.

Only dilute concentrations of impurities in the melt are of interest here. In this situation, the concentration dependence of the momentum equations can be neglected. The solution procedure for the combined momentum and diffusion equations is now considerably simplified. The velocity field can first be calculated for the domain shown in fig. 3 independently of the concentration field. The velocity data are then available as input for the solution of eq. (A6) for $C(x,y)$ in the reduced domain of fig. 4.

The auxiliary condition on velocity in the region of the domain of fig. 3 occupied by the die, as expressed in eq. (A5), is imposed by assigning viscosity values a factor of the order of 10^8 larger than those of the melt at the appropriate nodal points. Although they never fall to zero, the velocity values at the nodal points within the high viscosity region are depressed by factors of 10^5 or more below those in the melt. This scheme effectively simulates the presence of the die material.

Velocity and concentration field solutions are parameterized by the growth speed, the segregation and diffusion coefficients for the impurity species in

liquid silicon, and the ratio of die to capillary half width, w_d/w_c. In order to simplify discussion of the results, the die parameters w_d, h, and h_s for all the reported calculations are fixed at values representative of the dies shown in figs. 2b and 2c. These are w_d = 4 cm, h = 1.5 cm, and h_s = 0.25 cm. In principle, the results are also applicable to the die configuration of fig. 2a with 2 w_d = 8 cm as the capillary spacing; however, such large capillary spacings are not useful in practice. Liquid and solid silicon densities of 2.53 and 2.30 gm/cm^3, respectively, and a dynamic melt viscosity of 0.0088 poise are used in all the velocity field calculations.

4. RESULTS OF CALCULATIONS

The results of the calculations are presented in figs. 5 - 7 as graphs of the interface concentration ratio, C_s/C_o, against position along the width of the ribbon. The origin of the coordinate system for the die configuration of fig. 2c is on the capillary centerline; the same curves apply to the configuration of fig. 2b, with the origin displaced to the left-hand edge of the die. The solid interface concentration, C_s, has been obtained from the calculated interface concentration in the melt using the equilibrium segregation coefficient, as in eq. (A8). Equilibrium segregation coefficients in silicon are known for most impurities. Diffusion coefficients in the liquid have not been extensively measured, and there is disagreement in the literature over a number of the values. Because of the uncertainty in many of the latter, the input values of k_o and D for the calculations have been chosen to span a range which encompasses the reported data for impurities in liquid silicon.

Solid interface concentration profiles for impurities with different segregation coefficients but comparable diffusion coefficients are shown in fig. 5. An impurity with a value of k_o close to unity (k_o = 0.8) is boron. Its diffusion coefficient in liquid silicon has been measured by two different experimental techniques [7,8], and the results agree to within a factor of two. The average value

is used in the present calculation. The transport mechanisms modelled here cause only minor redistribution of boron in the melt. The resulting variation in C_s/C_o is less than one percent across the width of the ribbon. The situation is quite different for an impurity of comparable diffusion coefficient but a segregation coefficient much less than unity. Order of magnitude variations in C_s/C_o are predicted to occur for an impurity with $k_o = 10^{-3}$ and $D = 10^{-4}$ cm^2/sec; for the same D but a lower value of k_o, the predicted variation in C_s/C_o increases to range over more than three orders of magnitude. For this die configuration, re-distribution of impurities in the melt near the interface takes the form of a region of depressed concentration above the capillary exit with levels increasing to above C_o in the regions downstream from the exit.

The calculations have been extended to investigate the effect of changes in growth velocity and die geometry on the interface concentration distribution across the ribbon width for an impurity with $k_o = 10^{-5}$. The results at two growth speeds for each of two values of w_d/w_c are presented in figs. 6 and 7 for impurity diffusion coefficients in the range between 10^{-5} and 10^{-3} cm^2/sec. For $D = 10^{-5}$ cm^2/sec, C_s/C_o is essentially uniform across the full width of the ribbon in all cases examined. Impurity redistribution at the interface in the melt has significantly altered C_s/C_o already for $D = 10^{-4}$ cm^2/sec. Redistribution continues to become more pronounced with an increase in diffusion coefficient. For $w_d/w_c = 2$ (fig. 6), a minimum in the melt interface concentration is predicted for the region above the capillary edge. Both above the capillary center and in the melt furthest downstream, the concentration levels are higher. Enhancement of solid impurity levels above C_o occurs in the section of the ribbon furthest removed from the capillary exit. The concentration maximum above the capillary decreases both in relative magnitude (with respect to the minimum) and in extent with a decrease in capillary width (at constant w_d). At $w_d/w_c = 20$ (figs. 5 and 7), this maximum is not resolved on the scale of the graph. The concentration minimum now essentially

encompasses the entire region above the capillary. An increase in growth speed from 0.042 to 0.125 cm/sec leads to an increase in concentration levels in the region of the minimum with both die geometries. Compensating decreases in concentration occur at points downstream from the capillary exit region. The boron concentration distribution remains essentially uniform, as in fig. 5, over the same ranges of growth speeds and w_d/w_c values. The ratios of the maximum to the minimum value of C_s/C_o across the ribbon width are summarized in Table I for the cases examined and discussed above.

5. DISCUSSION

Forced convection has long been recognized as an important means for controlling the impurity distribution in crystals pulled from the melt. For example, stirring of the melt is used to advantage in Czochralski growth to reduce impurity inhomogeneity arising from thermally induced convection as well as to control the thickness of the impurity boundary layer ahead of the growth interface. Convection is also responsible for the impurity redistribution predicted for EFG of silicon ribbon on the basis of the above calculations. A feature which distinguishes the latter is that the convection pattern, and hence impurity redistribution in the melt near the interface, is controlled by a growth system component unique to EFG - the capillary die. Moreover, this imparts additional significance to EFG die design because growth cannot take place without the melt supply provided by this die capillary convection.

5.1 DIE CAPILLARY CONVECTION

This section will examine briefly the effect of convective flow near a growth interface on diffusive transport and illustrate how die capillary convection can lead to impurity redistribution in the case of EFG of ribbon. In steady-state growth at a speed V_g, an impurity boundary layer of extent, or thickness, of the order of D/V_g is known to form ahead of the growth interface as a result of impurity segregation [9]. This boundary layer is indicated schematically in fig. 8

by a plot of the melt impurity concentration against a coordinate measured into the melt from the interface as origin. The interface melt concentration, C_I, for each species differs according to its segregation coefficient and its level in the bulk melt. In particular, for one-dimensional growth with an effective segregation coefficient of unity, eq. (A8) gives $C_I = C_o/k_o$. Impurity concentration levels are uniform across the width of the ribbon for melt flow that is one-dimensional, i.e., directed normal to the growth interface. In the growth system modelled here, melt flow near the interface is not uniform. This has important consequences for interface impurity redistribution along the width of the ribbon.

Nonuniformity in die top melt velocities in silicon ribbon growth arises because the melt flow channel connecting the bulk melt to the growth interface varies in cross section (see fig. 2). For the die geometries considered, lateral melt flow parallel to the interface (in the ribbon width direction) is set up to supply melt to regions of the ribbon not directly above a capillary exit. The degree of nonuniformity in the lateral flow velocities is a function of the growth velocity and the die top slot and capillary geometry. In addition, viscous resistance to lateral flow at the growth interface gives rise to a momentum, or velocity, boundary layer. This is represented in fig. 8 by a plot of the horizontal component of melt velocity, u, superimposed on the concentration boundary layer graph. The momentum boundary layer thickness will vary with the lateral melt speed at the edge of the boundary layer. Overlap of the impurity and momentum boundary layers allows the former to respond to nonuniformity in lateral flow speeds, which may then result in lateral impurity redistribution.

A general feature of the convection patterns for two-dimensional flow with the die configurations modelled is the presence of zones of recirculating melt, or vortices, in the die top slot. These are set up by viscous forces in regions of separated flow extending downstream from the capillary edge along the bottom

of the die top slot. For example, two such zones will be formed between each pair of adjacent capillaries in the die configuration of fig. 2a. For the die geometries and growth speeds under consideration here, recirculation is minimal. Actual reverse flow does not extend to more than .02 cm (<0.1 h_s) above the bottom of the die top slot. However, the zones of recirculation have been found to extend over an appreciable portion of the die top slot for a die configuration such as that shown in fig. 2a [10]. When melt which must be supplied to the interface region downstream of the recirculation zone is constricted to flow in a narrower channel in order to bypass a zone of separated flow, nonuniformity in u can be greatly enhanced. In a real growth situation, the vortex might exert a destabilizing influence in the convection pattern near the interface.

5.2 IMPURITY REDISTRIBUTION

The results of the calculations given in figs. 6 and 7 can be explained by reference to fig. 8. The points of melt inflow to the die top slot are fixed by capillary geometry. Maximum capillary melt flow speeds vary with V_g roughly in proportion to the ratio w_d/w_c. The horizontal component of velocity outside of the momentum boundary layer also varies with V_g, although not in the same proportion. The maximum values of u occur in the neighborhood of the capillary edges; u is zero along a line of symmetry, such as between adjacent capillaries (fig. 2a), or along the die centerline and edges (figs. 2b and 2c). The C_s/C_o minima in figs. 6 and 7 are associated with regions of the highest u, enhancement of C_s relative to C_o with regions of lower u. Just such impurity redistribution can be expected to result from a readjustment of impurity concentration levels in response to nonuniformity in the melt flow, as impurities rejected in regions of high lateral velocity are swept to regions of lower velocity. The relationship of C_s/C_o to u is illustrated in fig. 9. Further, the minimum in C_s/C_o follows the region of highest velocities as the capillary width is decreased in going from

w_d/w_c = 2 to 20, as is evident in figs. 6 and 7.

An increase in V_g results in a decrease in the boundary layer thickness of a given impurity (i.e., given k_o and D) in proportion to V_g^{-1}. If the thickness of the impurity and momentum boundary layers is of the same order, this decrease will generally reduce the extent of the overlap of the two boundary layers. In addition, the momentum boundary layer is a region of decreasing values of the horizontal component of velocity as the interface is approached, as depicted in fig. 8. Therefore, as the impurity boundary layer thickness decreases, lateral convective transport becomes less effective in redistributing impurities within it. This can account for both the decrease in the ratio of the maximum to minimum values of C_s/C_o (see Table I) and the increase in C_s/C_o at the concentration minimum (see figs. 6 and 7) predicted with increasing V_g. Higher maximum values of u also accompany the increase in V_g. If the nonuniformity in u in the width dimension increases as a result, this could be expected to accentuate impurity redistribution and decrease C_s/C_o at the minimum. The first of the above effects is predicted to dominate the response of C_s/C_o at the minimum, while the second can be important in regions of enhanced C_s (as for D = 10^{-4} cm^2/sec in fig. 7).

Since the impurity boundary layer extent varies as D/V_g, an argument similar to the first one given above for the response of C_s/C_o to increases in V_g can explain the response of redistribution to decreases in D. At the growth speeds considered, redistribution has effectively disappeared for D ~ 10^{-5} cm^2/sec. The impurity boundary layer now no longer extends sufficiently far into the momentum boundary layer to enable the impurity levels to respond to lateral convective transport.

In another case, increasing the ratio w_d/w_c by decreasing w_c accentuates the nonuniformity in the lateral melt flow speed but does not change the melt flow speed normal to the interface. The melt interface concentration levels associate with the minimum in C_s/C_o are reduced in response to a higher rate of lateral con-

vective transport. Finally, the greater degree of redistribution observed with decreasing k_o below unity appears to be a consequence of the corresponding increase in impurity flux into the melt. The latter varies according to the local rate of impurity rejection, given by the last of the conditions in eq. (A7), which increases proportionally to $(1 - k_o)$ as k_o falls below unity.

5.3 IMPURITIES IN SILICON

The two impurity parameters which play the central role in the redistribution effects predicted above are the diffusion coefficient in the melt and the equilibrium segregation coefficient. These are tabulated in Table II for a number of impurities in silicon. The values of k_o range from lows of 10^{-7} to near unity. The measured values of D in liquid silicon fall in the range between 1×10^{-5} to 6×10^{-4} cm^2/sec. The disagreement in the published values of D is largest for aluminum, gallium and indium, where measurements differ by more than an order of magnitude.

The results presented in fig. 5 show redistribution in silicon is a strong function of k_o. For example, it was noted already that boron, with $k_o = 0.8$, is unaffected by the redistribution mechanism. This is of considerable significance because boron is a common dopant for solar cell silicon material and it is, therefore, desirable to have it incorporated uniformly into the solid during growth. In general, redistribution is minor (and insensitive to die geometry) for those impurities with k_o greater than about 0.1 for which D has been measured. Phosphorous and arsenic fall in this category in addition to boron. Redistribution for carbon ($k_o = 0.07$) is predicted to result in a variation of C_s/C_o of less than three percent in the most extreme case for the die configurations examined. Redistribution effects for antimony are also predicted to be relatively weak.

The possibility of significant redistribution increases for impurities with k_o much less than unity. Redistribution is also more sensitive to the magnitude of the diffusion coefficient over the range of values of D expected on the basis

of the reported data listed in Table II. As a consequence, it is not possible

to judge the extent of redistribution for aluminum, gallium and indium because

of the wide spread in their reported diffusion coefficients. For example, re-

distribution for aluminum is predicted to lead to a variation in C_s/C_o through

several orders of magnitude for the highest reported D (typified by the curve for

$k_o = 10^{-5}$ and $D = 10^{-4}$ cm^2/sec in fig. 5); yet, for the lowest reported $D = 0.24$

x 10^{-4} cm^2/sec, the variation in C_s/C_o is reduced to span less than an order of

magnitude and confined to the capillary exit region.

A number of impurities with very low values of k_o $(<10^{-4})$ - such as iron,

chromium, titanium - are known to be detrimental to solar cell performance in

silicon [15]. Diffusion coefficients for these impurities have not been measured

in liquid silicon. The results of the calculations for $k_o = 10^{-5}$ presented in

figs. 6 and 7 show that redistribution for low k_o impurities results in a varia-

tion in C_s/C_o by several orders of magnitude for most die configurations already

when $D = 10^{-4}$ cm^2/sec (see also Table I). The magnitude of the redistribution

for one of the above, iron, could be of this order. The diffusion coefficient

for iron in solid silicon near the melting point is reported to be ~2 x 10^{-5} cm^2/

sec [17]. For those impurities for which the liquid diffusion coefficient in

silicon has been measured (see Table II), it is found to be orders of magnitude

greater than in the solid [17]. Even though the diffusion coefficient for iron

in solid silicon is anomalously high in comparison to these others, it seems

unlikely it would be lower in the liquid state than in the solid. Thus, a some-

what higher value of D in the liquid state, say an increase over the solid value

by a factor of five to $D = 10^{-4}$ cm^2/sec, would mean that iron is redistributed

in the manner shown in figs. 6 and 7.

5.4 EFFECTIVE SEGREGATION COEFFICIENT

It has been proposed that steady-state EFG proceeds with a system effective

segregation coefficient of unity [18]. Experimental work lends some support to

this view [19]. Factors which will work toward establishing this condition in

EFG of silicon ribbon are fast growth speeds and long capillary paths from the

bulk melt to the interface. In the context of the present model, conditions of

growth with a system effective segregation coefficient of unity are established

when impurities segregated at the growth interface are confined to the die top and

capillary melt, as represented in the calculation domain of fig. 3.

As noted above, a measure of the extent of the impurity boundary layer ahead

of the growth interface is the ratio D/V_g. The maximum value this ratio attains

for the parameters used in these calculations is of the order of 0.025 cm (for

$D \sim 10^{-3}$ cm^2/sec and $V_g \sim 0.04$ cm/sec). This is about one-tenth of the die top slot

dimension, h_s, and of the order of the height of the liquid meniscus film above

the die top under typical silicon ribbon growth conditions [3]. The calculated

diffusion-related impurity flux down the capillary does not exceed one-tenth of

one percent of the convective inflow for any of the calculated die top concentra-

tion fields. Therefore, the rate of impurity incorporation into the growing ribbon

is, for practical purposes, equal to the impurity influx to the die top melt by

convection via the capillaries, and growth takes place with an effective segrega-

tion coefficient of unity in the sense defined above.

The present analysis does not allow for impurity removal from or addition to

the melt contained in the die by mechanisms other than incorporation into the grow-

ing solid. Two likely alternate paths are through interaction with the die

surface and vapor phase transport via the meniscus film surface. The system effec-

tive segregation coefficient for growth under these conditions would no longer be

unity. However, since information regarding these alternate processes is lacking,

extension of the analysis to include such effects is not warranted at this time.

5.5 MODEL LIMITATIONS

The development of a tractable two-dimensional model for impurity transport

during EFG of silicon ribbon has necessarily required a simplified representation of complex growth conditions. Restrictions placed on the applicability of the model as a result of simplifications are examined below.

(i) Convection arising from the flow of melt to the interface during growth has been the only form of convective impurity transport modelled here. The possibility also exists of convective flows being set up by temperature and concentration gradients in the melt. Convection set up by density changes associated with temperature differences in the interior of the melt has been termed thermal convection [5]. The type of flow pattern that may arise depends, among other parameters, on the thermal conditions and the geometric configuration of the melt. The Rayleigh number is used as a gauge of the threshhold for the onset of thermal convection. The dominant temperature gradient in the EFG melt is found along the growth direction and is estimated to be as high as 1000°C/cm at fast growth speeds. (Temperature gradients in the die width and thickness dimensions are very small because of an effort to keep the die top isothermal during growth.) The Rayleigh number is estimated to be less than 1000 at the extreme even for the highest temperature gradients because of the offsetting small melt volumes contained in the die top slot and liquid meniscus film. This appears to be far enough below the range of critical Rayleigh numbers required for the onset of thermal convection (2000 and above) to render the possibility of occurrence of these flows unlikely.

It has been suggested that convection driven by temperature-induced surface tension differences (thermocapillary convection) can have a significant impact on temperature and impurity concentration fields in liquid silicon melt [4]. As a consequence of EFG die geometry and the thermal field configuration noted above, thermocapillary convection associated with the dominant temperature difference will be in the plane of the ribbon thickness and confined to the portion of the die top melt bounded by the meniscus film surface. The melt is forced toward the

growth interface on the surface of the meniscus film and returns in the center of

the thickness cross section. Fluid at a temperature above the melting point is

brought to the interface by this flow. For the large temperature differences

expected in the meniscus film in EFG (up to 25°C), the flow could be very vigor-

ous [4]. Its effect on die capillary convection and impurity transport across the

ribbon width is difficult to predict. One possible result could be to broaden the

interface impurity boundary layer by distributing impurities more homogeneously

throughout the meniscus film volume. It should be kept in mind that thermocapillary

flow will oppose die capillary convection supplying melt to the central part of the

interface. Consequently, it appears unlikely the stable growth conditions observed

in practice during EFG of silicon ribbon [10] could be achieved if this flow were

to exist over a fraction of the die top melt volume large enough to significantly

alter impurity transport or convection across the ribbon width.

The convective flow pattern in the meniscus film could be further complicated

by impurity-induced surface tension driven convection. The effect of impurities

on liquid silicon surface tension is not known. It is quite possible that these

surface tension driven flows are confined to a relatively thin melt layer at the

surface of the meniscus film and do not appreciably perturb the interior melt flow

patterns. The effectiveness of surface tension gradients in setting up melt con-

vection could be greatly reduced by contamination of the meniscus film by the

influx of impurities from the vapor phase. (In EFG of silicon ribbon, in parti-

cular, SiO and oxides of molybdenum are present as evidenced by deposits on cooler

parts of the furnace interior.) Vapor transport could lead to saturation of the

meniscus surface with impurities to the point where the surface tension would no

longer respond to bulk melt concentration gradients.

(ii) Convective and diffusive impurity transport in the ribbon width dimen-

sion have been modelled without regard to transport processes that may be opera-

tive in redistributing impurities across the ribbon thickness. The validity of

this approach will now be examined with the aid of the Peclet number concept. Although it is not strictly applicable in regions of rapidly varying concentrations or velocities, such as in a boundary layer, it is still instructive to use it as a criterion to judge the importance of transport processes in certain limiting situations.

It follows from the discussion of Section 2.2 and the definition of the Peclet number that the range of diffusion controlled impurity transport, L, in a melt with average speed, V, is of the order of D/V. In one-dimensional growth with speed V_g, the impurity boundary layer is thus confined to a distance of the order of D/V_g from the growth interface. The impurity boundary layer thicknesses obtained in the present two-dimensional calculation are also of this order. On the other hand, aside from the momentum boundary layer, the melt flow speeds in the ribbon width dimension are of the order of V_g or greater. For the range of D and V_g encountered in the present analysis, $w_d \gg D/V_g$. The second of the inequalities of eq. (1) is thus easily satisfied for $L_w \sim w_d$ and $V_w \sim V_g$ and die top melt impurity transport is convection dominated in these circumstances. Even when the impurity boundary layer lies within the momentum boundary layer, melt flow parallel to the interface turns out to be of a sufficient magnitude to enable convection to redistribute impurities within the boundary layer in many instances. The question now remains as to the nature of the impurity transport in the ribbon thickness dimension and its influence on the calculated redistribution across the ribbon width.

Typical thicknesses of EFG silicon ribbon are of the order of 0.025 cm. Melt velocities in the plane of the ribbon thickness will vary with die top geometry. For matching die top slot and ribbon thicknesses, the bulk of convective flow supplying melt to the growth interface will be directed normal to the plane of the interface. Making use of eq. (1) for $V_t \sim 0$, then $Pe_t \sim 0$. In the absence of the surface tension driven flows discussed in (i) and with no contribution from

die capillary convection, diffusive transport, which could arise as a result of curvature of the interface, is left as the only mechanism for impurity transport in the plane of the ribbon thickness. These conditions are ones for which the melt flow in the die most closely approximates the calculated two-dimensional flow fields. It may now be argued that if impurity transport is diffusion limited in the plane of the ribbon thickness, perturbations of convection dominated transport characterized by a velocity $\sim V_g$ in the plane of the ribbon width will be minimal as long as diffusion is restricted to act over distances $D/V_g \ll w_d$. In the presence of surface tension driven convection, this conclusion may not be valid. However, a more complicated model for impurity transport than that developed here will necessarily be required to include the effects of convective and diffusive transport across the ribbon thickness.

(iii) In the modelling of impurity transport in EFG of silicon ribbon, it has been assumed that impurity segregation at the growth interface proceeds under equilibrium conditions and that the interface segregation coefficient takes on the equilibrium value k_o. Experimental evidence from a number of melt growth systems suggests that the rate at which impurities are incorporated into the solid is a function of the growth speed [20]. Typical growth speeds for EFG of silicon ribbon, such as those considered here, are generally a factor of ten to one hundred greater than those encountered in the systems for which growth speed-related effects have been observed. It should be expected, therefore, that if departures of the interface segregation coefficient from its equilibrium value do take place, they should be in evidence at the speeds used in EFG of silicon ribbon.

It is argued that the interface segregation coefficient will tend towards unity in the limit of infinitely fast growth speeds. A number of theories have been advanced to attempt to account for this variation. Most of these incorporate the concept of a reaction constant or reaction "velocity" proportional to the ratio D_s/λ where λ is a distance of the order of the interatomic spacing and D_s is

the solid diffusion coefficient. The interface segregation coefficient is a function of $V_g \lambda / D_s$, approaching unity for $V_g \to \infty$. It is of particular interest in the case of silicon that the solid diffusion coefficients near the melting point, and hence the reaction velocities, for a number of the impurities considered above fall roughly into two categories: one having D_s in the range between 10^{-11} to 10^{-9} cm^2/sec, such as for aluminum, phosphorus, indium, gallium and arsenic; the other having much higher values of 10^{-6} cm^2/sec and above, such as for iron, copper and zinc [17]. The interface segregation coefficient at a given growth speed is predicted to depart more from k_o and approach closer to unity for impurities in the group with low D_s than in the group for which D_s is many orders of magnitude greater. For example, it may be argued on the basis of these theories that the interface segregation coefficient for an impurity such as iron increases by several orders of magnitude above k_o during EFG at the high speeds encountered in silicon ribbon growth. The impurity redistribution predicted on the basis of the present model is sensitive to changes in k_o, all other parameters being held constant. The possible variation of the interface segregation coefficient with growth speed and consequent departure from k_o would then have to be accounted for in any attempt to use the predicted impurity redistributions of this model in the interpretation of experimental data.

5.6 SUGGESTIONS FOR EXPERIMENTAL WORK

In many situations, it is of primary importance to grow material with homogeneous properties insofar as impurity content is concerned. For the EFG system configurations studied, impurity redistribution was shown to be directly related to nonuniformity in the die top melt velocity in the ribbon width dimension. Nonuniform velocities and the accompanying impurity redistribution can be avoided by extending the capillary of the EFG die so the interface is fed by melt uniformly along its entire width. Since EFG at the growth speeds considered takes place with a system effective segregation coefficient of unity, ribbon grown from a die

with uniform melt feed along its width will have a homogeneous impurity distribution along both its length and its width.

On the other hand, it is interesting to consider possible benefits to be gained from the ability to influence the impurity content of preselected sections of a crystal by appropriate die design. Two situations in which it may prove to be advantageous will be examined. The discussion will be restricted to a consideration of EFG of silicon ribbon, although the concepts could as well be applied to other materials that can be grown by EFG or by other crystal growth methods which utilize a die.

One possibility to consider is whether potentially undesirable impurities can be "swept" to regions of the ribbon that are disposable for material end-use purposes. A general feature of impurity redistribution in EFG is the enhancement of concentration levels in sections of ribbon growing from above some regions of the die top melt in which the component of velocity parallel to the interface is zero. This has been noted to be the case at the die centerline for a configuration such as that shown in fig. 2b, and at the die edges for the die in fig. 2c. Conversely, impurity levels are predicted to be depleted in material grown from above the capillary edge. Knowledge of the lateral extent of the regions of enhanced and depleted levels is thus of primary importance in the design of die configurations which could take advantage of redistribution to grow inhomogeneous material with sections of high impurity concentration that are to be discarded. The impurity parameters figuring most prominently in the redistribution are the interface segregation coefficient and the liquid diffusion coefficient.

The possibility of "in situ purification" of a predetermined section of the ribbon has application in the case of silicon ribbon grown for solar cell manufacture. Impurity redistribution for the growth configurations modelled is predicted to be the most pronounced for low k_o impurities; this includes a number known to be detrimental to solar cell performance, among those iron and titanium.

However, the liquid diffusion coefficients for these and other impurities with low k_o in this category are not known. The possibility that the interface segregation coefficient may vary with growth speed adds more uncertainty to the prediction of redistribution for a specific impurity. Experimental work will be needed to establish whether silicon ribbon with deliberately created inhomogeneity can be grown. Some preliminary experiments in this area have been performed [10]. The results appear to lend some credence to the feasibility of the concepts proposed here. However, the magnitude of the redistribution in silicon ribbon grown to date has been difficult to establish due to the complexity of the EFG growth system presently in use for high speed growth. Additional experiments are needed to determine if changes in ribbon material properties attributed to die design selection arise from redistribution of impurities by die capillary convection as proposed, or from other as yet undetermined causes.

In a second area of application of the concepts of impurity redistribution by die capillary convection, material inhomogeneity induced deliberately during growth could be used to provide information regarding the diffusion and interface segregation coefficients of impurity species measurably affected by redistribution. The experimental parameters available to do this are the growth speed and the die geometry. For example, inhomogeneous material could be grown by EFG from a melt intentionally doped with a low segregation coefficient impurity. The diffusion coefficient could be obtained from a fit of the theory to the measured impurity distribution. Competing processes for impurity transport in the melt make it necessary to design such experiments with great care. Possibilities for alternative transport mechanisms for EFG have already been discussed in Section 5.5. It is also not established whether the effect on impurity redistribution due to variations of the interface segregation coefficient with growth speed can be identified on the basis of available theories.

It is important to recognize the central role of the growth speed as an aid

to future experimental work in the areas proposed above. The calculations pre-sented here have investigated a restricted speed range of current interest in growth of silicon ribbon [10] and demonstrate the main features of impurity re-distribution by die capillary convection. These growth speeds span only a small interval of the overall range available in EFG systems. The EFG technique has now been used to grow material at speeds covering more than three orders of magnitude, from those considered here (~0.1 cm/sec) to below 0.0001 cm/sec [21]. This wide range implies considerable flexibility for experimentation.

The response of the impurity redistribution ahead of the growth interface to changes in growth speed has been attributed to interaction between the momentum and impurity boundary layers. For example, the adjustment in the impurity dis-tribution predicted in going from 0.125 to 0.042 cm/sec is shown in figs. 6 and 7 for $k_o = 10^{-5}$. The most striking change is the increase in the predicted ratio of the maximum to the minimum value of C_s/C_o. For $D = 10^{-4}$ cm^2/sec, Table I shows the magnitude of the change is quite different for the two die geometries examined: by a factor of 40 for $w_d/w_c = 2$, but only by a factor of ~3 for $w_d/w_c =$ 20. The numerical effect of the decrease in V_g on the impurity boundary layer extent (i.e., the ratio D/V_g) may also be achieved by increasing D while keeping V_g constant. Changes in the calculated ratios of maximum to minimum C_s/C_o with either an increase in D or commensurate decrease in V_g are comparable (although never the same) for the die geometries investigated. Thus, the ratio D/V_g, rather than D or V_g alone, can be used as a measure of redistribution. However, the limitations of this argument must be recognized. If growth speed is lowered to the point where convection parallel to the interface (in the ribbon width dimen-sion here) no longer dominates diffusion transport, the degree of redistribution (as measured by the ratio of the maximum to minimum values of C_s/C_o) will decrease. From the considerations of Section 2.2, these transport mechanisms become compar-able for $Pc = \dfrac{V_g w_d}{D} \sim 1$, or when $D/V_g \sim w_d$ (neglecting momentum boundary layer

effects). Nevertheless, for a given die geometry and impurity species (given k_o and D), this line of reasoning may be of benefit in searching for the experimental configuration most suitable for studying redistribution effects in a given system.

6. CONCLUSIONS

Impurity transport in EFG of silicon ribbon by convection and diffusion has been investigated through numerical solution of the time-independent transport equations. Convection in the die top melt resulting from melt flow to supply the interface has been shown to influence redistribution of certain impurities across the ribbon width. Redistribution by this "die capillary" convection is uniquely related to die capillary and top slot geometry. At the growth speeds and for the die configurations investigated, the effective system distribution coefficient for all impurities is unity.

The redistribution of impurities across the silicon ribbon width has been calculated for two die configurations and for growth speeds of current interest in preparation of material for use in the manufacture of low cost solar cells. The degree of redistribution is found to vary with growth speed and die geometry and to be particularly sensitive to the values of the interface segregation coefficient and the liquid diffusion coefficient of the impurity species. Redistribution is predicted to be the most pronounced for impurities with low segregation coefficients ($k_o \leq 10^{-2}$) and large diffusion coefficients ($D \geq 10^{-4}$ cm^2/sec). Very minor redistribution is observed for all impurities with $D \sim 10^{-5}$ cm^2/sec. For a number of impurities with measured values of D, redistribution is also very weak if the interface segregation coefficient exceeds about 0.1.

Although the present analysis has been restricted to a consideration of EFG of silicon ribbon, the concept of impurity redistribution by die capillary convection is not limited in applicability to this growth system. The general features of the redistribution are depletion of impurity concentration levels in the region

of the interface above the capillary exit and enhancement downstream of it.
These are attributed to nonuniformity in the component of melt velocity parallel
to the growth interface. It is, therefore, possible for redistribution to arise
in all systems in which growth takes place from a die and nonuniformity in con-
vective flow parallel to the growth interface can be set up by an appropriate
choice of die design.

ACKNOWLEDGMENTS

APPENDIX

The time-independent two-dimensional momentum equations and continuity equa-
tion to be solved for the x- and y-direction velocity components $u(x,y)$ and $v(x,y)$,
respectively, are [22]:

$$\rho \left[u(\partial u/\partial x) + v(\partial u/\partial y) \right] = -(\partial p/\partial x) + \mu (\partial^2 u/\partial x^2 + \partial^2 u/\partial y^2), \qquad (A1)$$

$$\rho \left[u(\partial v/\partial x) + v(\partial v/\partial y) \right] = -(\partial p/\partial y) + \mu (\partial^2 v/\partial x^2 + \partial^2 v/\partial y^2), \qquad (A2)$$

$$\partial u/\partial x + \partial v/\partial y = 0. \qquad (A3)$$

Here ρ is the liquid density, μ is the dynamic viscosity and p is the pressure.
The calculation domain in which solutions for the velocity field are sought is
shown in fig. 3. Insofar as the fluid flow is concerned, the relevant die dimen-
sions are the capillary half width, w_c, the die top slot height, h_s, and a die half
width, w_d. The die top slot height dimension includes the height of the liquid
meniscus film above the die top. The choice of total die height, h, will not

affect convection near the interface provided the velocity profile is fully developed at the entrance of the die top slot.

The boundary conditions imposed on u and v for the calculation domain are:

$$u = 0, \quad \partial v/\partial x = 0; \qquad x = 0, \; 0 < y < h$$
$$x = w_d, \; h - h_s < y < h$$
$$u = 0, \quad v = V_i; \quad 0 < x < w_c, \; y = 0 \qquad \text{(A4)}$$
$$u = 0, \quad v = 0; \quad w_c < x < w_d, \; y = 0$$
$$x = w_d, \; 0 < y < h - h_s$$
$$u = 0, \quad v = V_g; \quad 0 < x < w_d, \; y = h$$

An auxiliary condition of zero melt velocity is needed in the regions of the domain occupied by die material. For the die configuration in fig. 3, the requirement is:

$$u = v = 0; \quad w_c < x < w_d, \quad 0 < y < h - h_s. \qquad \text{(A5)}$$

Both the inflow and outflow velocities are assumed to be uniform and directed along the y-axis. The velocity at the outflow boundary, V_g, is fixed at the start of each computation. The speed of the melt entering the die capillary, V_i, is calculated for each V_g by application of mass conservation to the melt at the inflow and to the solid at the outflow boundaries. The boundary condition for v(x,y) on the vertical melt boundaries is applicable either at a line of symmetry or a free melt surface under zero shear stress. The latter is a good approximation to the conditions expected at an ambient gas-melt interface. It should be recognized that the calculations model only die configurations for which the capillary and die top slot dimensions match in the plane perpendicular to that of the calculation.

The time-independent diffusion equation for the concentration field in two dimensions, C(x,y), is [22]:

$$u(\partial C/\partial x) + v(\partial C/\partial y) = D(\partial^2 C/\partial x^2 + \partial^2 C/\partial y^2) + S_c. \qquad \text{(A6)}$$

S_c represents a volume source (or sink) for the impurity species. The solution of

ɟ. (A6) is carried out in the reduced domain at the die top shown in fig. 4. The boundary conditions imposed on C(x,y) are:

$$\partial C/\partial x = 0; \qquad\qquad x = 0,\ 0 < y < h_s$$
$$x = w_d,\ 0 < y < h_s$$
$$w_c < x < w_d,\ y = 0 \qquad\qquad \text{(A7)}$$
$$C = C_o; \qquad\qquad 0 < x < w_c,\ y = 0$$
$$-D(\partial C/\partial y) = C(1 - k_o)V_g; \quad 0 < x < w_d,\ y = h_s$$

The lower boundary of the domain consists of the bottom of the die top slot and the capillary exit; the top is the solid-liquid interface. The side boundaries may be formed by either two lines of symmetry (as in fig. 2a) or one line of symmetry and one free meniscus surface (as in figs. 2b and 2c).

The inflow boundary condition of uniform melt concentration, C_o, neglects impurity redistribution by convection during melt flow up the capillary. Equilibrium conditions are assumed to hold at the growth interface, with the interface segregation coefficient equal to its equilibrium value, k_o. The solid impurity concentration, C_s, and the melt interface concentration, C_I, are then related according to:

$$C_s = k_o C_I. \qquad\qquad \text{(A8)}$$

This relation is implied in the use of the last of the conditions in eq. (A7), which sets the concentration gradient into the melt.

REFERENCES

1. H.E. LaBelle, Jr. and A.I. Mlavsky, Mater. Res. Bull. 6 (1971) 571; H.E. LaBelle, Jr., Mater. Res. Bull. 6 (1971) 581; B. Chalmers, H.E. LaBelle, Jr. and A.I. Mlavsky, Mater. Res. Bull. 6 (1971) 681.

2. K.V. Ravi, J. Crystal Growth 39 (1977) 1.

3. T. Surek, B. Chalmers and A.I. Mlavsky, J. Crystal Growth (in press).

4. C.E. Chang and W.R. Wilcox, J. Crystal Growth 28 (1975) 8.

5. For a review of the literature see J.R. Carruthers, J. Crystal Growth (1975) 12.

6. S.V. Patankar and D.B. Spalding, Int. J. Heat and Mass Transfer 15 (1972) 1787.

7. H. Kodera, Jap. J. Appl. Phys. 2 (1963) 212.

8. Yu. M. Shashkov and V.M. Gurevich, Russ. J. Phys. Chem. 42 (1968) 1082.

9. J.A. Burton, R.C. Prim and W.P. Slichter, J. Chem. Phys. 21 (1953) 1987; A.I. Gubanov and S. Yu. Davydov, Bull. Acad. Sci. USSR, Phys. Ser. 35 (1971) 405.

10. F.V. Wald et. al., Annual Progress Report, ERDA/JPL 954355/77-3 (September 1977) (unpublished).

11. F.A. Trumbore, Bell System Tech. J. 39 (1960) 205.

12. B.M. Turovskii, Russ. J. Phys. Chem. 36 (1962) 983.

13. T. Nozaki, Y. Yatsurugi and N. Akiyama, J. Electrochem. Soc.: Solid State Science 117 (1970) 1566.

14. G.G. Gnesin and A.I. Raichenko, Porosh. Met. 13 (1973) 35.

15. R.H. Hopkins, J.R. Davis, P. Rai-Choudhury, P.D. Blais, J.P. McHugh, R.G. Seidensticker and J.R. McCormick, Fifth Quarterly Report, ERDA/JPL 954331/77-1 (December 1976) (unpublished).

16. V.M. Glazov, S.N. Chizhevskaya and N.N. Glagoleva, Liquid Semiconductors (translated from the Russian) (Plenum Press, New York, 1969) Ch. 3.

17. A.G. Milnes, Deep Impurities in Semiconductors (John Wiley and Sons, New York, 1973) p. 29.

18. J.C. Swartz, T. Surek and B. Chalmers, J. Electronic Mat. 4 (1975) 255.

19. S. Matsumara and T. Fukuda, J. Crystal Growth 34 (1976) 350.

20. For a discussion of these results see J.C. Brice, The Growth of Crystals from Liquids, Selected Topics in Solid State Physics, Vol. 12, E.P. Wohlfarth, Ed. (North Holland, Amsterdam, 1973) Ch. 3.

21. C.B. Finch, J.D. Holder, G.W. Clark and H.L. Yakel, J. Crystal Growth 37 (1977) 245.

22. V.G. Levich, Physicochemical Hydrodynamics (translated from the Russian) (Prentice-Hall, Englewood Cliffs, N.J., 1962).

Table I. Ratio of the Maximum to the Minimum Value of C_s/C_o Predicted for Silicon Ribbon Growth with Die Parameters w_d = 4 cm, h_s = 0.25 cm and h = 1.5 cm.

k_o	D (cm^2/sec)	w_d/w_c	V_g (cm/sec)	C_s/C_o Ratio
0.8	2.5×10^{-4}	2 to 20	0.042 to 0.125	~1
10^{-3}	1×10^{-4}	20	0.125	10
10^{-5}	1×10^{-5}	2	0.042	~1
		2	0.125	~1
		20	0.042	~1
		20	0.125	~1
	1×10^{-4}	2	0.042	2×10^2
		2	0.125	5
		20	0.042	1×10^4
		20	0.125	3.5×10^3
	1×10^{-3}	2	0.042	8×10^4
		2	0.125	3×10^4
		20	0.042	3.5×10^5
		20	0.125	2×10^5

Table II. Equilibrium Distribution Coefficients, k_o, and Liquid Diffusion Coefficients, D, in Silicon. The Values of k_o, Except as Noted, are from the Compilation in Ref. (11).

Impurity	k_o	D ($\times 10^4$ cm^2/sec)*
Cu	4×10^{-4}	-
Ag	2.5×10^{-5}	-
Zn	$\sim 10^{-5}$	-
B	0.8	1.8^a , 3.3^b
Al	0.002	$0.24 - 0.37^c$, 5.3^a
Ga	0.008	0.66^b, 3.6^a
In	4×10^{-4}	0.17^b, 5.2^a
C	0.07^d	0.485^e
Sn	0.016	-
P	0.35	2.7^b , 3.9^a
As	0.3	2.5^a
Sb	0.023	1.1^a , 1.4^b
Bi	7×10^{-4}	-
S	10^{-5}	-
Ti	3.6×10^{-6f}	-
Ta	10^{-7}	-
Cr	1.1×10^{-5f}	-
Mn	$\sim 10^{-5}$	-
Fe	8×10^{-6}	-
Co	8×10^{-6}	-
Ni	10^{-6}	-

*The reported literature values in Refs. (7) and (12) have been recalculated using μ = 0.88 cp (Ref. (16)). The value of μ used to obtain D in Ref. (8) is not given. a. Ref. (7); b. Ref. (8); c. Ref. (12); d. Ref. (13); e. Ref. (14); f. Ref. (15).
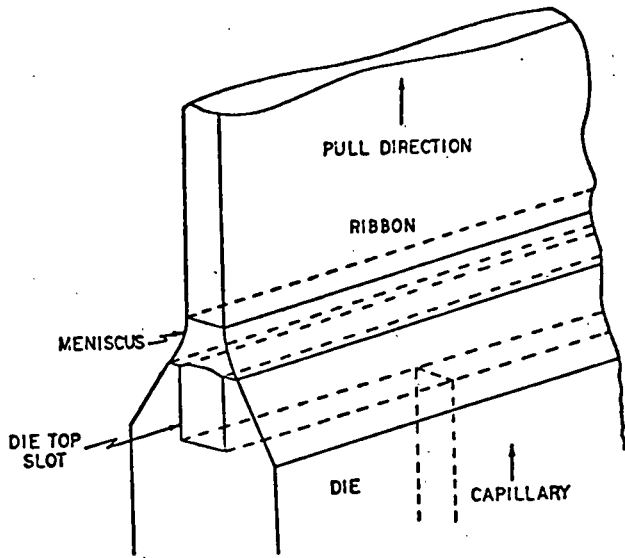
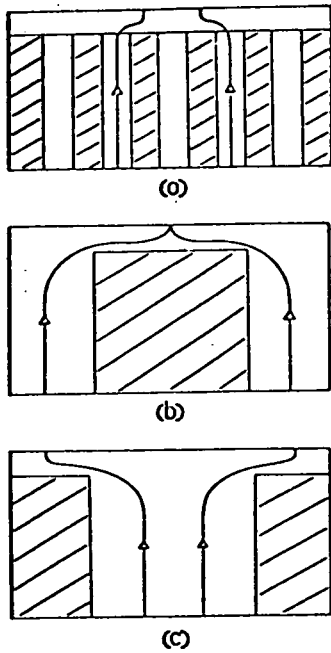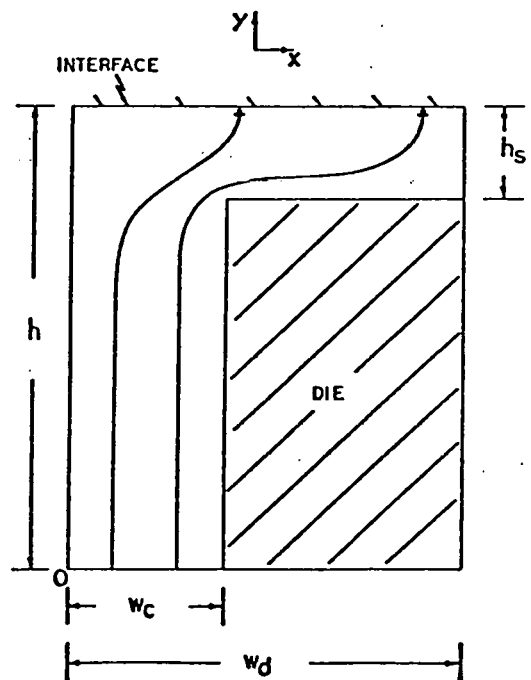Fig. 1. Schematic of EFG melt and die configuration in silicon ribbon growth.

Fig. 2. Schematics of ribbon die cross sections showing several capillary arrangements: (a) multi-capillary die; (b) side channel die; (c) central channel die.

Fig. 3. Calculation domain in cross section of die width for velocity field solution. The coordinate system origin is at 0.
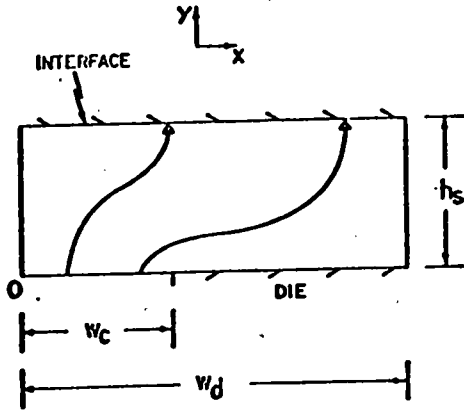
107

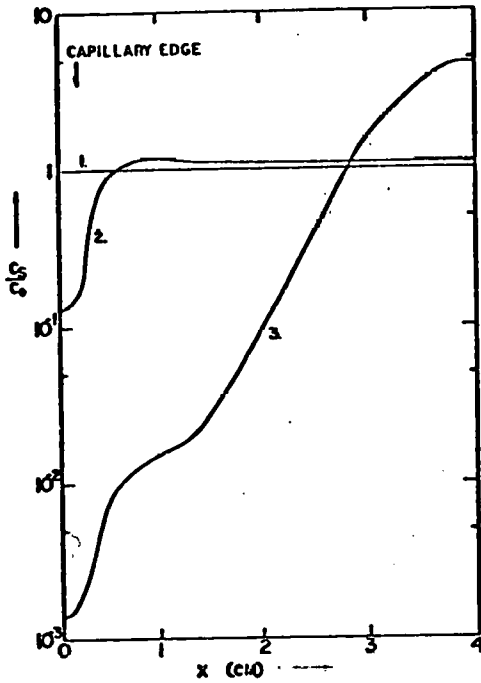Fig. 4. Calculation domain in cross section of die width for concentration field solution. The coordinate system origin is at 0.

Fig. 5. Interface concentration ratio in the solid, C_s/C_o, along the ribbon width for $w_d/w_c = 20$ and $V_g = 0.125$ cm/sec. Graph parameters:

1. $k_o = 0.8$, $D = 2.5 \times 10^{-4}$ cm^2/sec
2. $k_o = 10^{-3}$, $D = 10^{-4}$ cm^2/sec
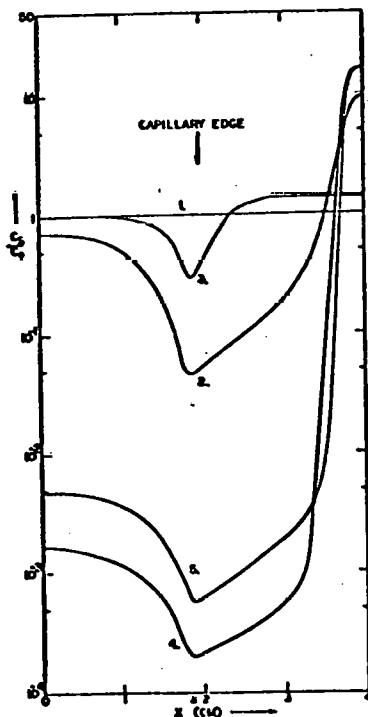3. $k_o = 10^{-5}$, $D = 10^{-4}$ cm^2/sec

Fig. 6. Interface concentration ratio in the solid, C_s/C_o, along the ribbon width for $w_d/w_c = 2$ and $k_o = 10^{-5}$. Graph parameters:

1. $D = 10^{-5}$ cm^2/sec, $V_g = 0.042$, 0.125 cm/sec
2. $D = 10^{-4}$ cm^2/sec, $V_g = 0.042$ cm/sec
3. $D = 10^{-4}$ cm^2/sec, $V_g = 0.125$ cm/sec
4. $D = 10^{-3}$ cm^2/sec, $V_g = 0.042$ cm/sec
5. $D = 10^{-3}$ cm^2/sec, $V_g = 0.125$ cm/sec

108

Fig. 7. Interface concentration ratio in the solid, C_s/C_o, along the ribbon width for $w_d/w_c = .20$ and $k_o = 10^{-5}$. Graph parameters:

1. $D = 10^{-5}$ cm^2/sec, $V_g = 0.042$, 0.125 cm/sec
2. $D = 10^{-4}$ cm^2/sec, $V_g = 0.042$ cm/sec
3. $D = 10^{-4}$ cm^2/sec, $V_g = 0.125$ cm/sec
4. $D = 10^{-3}$ cm^2/sec, $V_g = 0.042$ cm/sec
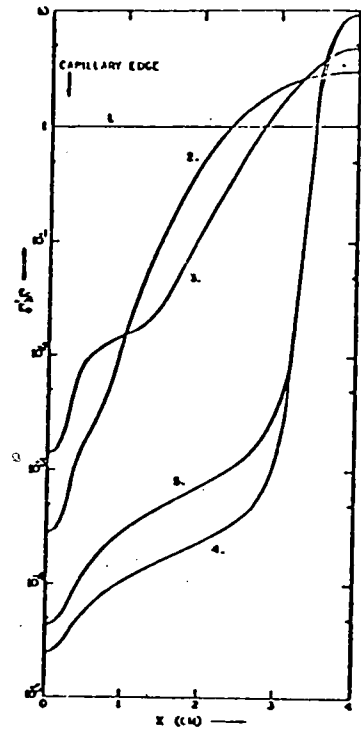5. $D = 10^{-3}$ cm^2/sec, $V_g = 0.125$ cm/sec

Fig. 8. Concentration (C) and horizontal component of velocity (u) boundary layers ahead of the growth interface.
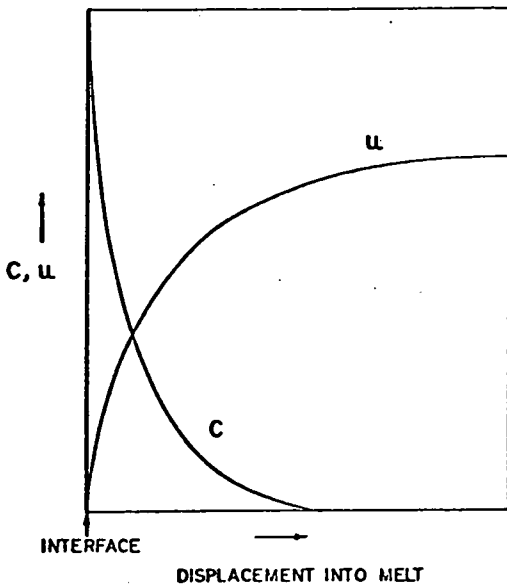
Fig. 9. Interface concentration ratio, C_s/C_o, and horizontal component of melt velocity, u, along the ribbon width for $w_d/w_c = 20$, $V_g = 0.042$ cm/sec, $k_o = 10^{-5}$ and $D = 10^{-4}$ cm^2/sec. The values of u are those at a distance of 0.0025 cm from the growth interface, well within the momentum boundary layer.

109